Title
Spin-orbitronics: Electrical control of magnets via spin-orbit interaction

Author
Upadhyaya, Pramey

Publication Date
2015

Peer reviewed|Thesis/dissertation

UNIVERSITY OF CALIFORNIA

Los Angeles

Spin-orbitronics: Electrical control of magnets via spin-orbit interaction

A dissertation submitted in partial satisfaction of the requirements for the degree Doctor of Philosophy in Electrical Engineering

by

Pramey Upadhyaya

2015

ABSTRACT OF THE DISSERTATION

Spin-orbitronics: Electrical control of

magnets via spin-orbit interaction

by

Pramey Upadhyaya

Doctor of Philosophy in Electrical Engineering

University of California, Los Angeles, 2015

Professor Kang Lung Wang, Chair

Relativistic effects, having far reaching consequences for advancing our fundamental understanding of the nature, have so far mostly played an academic role in solid-state systems. For example, electrons moving in atomic orbitals close to the speed of light acquire a relativistic shift in energy via the so-called spin-orbit interaction (SOI). More recently, the ability to engineer this relativistic SOI in magnetic system, has shown potential to extend the reach of relativity into technological applications by providing an energy-efficient electrical knob to control magnetic order via torques, now referred to as the spin-orbit torques (SOT). In this dissertation, this "spin-orbitronic" control of magnets interfaced with heavy elements, which in turn possess a high SOI, is presented. Starting from a symmetry-based phenomenology, the role of reduced symmetries leading to the identification of two flavors of SOT: current-induced and

voltage-induced is highlighted. Focusing first on magnetic-memory-type applications, theoretical proposal and experimental demonstration of new SOT resulting from breaking additional lateral structural symmetry is then presented, which allows for the removal of power hungry external magnetic fields for switching magnets. Subsequently, the required switching currents are reduced by nearly three orders of magnitude via demonstration of extremely efficient SOT in topological insulator-based magnets with engineered inversion asymmetry. Next, motivated by going beyond memory applications, the role of SOT to create and manipulate magnetic solitons, i.e. particle-like magnetic configurations capable of storing and transporting non-volatile information is presented. This includes: (a) experimental demonstration of a scheme for current-induced creation and manipulation of such solitons utilizing inhomogeneous SOT, (b) theoretical possibility of manipulating these solitons via more energy efficient electric-field-induced SOT. Finally, excitation of magnetization dynamics in insulating magnets, for transporting information by Joule heating free "pure spin currents", is of particular importance for low power requirement. Consequently, an optical scheme demonstrating current-induced SOT in insulating magnets is developed, followed by a proof of principle demonstration of motion of solitons via these pure spin currents.

The dissertation of Pramey Upadhyaya is approved.

Yaroslav Tserkovnyak

Oscar M. Stafsudd

Kang Lung Wang, Committee Chair

University of California, Los Angeles

2015

Dedicated to my family,

specially to the loving memory

of my grandfather, Somnath Upadhyaya

TABLE OF CONTENTS

LIST OF FIGURES

ACKNOWLEDGMENTS

I have always been a person with strong mirror traits (which even reflects in the structure and choice of words in the current acknowledgement section) and thus have been extremely fortunate to meet some exceptional personalities who have played a crucial part in shaping my life till today. Without their help, at all the crucial stages of my educational development process, I would not have been able to make an attempt at composing this thesis. At the risk of making it sound like an Oscar thank you speech, I am extremely happy to go over these experiences and get a chance to thank them below in a chronological order.

First and foremost I would like to thank my parents, *Lalita* (ma) and *Sunil* (papa), who, apart from being the reason for my existence, have from my childhood instilled in me the pursuit of academic achievements. My father, being a professor himself, has always inspired me to try and become one myself, while my mother, also my first mathematics teacher, has been responsible for showing me the elegance in mathematics (which in my earlier days I mistakenly thought was a subject, like every other, that should be memorized). Every PhD student has their childhood heroes, basically teachers, who instigate the interest in the subject one pursues in their PhD. *Rao Mam* and *Shukla Sir* were my childhood heroes, whom I cannot thank enough for invoking my interest in the beauty of Physics, which has remained (and will in the future) with me as the major driving source for all my research explorations. At the undergraduate level, I am grateful to my senior *Angik Sarkar* and *Prof. Supriyo Bandyopadhyay* for introducing me to the wonderful field of Spintronics (which is the main theme of the thesis) and the joy of finding something new.

This brings me to my graduate studies and the "real" start of the PhD, where I was in a very unique and fortunate setting with (as described by one of my advisors) "one foot in experimental engineering aspects and the other in theoretical physics". More importantly, I was extremely lucky to work with the professors who are leaders in both of these aspects of spintronics. On the experimental side, Prof *Kang Wang*, my graduate advisor, has been crucial in suggesting and guiding the research projects pursued in this thesis, most of which started from the humble beginnings of the (in-)famous "Saturday afternoon brainstorm sessions". I will always be amazed at his passion for progressing the science and unique capability of applying his scientific wisdom to completely new problems, opening novel fields at the frontier of science. I sincerely hope this is one trait which I can mirror in my future endeavors. On the physics side, I owe all my acquired technical knowledge and skills to Prof. *Yaroslav Tserkovnyak*. A well-established leader in theoretical spintronics, I admire how he can combine his genius with amazing teaching skills and child-like enthusiasm for, not only keep coming up with novel predictions and insights, but to inspire the next generation of scientists to find their own. Risking plagiarism I would like to copy a sentence from his own thesis stating that he will always remain for me the golden standard of intellectual excellence and scientific conduct. There are two more professors whom I wish to thank, who were critical during this PhD study: Prof. *Benjamin Williams* and Prof. *Oscar Stafsudd* for their valuable time, advice and patience while serving as the committee members.

Although professors are responsible for guiding and laying down the general directions, much learning about the details (the necessary devil to complete the PhD) is acquired through interaction with the "partners in crime" also referred to as *lab mates*. I would like to take this opportunity to thank: *Pedram K. Amiri* (I was confused where to put Pedram, as recently he has

obtained the much deserved title of a Professor; however he has always been more of a “partner in crime” and involve in the details for me), *Juan Alzate, Yabin Fan, Guoqiang Yu, Wanjun Jiang, Mohammad Montazeri, Scott Bender, Silas Hoffman and So Takei* for playing that role. Much of the experimental work directly contributing to this thesis on: topological-insulator based magnets, zero-field magnetic switching, magnetic solitons and optical measurement of spin-orbit torques was led by Yabin, Guoqiang, Wanjun and Mohammad, respectively. In addition, I would like to express my gratitude for all the DRL members, especially the staff members *Eileen Panguito* and *Wendy Sanchez* for helping with many complex situations faced as a foreign graduate student (which sometimes included maintaining a legal status !) or getting favors from Prof. Wang.

. One can indulge into the practice of enjoying research freedom and still eat a meal every day, specially living in Los Angeles, only if there is a hand of a funding agency having trust in your field. Consequently, during my M.S./PhD course, I acknowledge funding from different projects, starting from the DARPA STT-MRAM program, followed by the DARPA Non-volatile logic program, then the NSF TANMS center at UCLA, the Qualcomm Innovation Fellowship, the WIN and FAME research centers funded by DARPA and Semiconductor Research Corporations and finally the US DOE center SHINES. Thanks!

Last but not the least, a big part of (nearly) completing the PhD comes down to the comforting and reassuring words from friends and family, who keep you sane “off the field”. In this regard, I would like to thank my sister, brother–in-law *Paridhi & Saurabh*; and friends: *Kavitha, Karthik, Anil, Nomisha, Sharath, Vibhor, Krishna, Ajay, Tanu, Prabhat* and *Khushboo*. Although, not understanding anything I blabber after either succeeding or failing at an attempt to solve the (many) problems faced during PhD, they keep instilling the confidence back. *Shukriya* !

VITA

Education

2009-2011 M.S., Electrical Engineering
University of California, Los Angeles, United States

2005-2009 B.Tech., Electrical Engineering
Indian Institute of Technology Kharagpur, West Bengal, India

Employment history

2011 Graduate Research Intern – Components Research Group
Intel Corporation, Hillsboro, Oregon, United States

Selected publications

- **P. Upadhyaya**, G. Yu, P. Khalili Amiri and K.L. Wang, "Electric-field guiding of magnetic skyrmion", arxiv1505.03972, 2015.

- M Montazeri*, **P. Upadhyaya** *, M.C. Onbasli, G. Yu, K.L. Wong, M. Lang, Y. Fan, X. Li, P.K. Amiri, R.N. Schwartz, C.A. Ross, K.L. Wang, "Magneto-optical investigation of spin-orbit torques in metallic and insulating magnetic heterostructures", submitted (Nature Nanotechnology) ***equal contribution**

- W. Jiang, **P. Upadhyaya**, W. Zhang, G. Yu, M.B. Jungfleisch, F.Y. Fradin, J.E. Pearson, Y. Tserkovnyak, K.L. Wang, O. Heinonen, S.G.E.T Velthuis and A. Hoffman, "Blowing magnetic skyrmion bubbles", Science 349, 6245 (2015).

- Y. Fan*, **P. Upadhyaya** *, X. Kou*, M. Lang, S. Takei, Z. Wang, J. Tang, L. He, L.T. Chang, M. Montazeri, G. Yu, W. Jiang, T. Nie, R.N. Schwartz, Y. Tserkovnyak and K.L. Wang, "Magnetization switching through giant spin-orbit torque in a magnetically doped topological insulator heterostructure", Nature Mater 13, 699 (2014); ***equal contribution**

- G. Yu*, **P. Upadhyaya** *, Y. Fan, J. G. Alzate, W. Jiang, K.L. Wong, S. Takei, S.A. Bender, L.T. Chang, Y. Jiang, M. Lang, J. Tang, Y. Wang, Y. Tserkovnyak, P.K. Amiri and K.L. Wang, "Switching of perpendicular magnetization by spin orbit torques in the absence of external magnetic fields", Nature Nano 9, 548 (2014); ***equal contribution**

- **P. Upadhyaya**, R. Dusad, S. Hoffman, Y. Tserkovnyak, J.G. Alzate, P.K. Amiri and K.L. Wang Electric field induced domain-wall dynamics: depinning and chirality switching, Phys. Rev. B, 88, 224422 (2013) [**selected for Editor's suggestion**]

- W. Jiang*, **P. Upadhyaya** *, Y. Fan, J. Zhao, M. Wang, L.T. Chang, K.L. Wong, M. Lewis, Y.T. Lin, J. Tang, S. Cherepov, X. Zhou, Y. Tserkovnyak, R.N. Schwartz, and K.L. Wang

"Direct imaging of thermally driven domain-wall motion in magnetic insulators", Phys. Rev. Lett, 110, 177202 (2013); ***equal contribution**

CHAPTER 1: Introduction

1.1 Paradigm shift in information processing: Towards "greener" technology

The discovery of transistor [1] and the ability to pack them on a single functional chip, i.e. an integrated circuit [2], are considered as epochal events in the history of human civilization, kick-starting the so-called "silicon age". From then onwards the race has been towards packing more and more transistors on a single chip following a simple scaling rule [3]. This scaling rule has continuously increased the computational power, by roughly doubling the number of transistors per square inch of an integrated circuit (popularly referred to as the Moore's law [4]), and shrunk the size of information processing devices. These devices have now become an integral part of our lives, essential for computation, communication, and even entertainment needs.

At the same time, this never-ending demand for increased computing power, along with the rise in the number of computational devices, is slowly turning out to be a major source of energy wastage, demanding a shift towards the need for energy efficient computational devices, referred to as the "Green information technology". For example, currently, the developed countries spend about 5% of total electricity on information technology and are projected to reach the 20% mark by 2020. The CPU power density of a Pentium chip with a billion or more transistors is rapidly approaching that of a nuclear reactor with current values of 100 W/cm^2 (see Fig. 1.1, taken from Ref. [5]). One of the major culprits for this consumption are the Data centers, whose demands will only increase, unfortunately following its own "energy-wastage Moore's law", in today's "big data" era. Another major shift seen by information processing industry is the emergence of mobile devices: smart-phones, tablets, computing watches and glasses. The

number of global users of mobile devices has already surpassed that of desktops in the year of 2014. The single most important issue faced by these mobile devices is the short battery-life, also having its origin in power hungry devices.

In conclusion, there is an immediate need to find low energy consumption devices that could potentially keep up with this paradigm shift towards Greener technology. In this thesis, motivated by this grand challenge we evaluate magnetic devices exploiting a, seemingly unrelated, relativistic effect for the possibility of making energy efficient devices. One could guess from the fact that since the author is not a CEO of a multi-million dollar establishment (*at least not at the time of writing*), we haven't "solved" this issue in this thesis. However, the scope of the thesis is to show the promise of the approach and, along the way, discover fundamentally new phenomenon that could potentially be used in the future greener devices. In the next section, we highlight why magnet-based devices could meet the demand for a low energy computing device which has, in the recent past, opened a burgeoning field called *spintronics* [6].

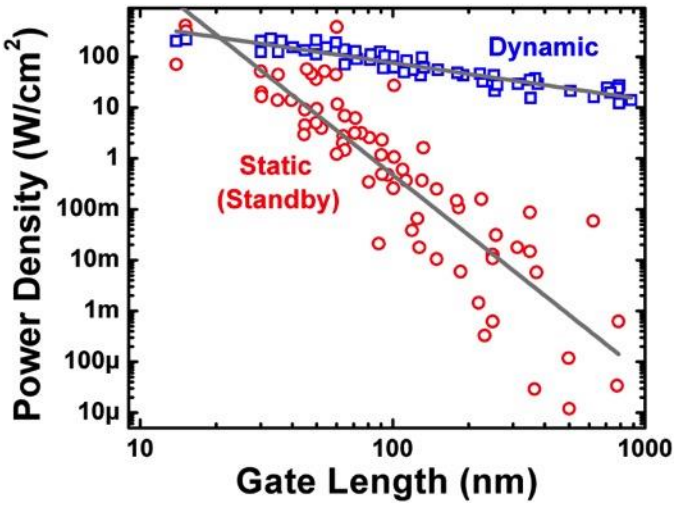

Fig. 1.1 As the CMOS transistor is scaled down, the loss of electrostatic control of the gate translates into a drastic increase of the dissipated static power density. The scaling trend shows how static power has become a major component into the total dissipated power for current technology nodes. This is one of

the motivations for non-volatile electronics: Alleviating the static power dissipation problem and allowing for instant-on electronics (Taken from Ref. [5]).

1.2 Spintronics: promise of magnets for greener technology

The major issue with today's transistors is that, although, they are pretty efficient when they are doing the computation, utilizing about 1femto-Joule (fJ) of energy per switch (referred to as the dynamic power), they end up wasting about the same or even more energy when they are dormant (referred to as the static power). This problem is compounded as the transistors are scaled to smaller dimensions (see Fig. 1.1). The basic reason behind the issue, as explained next, is that transistors are charge-based devices which start leaking in the dormant state. In its most simplistic form, a transistor is a voltage-controlled switch comprising of three terminals, namely, (i) source (ii) drain and a (iii) gate. To turn the switch "ON", a voltage, V, is applied at the gate terminal increasing transistors ability to conduct between source and drain, while to turn the transistor "OFF" this voltage is removed. Consequently, during this dynamic cycle, charges are drawn from the power source, stored in the capacitor components of transistor and discarded to the ground terminal, burning $CV^2/2$ dynamic energy, where C is the value of capacitance. Thus, in order to reduce this dynamic power transistor can be simply scaled down reducing its capacitance and operation voltage. However, as the transistor is scaled to few tens of nm size, several non-idealities start to kick in [7]. One of these non-idealities being: leakage of charge over time, both, through the thinner gate oxide, and between source and drain resulting in an "OFF" state leakage current. This leakage current, in turn, results in the increased static power due to increased Joule heating. Moreover, this leakage leads to leaking of information when power is turned off making these devices typically volatile. Thus, if devices can be constructed using variables different from charges, which remain stable for few years, one can completely

shut-off the static power resulting in energy-efficient devices. Magnet-based memory, like hard-disks, using the spin-state of electron to store information (as opposed to charge), have been utilized for quite a few time for storing information for several years, making them natural candidates suited for this task.

Spintronics is an active and growing area of research and development (R&D) where this spin degree of freedom is electrically controlled to engineer devices for computation, sensing and storage. In Spintronics, the information is coded in the orientation of a collection of spins. This particular spin configuration is fixed at a local minimum of a designed energy landscape. The "leakage" of information is then described by change of spin configuration to another local minimum caused by thermal fluctuations-induced escape over a barrier (see Fig. 1.2, left panel). For magnets, it is very easy to design an energy barrier of $\sim 40\ k_B T$ [8], where k_B and T are the Boltzman's constant and operation temperature respectively, corresponding to an escape rate of tens of years at room temperature. This is basically why information stored in magnets is considered "non-volatile".

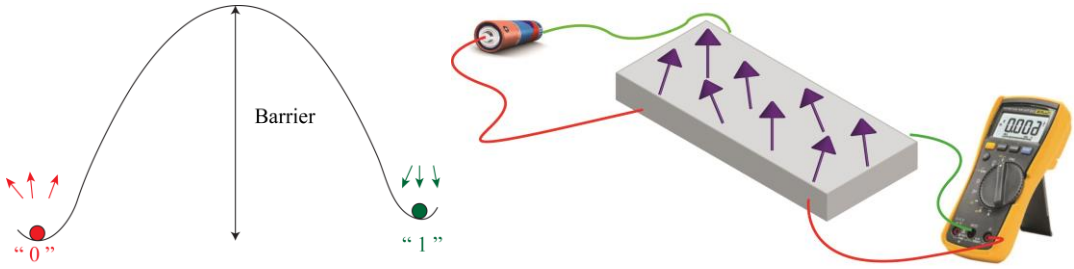

Fig. 1.2 **(Left panel)** Nonvolatility of a typical spintronic bit: Information stored in particular orientation pf spins (shown by arrows) constitute bit "1" or "0". An energy barrier separates these two configurations whose height can be made sufficiently large to guard information from thermal fluctuations at room temperature. **(Right panel)** A spintronic device showing a magnet based region controlled and read via electrical contacts. The transmutation of electrical to magnetic degrees of freedom is the most power

hungry step in current devices making dynamic power of spintronic devices larger than that of charge-based counterparts.

If the standby power of spintronic devices is zero then a natural question arises that what is stopping us from making spintronic devices? One of the major reasons is the high dynamic power. In spintronic devices (different from charge based devices), during the computation cycle, transmutation of electrical to magnetic energy needs to take place in order to interface the magnets with electrical inputs and outputs (see Fig. 1.2, right panel). The dynamic power requirement for this electric control of magnets is one of the major bottlenecks of present day spintronic devices and an area attracting rigorous research activity. For example, the dynamic energy required to perform one operation for a typical magnet-based device using a popular mechanism for electric control of magnets, referred to as spin-transfer-torque from polarizers (see next section), is $\sim 10^{-13}$Joules [9] as compared to $\sim 10^{-15}$Joules for a transistor. Moreover, when compared to the energy barrier of $\sim 40\ k_B T \sim 10^{-18}$Joules, for storage of roughly 10 years, there exists a gap of about five orders of magnitude that could potentially be closed, providing the motivation for most ongoing activities in this field. In the next section, we provide a brief review of some of the mechanisms employed for achieving the sought electric control of magnets.

1.3 Electrical control of magnets: mechanisms

The fundamental property storing information in the magnetic devices is the spin of the electron. Spin is, in turn, a quantum mechanical form of angular momentum inherent to electrons, which below a critical temperature develops a net non-zero magnitude when atoms are brought together to form a magnetic material. Thus, broadly speaking, to manipulate information stored

in spins two possible routes have been explored: (a) modifying the critical temperature and (b) exchange angular momentum with the magnets, applying a torque on them. The various mechanisms explored so far to achieve task (a) and (b) *electrically* are summarized in Fig.1.3 and are described below:

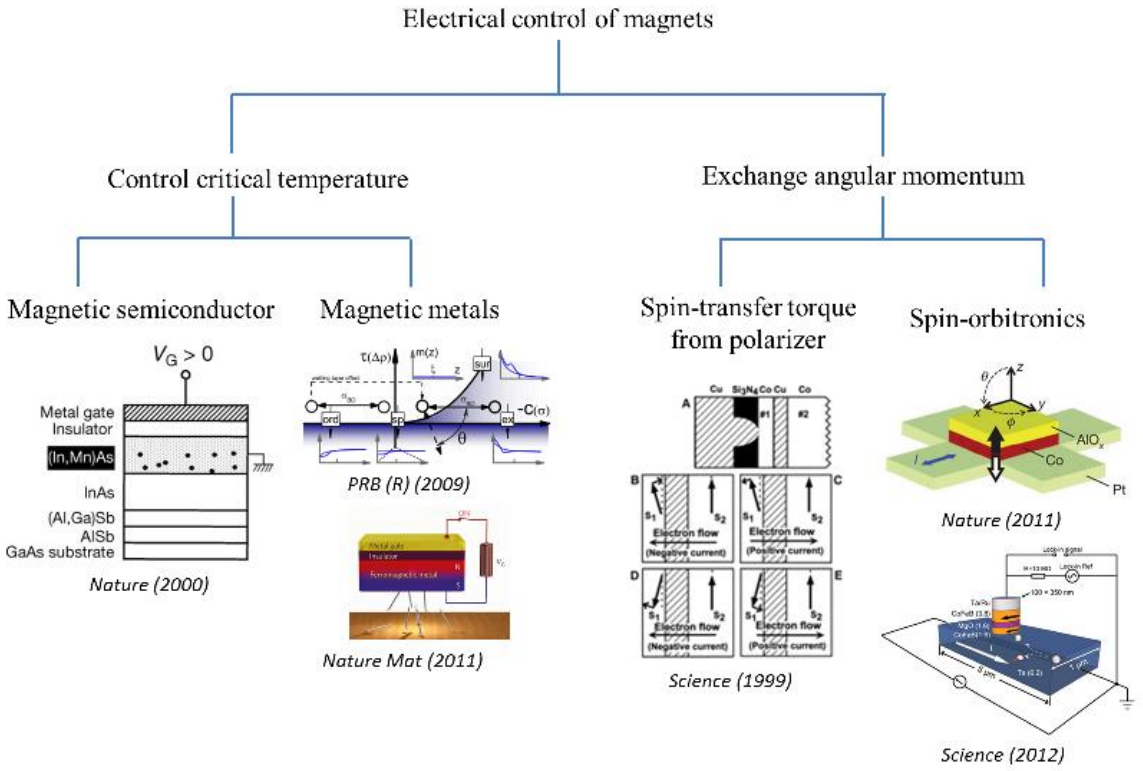

Fig. 1.3 Strategies for electrical control of magnets

Electric-field-controlled Curie temperature: The idea to mimic the success seen by doping of semiconductors to control their conductivity resulted in the discovery of dilute magnetic semiconductors (DMS) [10]. It was demonstrated that a magnetic-semiconductor material system can be "cooked" up by the introduction of dilute magnetic impurities in a host non-magnetic semiconductor. This marriage of semiconductors with magnets allowed to take advantage of the skill set already developed to control semiconductors electrically. In particular, it was shown that by varying the concentration of carriers via an external electrical "gate" the Curie temperature

could be modified, thus providing a method to control magnetism electrically [11]. One mechanism proposed for this phenomenon is that the exchange interaction between the magnetic dopants is mediated by the carriers [12]. The Curie temperature is set by the strength of this exchange interaction which, in turn, depends on the concentration of carriers. Thus, via controlling the carrier concentration by a gate, the strength of exchange interaction between the magnetic dopants, and hence, the Curie temperature can be controlled. A thorough discussion of the mechanisms resulting in this electrical control is beyond the scope of this thesis and a matter of current research (interested readers are directed to Ref. [13] [14] for a review). Furthermore, electric control of Curie temperatures has been predicted [15] and demonstrated [16] even for metallic thin films.

The advantage of this method is that the use of electric fields for control of magnets allow for dynamic power comparable to CMOS transistors (which are also field controlled devices), however, the major challenge remaining for quite some time now has been to bring the operating temperature of DMS to the room temperature.

Spin transfer torque (STT): A method to electrically exchange angular momentum with a magnet is to transfer the angular momentum to it from another magnet. This method was first theorized by Slonczewski and Berger [17] [18] and subsequently experimentally demonstrated by [19-21]. This is achieved by making a ferromagnet(FL)/non-ferromagnet/ferromagnet(PL) sandwich structure (Fig.1.4). When the non-ferromagnet is a metal (insulator) the structure is called a spin-valve (magnetic-tunnel junction) [22]. One of the ferromagnets, PL, acts as a polarizer pinned along a certain direction by either making it thicker or using exchange bias [23], while the other ferromagnet, FL, is free to orient in any direction. When an unpolarized electrical current (composed of equal number of “up” and “down” spins) is passed through this sandwich structure,

it first gets spin-polarized by the PL and subsequently transfer this acquired polarization to the free layer applying a torque on the FL, thus providing the electrical control of the magnet.

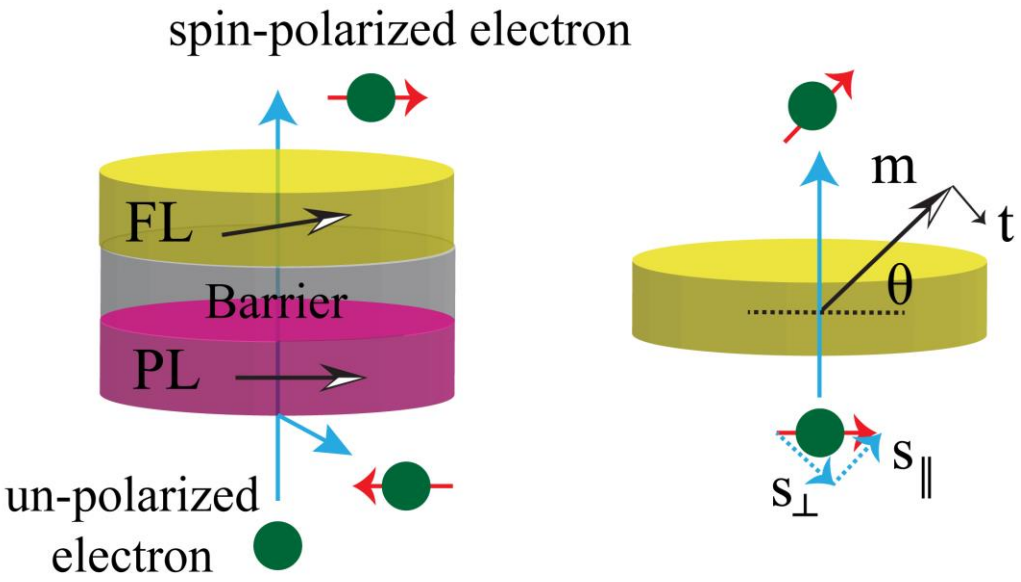

Fig. 1.4 **(Left panel)** Angular momentum transfer from a pinned layer (PL) to a free layer (FL).These layers separated by a barrier forms the basic element of a magnetic tunnel junction. Current passed through such a stack becomes spin polarized by PL which transfers angular momentum to FL **(Right panel)** Illustration of spin-transfer-torque: Spin filtering action of a single free layer for non-collinear spin injection. Magnet transmits spins collinear to the magnetization (**m**) absorbing the transverse component ($s_\perp$) and resulting in a torque (τ).

This spin transfer torque can, in turn, be motivated by a simple picture depicted in Fig.1.4 (right panel). When a spin-polarized current passing through a magnet has its spin oriented at some angle θ with respect to the magnetization direction, only the components parallel to the magnetization is passed through the magnet. Consequently, the angular momentum of the electrons before and after "scattering-off" the magnet is not the same. The component perpendicular to the magnetization is said to be absorbed by the magnet resulting in a STT.

Quantitatively, STT is proportional to the product of current density, J, and effective polarization $P < 1$, acquired during the filtering of current provided by the polarizing PL. The advantage of the method is that, being dependent on the current density, the critical currents required to perform a dynamic switch scales down with the area of the device. However, the energy required to perform this switching for typical nm-sized samples, having a retention time of few years, is $\sim$0.1 pico-Joules. One of the primary reasons being the critical current, with polarization limited to 1, is high. To overcome these challenges, recently, a completely new method of transferring angular momentum has been discovered, termed spin-orbitronics, which we describe next.

1.4 Spin-orbitronics

The contents of this and next section are adapted from work originally published as a chapter in Ref. [24]

Angular momentum associated with the orbital degrees of freedom provides yet another source which can be used to apply torque on the magnets. Thus if a method can be devised to couple the orbital motion (which is controlled electrically) with the spin degrees of freedom, angular momentum can be exchanged with magnets electrically applying new kind of torques, referred to as the spin-orbit torques (SOT). In particular, the advantage of this way of applying torques over STT from a polarizing layer is that the efficiency of the former is not limited by $P < 1$ and can thus reduce critical currents and dynamic power. This spin-orbit torque is at the heart of the effects discussed in this thesis, whose origin we discuss in details next.

1.4.1 Spin-orbit interaction (SOI) as the coupling mechanism

Spin-orbit interaction, describing the coupling between the orbital and spin degrees of freedom provides yet another avenue to control magnetism electrically. Fundamentally, spin-

orbit interaction is a relativistic effect as explained in the following. The relativistic equation describing electrons in an atom (see Fig. 1.5) is the well-known Dirac equation, which when approximated up to second order in v/c (with v and c being the electron's velocity and the speed of light), generates (amongst others) the following Pauli spin-orbit coupling term [25]:

$$H_{SO} = -\frac{\hbar}{4m_0^2c^2}\boldsymbol{\sigma} \cdot \boldsymbol{p} \times \boldsymbol{\nabla} \mathrm{V}_0 \, . \tag{1.1}$$

Here $\hbar$ is the reduced Planck's constant, m_0 is the electron's mass, $\boldsymbol{\sigma}$ is the Pauli spin matrix vector, $\boldsymbol{p}$ is the momentum operator and V_0 is the atomic potential. Typically, this relativistic effect is more important for the core electrons, which are closer to the nucleus and are thus moving at much higher velocities. Similarly, the heavier elements have a larger spin-orbit coupling. In a crystal, the valence electrons move in a periodic "pseudopotential", i.e. the atomic potential, due to a periodic arrangement of nuclei, renormalized by the core electrons. In this case, these valence electrons are described by the so called Bloch bands and the effect of spin-orbit coupling, entering through the pseudopotential, is conveniently parameterized by a material dependent effective parameter, which can be obtained from the bandstructure [25]. The consequence of a spin-orbit term is that the orbital degrees of freedom, which can be controlled electrically, become coupled to the spin-degrees of freedom, which in turn can interact with magnetic order, and hence provide the sought mechanism for electric control of magnetism.

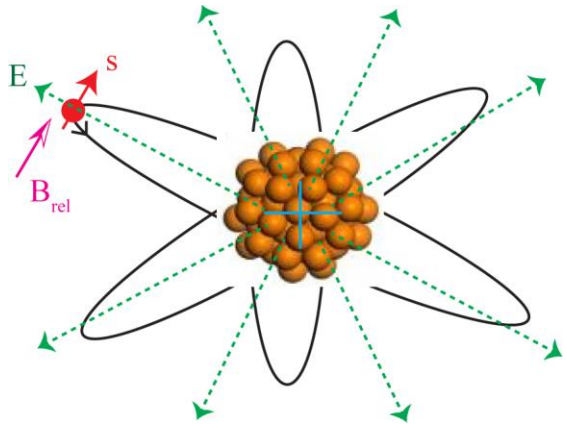

Fig. 1.5 Illustration for origin of spin-orbit interaction: an electron orbiting around the positively charged nucleus experiences electric field € transformed to a relativistic magnetic field (B_{rel}) in its own reference frame. This magnetic field interacts with the spin of the electron (s) to give rise to spin-orbit interaction.

1.4.2 Marrying SOI with magnets: material systems

Although the effect of spin-orbit interaction on electrical transport was known for quite a while [26], the recent increased interest in spin-orbitronics has been triggered by the ability to engineer high spin-orbit interaction into magnetic system. Typical magnets, being light, possess a weak intrinsic spin-orbit coupling. On the other hand, as was mentioned in the previous section, high spin-orbit interaction requires presence of heavy elements. Thus two possible routes exist to achieve the marriage of magnets with spin-orbit interaction: (Fig.1.6) : (a) interfacing magnetic thin films with heavy-metal system [27], like Platinum , Tantalum, Tungsten and Bismuth doped Copper (b) Magnetically doping materials having intrinsically high spin-orbit coupling for example Cr-doped Bismuth selenide compounds [28] and Manganese doped Gallium Arsenide [29]. As will be explained in the next section, to observe non-trivial effects arising from spin-orbit interaction in magnets, it is also important to break certain structural symmetries. For thin-film interfaces (i.e. (a)) this is achieved by growing asymmetric interfaces, while for magnetically doped systems either asymmetric doping profile may be used, for example doping Cr on one side of Bismuth Selenide compound [28] or the host material itself might lack some

structural symmetries, like absence of inversion in GaAs [29]. In this thesis we will focus on both of these strategies. Before diving into the details of spin-orbitronic control studied here, we briefly mention the new possibilities opened up by this ability to engineer SOI in magnets.

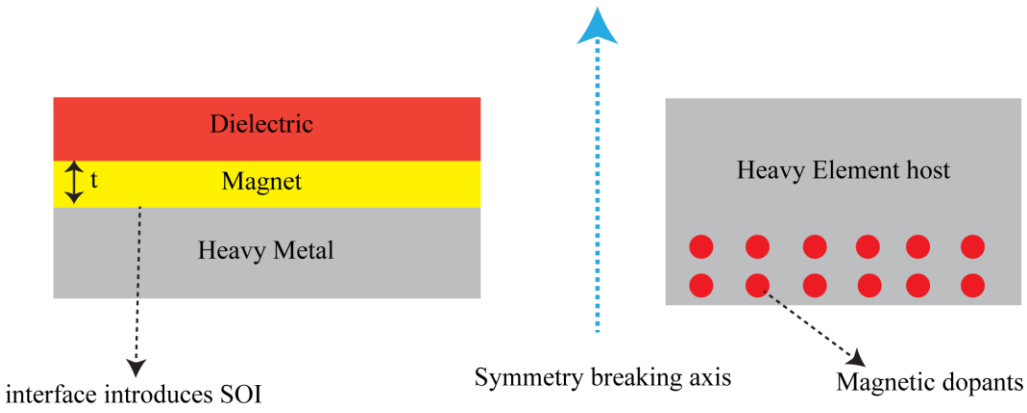

Fig. 1.6 Material system for introducing high SOI in magnets: **(left panel)** thin magnetic films interfaced with heavy metals. Thickness t is small enough such that interface properties dominate. SOI is introduced by presence of heavy metals. **(right panel)** Magnetic impurities are doped into a host heavy element material. In both structures structural symmetry is broken along the indicated axis.

1.4.3 New opportunities

The marriage of SOI and magnets has resulted in almost a revolution of new fundamental discoveries (amazingly all within the lifetime of this PhD), including giant spin-orbit torques in heavy metal/metallic ferromagnet interfaces [30, 31] and topological insulators [28, 32], switching of magnets and efficient motion of domain walls using SOTs [33, 34]. This has not only provided a pathway to improve upon the efficiency of STT from polarizers, as discussed above, but opened up opportunities that were not possible before (see Fig 1.7). For example, heavy elements can be interfaced not only with metallic magnets but with magnetic insulators as

well. This has provided an efficient method to electrically excite and detect spin waves and magnons for joule heating free transport of spin information [35], a field dubbed as *magnonics* [36]. On another front magnetic doping of a new class of materials called topological insulators (which themselves owe their experimental existence to SOI) has resulted in the observation of truly dissipationless transport of charge current in the absence of magnetic fields, referred to as the Quantum Anomalous Hall effect [37], prompting a field called *topotronics* [38]. Furthermore, SOI has shown to stabilize magnetic structures with non-trivial topology, known as skyrmions, which could provide new stable objects for performing memory and logic applications for *skyrmionics* [39].

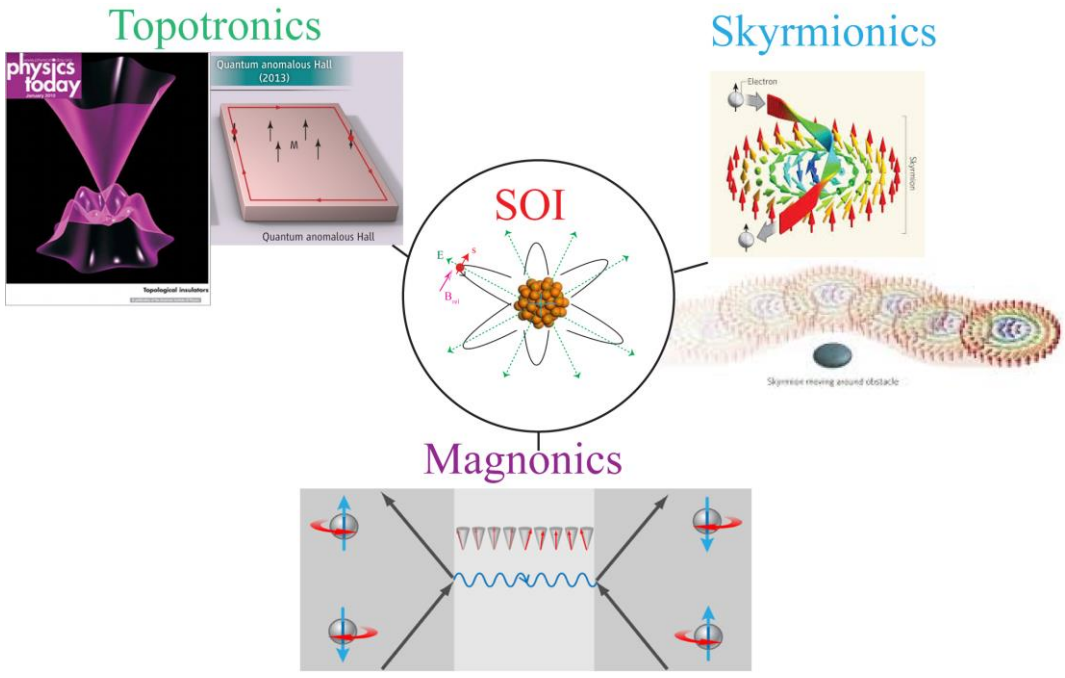

Fig. 1.7 Some novel fields enabled by spin-orbit interaction.

1.5 Role of symmetries and types of SOT

The presence of spin-orbit interaction is necessary but not sufficient to induce a net non-zero spin-orbit torque. The other critical requirement is to break some structural symmetries. In fact, without invoking any particular microscopic mechanism, purely based on symmetry considerations one can "derive" and thus predict the role of spin-orbit interaction in controlling magnets. This symmetry-based phenomenological approach is not unique to spin-orbitronics and was championed by the famous Russian physicist Lev Landau in developing his theory for phase transitions [40]. The biggest advantage of such an approach is that it provides a general framework, applicable to any microscopic mechanism, for deriving and or predicting non-trivial effects induced by spin-orbit interaction. In this thesis we adopt this method to analyze and predict novel spin-orbitronic effects which were measured directly by experiments. In what follows, we derive equation of motion of magnets in presence of spin-orbit interaction, both, in and absence of electrical signals. This treatment, on the one hand, serves the purpose of introducing all the effects that will be discussed in the subsequent chapters in a unified fashion, while on the other, highlights the connection between symmetry breaking and spin-orbit torques.

All spin-orbitronic devices discussed here work below the Curie temperature, where the magnitude fluctuations in the magnetization are suppressed and the information is stored in the orientation of magnetization. The equation of motion conserving the magnitude of magnetization can then be written within the Landau Lifshitz Gilbert (LLG) phenomenology as [41, 42]:

$$\partial_t \boldsymbol{m} = -\gamma \boldsymbol{m} \times \boldsymbol{H}(\boldsymbol{m}, I, V) + \alpha \boldsymbol{m} \times \partial_t \boldsymbol{m} \,. \tag{1.2}$$

Here, α is the Gilbert damping parameter, γ is the gyromagnetic ratio and $\boldsymbol{m}$ is a unit vector oriented along the magnetization. The effective field $\boldsymbol{H}(\boldsymbol{m}, I, V) \equiv \boldsymbol{H}_m + \boldsymbol{H}_I + \boldsymbol{H}_V$ includes the following contributions: $\boldsymbol{H}_I$ and $\boldsymbol{H}_V$ represent the electrically controlled terms allowed via spin-

orbit interaction, while $\boldsymbol{H}_m$ represents the sum of externally applied and the internal effective magnetic fields, which in its minimalistic form is derived from exchange, dipolar and crystalline anisotropy energy. The crystalline anisotropy energy is the first example of a term that arises due to spin orbit interaction. Intuitively, in the presence of spin-orbit interaction the magnetization, i.e the spin degrees of freedom, becomes "aware" of the crystalline structure, i.e the orbital degrees of freedom, and hence prefers to orient along certain crystalline axis, known as the easy axis. In this sense, even in the absence of any electrical control, spin-orbit interaction influences the orientation of magnetization. In fact, for computational devices this crystalline anisotropy term is crucial, as by restricting the magnetization to point in opposite directions along the easy axis, the information becomes binary. Moreover, the barrier to overcome the anisotropy energy makes this information non-volatile.

To arrive at the form of allowed terms in $\boldsymbol{H}_I$ and $\boldsymbol{H}_V$ one can either start from the microscopic picture or utilize the symmetry principle. In the following we adopt the latter approach which states that the equation of motion should remain invariant under the transformations which respect the symmetry of the system under consideration. The typical symmetries of the devices discussed here are (see Figure 1.6):

(a) Rotation invariance about the growth axis (chosen to be oriented along the z-axis): the hetero-structures considered here are typically amorphous or polycrystalline films, thus having no favored direction in the film plane.

(b) Mirror symmetry: In all devices the mirror symmetry about the x-y plane is broken intentionally by having different material environment on top and bottom of the ferromagnet, leaving the structure mirror symmetric only about the y-z and x-z plane. In chapter 2 we will

also break the mirror symmetry about the x-z plane to introduce additional useful spin-orbit terms.

Imposing the above mentioned symmetries on the equation of motion and knowing that magnetization transforms as a pseudo-vector, the leading order terms allowed in $\boldsymbol{H}_I$ and $\boldsymbol{H}_V$ can be written as (some of the terms appearing at the same order as below are suppressed for simplicity, interested readers are referred to the Ref.[43, 44]):

$$\boldsymbol{H}_I = H^{DL}\boldsymbol{m} \times (\boldsymbol{z} \times \boldsymbol{i}) + H^{FL}(\boldsymbol{z} \times \boldsymbol{i}) \,, \tag{1.3}$$

$$\boldsymbol{H}_V = H_E m_z \boldsymbol{z} \ . \tag{1.4}$$

Here, $\boldsymbol{i}$ and $\boldsymbol{z}$ are the unit vectors along the current and the normal to the film plane, respectively. The $\boldsymbol{H}_I$ terms and corresponding torques, i.e. $\boldsymbol{m} \times \boldsymbol{H}_I$, are known as the current-induced spin-orbit fields and spin-orbit torques, respectively. The first term on the right hand side of $\boldsymbol{H}_I$ is known as the damping (or anti-damping)-like term, owing to its non-conservative nature with the corresponding torque changing sign under time reversal. While the second term is referred to as the field-like term, due to its conservative nature with the corresponding torque preserving sign under time reversal. The strengths of the damping-like and the field-like terms is in turn parameterized by H^{DL} and H^{FL}. Microscopically, two primary effects are typically associated with the spin-orbit torques: the so called spin-Hall effect [26] and Rashba/Edelstein effect[45, 46]. The spin-Hall effect is the flow of spin current transverse to charge current which in the diffusive metal systems arises due to inequivalent scattering of up and down spin electrons in the presence of spin-orbit interaction. This spin current can then interact with the magnetization and thus apply torque on it. While, the Rashba/Edelstein effect is an interfacial effect where, due to change in the bandstructure at the interface, large internal electric fields are typically present. These electric fields via spin-orbit interaction in turn lead to a net spin polarization which upon

interacting with the magnetization can also result in the above mentioned spin orbit torques. It is important to note that the current-induced spin-orbit torques vanish, even in the presence of spin orbit interaction, if all the mirror-symmetries are present.

Similarily, the $\boldsymbol{H}_V$ terms and corresponding torques, i.e. $\boldsymbol{m} \times \boldsymbol{H}_V$, are the voltage-induced fields and torques. Microscopically one phenomenon responsible for the voltage torques is the so called voltage control of magnetic anisotropy (VCMA) [47]. As was mentioned above, the magnetic anisotropies arise due to spin-orbit interaction, which are sensitive to electric field due to charging effect at the interface. As a result, the magnetic anisotropies can be tuned via application of gate-voltage, which in turn reorients magnetization by application of voltage-induced torques. Other possibilities include magneto-ionic effects [48] and strain-induced anisotropies[49].

So far, we have concentrated on terms uniform in magnetization, relaxing this constraint allows for additional spin-orbit-induced terms proportional to the gradients in magnetization. One such term which is gaining increased attention and will be of subject in chapter 3 is known as Dzyaloshinskii-Moriya interaction (DMI) [50, 51] : $\boldsymbol{H}_{\boldsymbol{DMI}}$ **.** Motivated by available experimental data, we will restrict our discussion here to equilibrium DMI, i.e. neglecting its current and voltage dependence. In this case, $\boldsymbol{H}_{\boldsymbol{DMI}}$ adds to $\boldsymbol{H}_m$ according to our scheme defined above and following the symmetry-based phenomenology its form is restricted to:

$$\boldsymbol{H}_{\boldsymbol{DMI}} = D(\partial_x m_z \hat{x} + \partial_y m_z \hat{y} - \partial_x m_x \hat{z} - \partial_y m_y \hat{z}). \tag{1.5}$$

Here D represents the strength of DMI interaction which depends on SOI. This form of DMI is also known as interfacial DMI, as it occurs at the breaking of mirror symmetry at the interface. Other forms of DMI, such as due to breaking of inversion in bulk have also been observed but will not be of importance here. The role of DMI is to encourage textured magnetization

structures (since it favors gradient in magnetization) of a particular handedness, known as chiral structures (see chapter 3 for details). The handedness or chirality is, in turn, dependent on the material specific sign of D.

Based on these allowed terms, a basic general element of a spin-orbitronic device that will be common to the following chapters would look like the schematic shown in Fig.1.8. Information can be stored in the orientation of magnetization, which can either be uniform or textured, manipulated by a current (passing laterally) -induced SOT and/or a voltage (applied via a gated structure)-induced SOT.

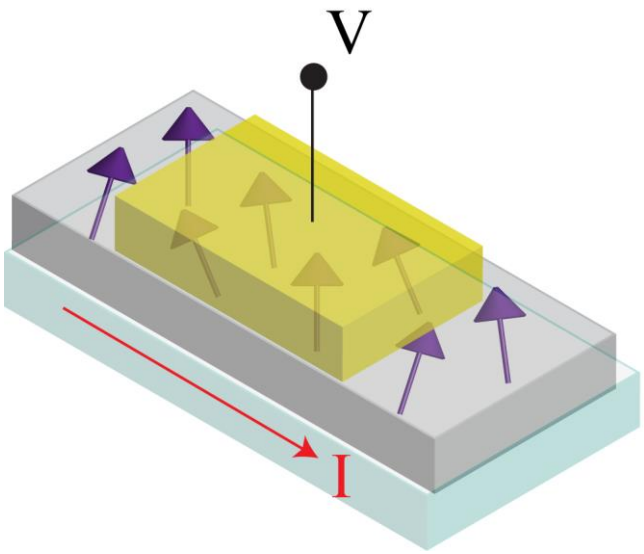

Fig. 1.8 A general schematic of spin-orbitronic devices discussed here. A magnet (middle layer) interfaced with heavy materials to have high SOI, resulting in following SOT: a lateral current-induced and or a top gate voltage-induced. The magnetic configuration manipulated could either be uniform or a soliton (which can , in turn, be induced by DMI part of SOI).

CHAPTER 2: Magnetization switching by Spin Orbit Torque

The content of this chapter is adapted from work originally published in Ref. [28, 43]

2.1 Motivation

. In this chapter, we focus on the switching of magnets via spin orbit torques (SOT). This is particularly relevant for memory applications, where a "0" or "1" is stored in the orientation of magnets, which can be electrically written by SOT. Such SOTs have been used to realize current-induced magnetization switching [30, 31] in recent experiments. Typical heterostructures exhibiting SOTs consist of a ferromagnet (F) with a heavy nonmagnetic metal (NM) having strong spin-orbit coupling on one side and an insulator (I) on the other side (referred to as NM/F/I structures, shown schematically in Fig. 2.1, which break mirror symmetry in the growth direction). In terms of device applications, the use of SOTs in NM/F/I structures allows for a significantly lower write-current compared to regular spin-transfer-torque (STT) devices, greatly improving energy efficiency and scalability for new SOT-based magnetic random access memory (SOT-MRAM) [31] , going beyond state-of-the-art STT-MRAM. However, two major challenges still remain in terms of dynamic power requirements: (a) undesirable external magnetic fields, which increase critical switching currents for a given thermal stability, are required to assist switching of high density perpendicular magnets and (b) the current level is still required to be brought down further for dynamic power to be comparable to the transistor. In this chapter, motivated by these challenges, we engineer device structures and material systems giving rise to novel form of SOT. Specifically, for mitigating (a) we break additional lateral

symmetries achieving switching in the absence of external magnetic fields, while for (b) we discover a new material system based on so called topological insulators and demonstrate reduction of the critical current by about three orders of magnitude.

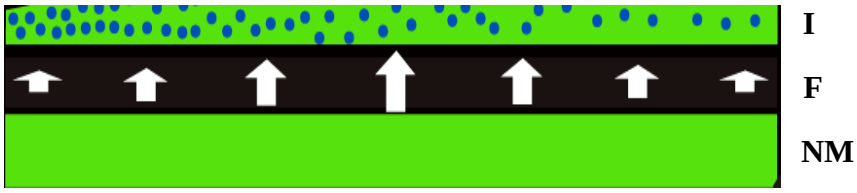

Fig. 2.1 The experimental structure: A ferromagnet,F, sandwiched between a normal metal, NM, (which typically have a heavy element) and an insulator, I. In the next section the insulator is formed by oxidizing the normal metal (oxygen shown schematically by blue circles), which can be controlled to control the strength of out-of-growth-plane anisotropy (indicated by arrows in the ferromagnetic layer).

2.2 External magnetic field free switching

We begin by looking at the strategy to remove external magnetic fields for SOT-induced switching. We present a new NM/F/I structure, which provides a novel spin-orbit torque, resulting in zero-field current-induced switching of perpendicular magnetization. Our device consists of a stack of Ta/$Co_{20}Fe_{60}B_{20}$/TaO_x layers that also has a *structural mirror asymmetry along the in-plane direction*. The lateral structural asymmetry, in effect, replaces the role of the external in-plane magnetic field. We present experimental results on current-induced SOT switching of perpendicular magnetization without applied magnetic fields. We also present a symmetry-based analysis of SOT interactions and show that this type of bias-field-free switching originates from the lateral symmetry-breaking of the device, giving rise to a new field-like torque upon application of an in-plane current.

2.2.1 Lateral symmetry breaking-induced novel SOT

As was shown in section 1.5, the current-induced SOT terms, which are physically allowed for a particular device structure, can be determined based on their symmetry properties. Hence, symmetry arguments provide a powerful tool in designing magnetic material and device structures to realize particular switching characteristics. Figure 2.2 schematically illustrates how lateral symmetry-breaking in the device can give rise to current-induced switching of perpendicular magnetization. The coordinate system is chosen such that the *z*-axis is fixed along the growth direction, and the current is applied along the *x*-axis. The figure depicts the following scenarios.

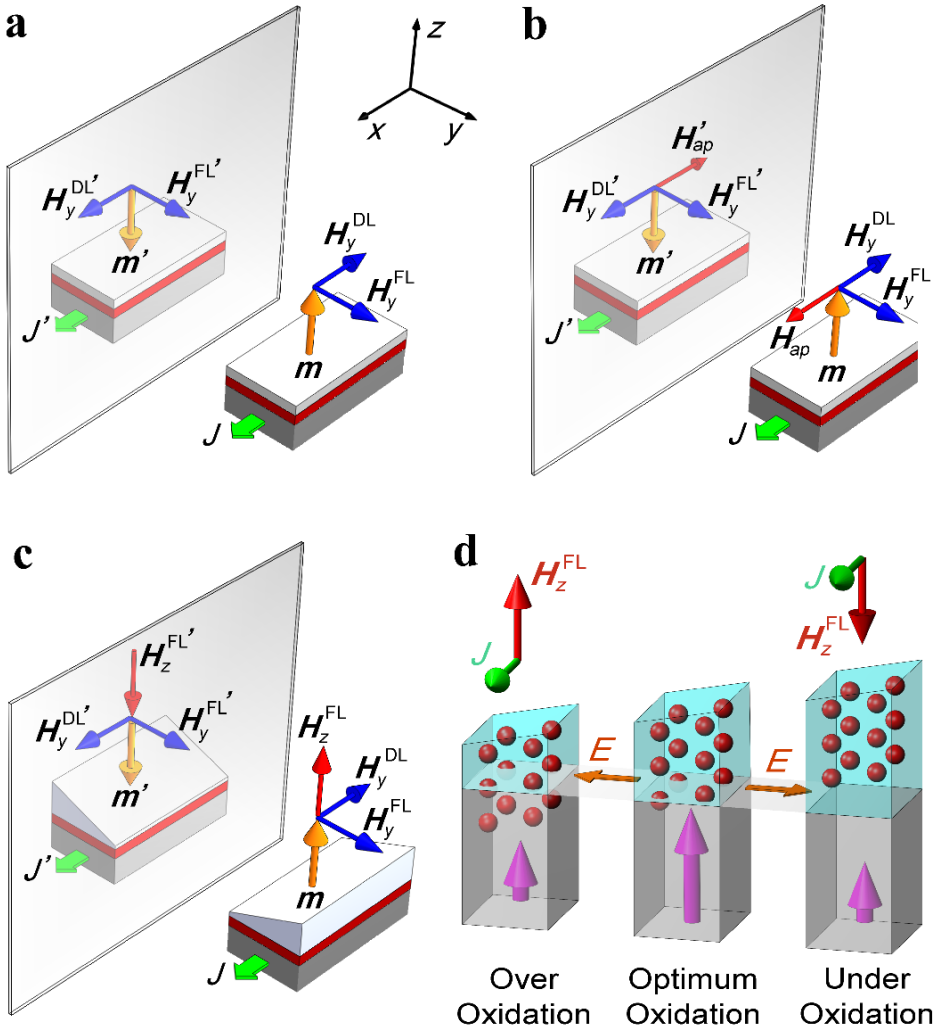

Fig. 2.2 Schematics of mirror symmetry and current-induced effective fields corresponding to spin-orbit torques (SOTs). **a,** Effective fields induced by current and absence of deterministic switching in a perpendicular magnetic structure symmetric about the *xz* plane, as same direction of current favors states with magnetization pointing up as well as down. The in-plane effective fields ($\boldsymbol{H}_y^{\mathrm{FL}}$ and $\boldsymbol{H}_y^{\mathrm{DL}}$) are permitted due to the structural inversion asymmetry along the *z*-axis. The blue arrows indicate the $\boldsymbol{H}_y^{\mathrm{FL}}$ and $\boldsymbol{H}_y^{\mathrm{DL}}$ and their mirror reflections $\boldsymbol{H}_y^{\mathrm{FL}\prime}$ and $\boldsymbol{H}_y^{\mathrm{DL}\prime}$ with respect to the *xz* plane. It is important to note the

difference between an external field $\boldsymbol{H_{ap}}$ and the damping-like field $\boldsymbol{H}_y^{\mathrm{DL}}$; the latter does not break the mirror symmetry about the *xz* plane as it depends on $\boldsymbol{m}$ and changes sign when magnetization is reversed, however, the former does break the aforementioned symmetry (see **b**). **b**, Symmetry with respect to the *xz* plane is broken by applying an external magnetic field ($\boldsymbol{H_{ap}}$) along the *x*-direction. By fixing the direction of $\boldsymbol{H_{ap}}$ (either positive or negative with respect to the *x*-axis), a unique perpendicular magnetization state can be chosen. **c**, The new perpendicular effective field ($\boldsymbol{H}_z^{\mathrm{FL}}$) induced by the laterally asymmetric structure, and its mirror image ($\boldsymbol{H}_z^{\mathrm{FL}\prime}$). The presence of the new perpendicular effective field, induced by the lateral symmetry-breaking, uniquely determines the *z*-component of the magnetization for a particular direction of current, thereby allowing deterministic switching without external magnetic fields. **d**, Schematic representation of the ferromagnet/oxide interface, illustrating its non-uniform oxygen content. The resulting non-uniform charge distribution may produce in-plane electric-fields (E) along the interface, which in turn can contribute to the observed zero field $\boldsymbol{H}_z^{\mathrm{FL}}$. Red spheres indicate oxygen atoms and perpendicular pink arrows correspond to the PMA in the magnetic layer.

(i) ***Mirror symmetry-breaking along z-axis only***: Figure 2.2a depicts the case where mirror symmetry is broken only along the *z*-axis (*i.e.* preserving mirror symmetries along the *x*- and *y*-axes similarly to previous works [52]) in the absence of external magnetic fields. In this case, the symmetry breaking results in current-induced SOTs, which, to quadratic order in $\boldsymbol{m}$, consist of a field-like (FL) term $\boldsymbol{T}_{\boldsymbol{c}}^{\mathrm{FL}} = \gamma H_y^{\mathrm{FL}} \boldsymbol{m} \times \boldsymbol{y}$ and a damping-like (DL) term $\boldsymbol{T}_{\boldsymbol{c}}^{\mathrm{DL}} = \gamma H_y^{\mathrm{DL}} \boldsymbol{m} \times \boldsymbol{m} \times \boldsymbol{y}$. (Notation-wise, different from section 1.5, we have added a subscript y here in order to distinguish this term from a new spin-orbit field due to additional lateral symmetry breaking, as discussed below). Here, $\boldsymbol{m}$ denotes a unit vector along the magnetization direction. Equivalently, these torques can be expressed in terms of effective magnetic fields, namely $\boldsymbol{H}_y^{\mathrm{FL}} = H_y^{\mathrm{FL}} \boldsymbol{y}$ and $\boldsymbol{H}_y^{\mathrm{DL}} = H_y^{\mathrm{DL}} \boldsymbol{m} \times \boldsymbol{y}$ (depicted in Fig. 2.2), with H_y^{FL} and H_y^{DL} representing the current-dependent

proportionality constants for each term. In this case, the absence of deterministic perpendicular magnetization switching can be understood by performing a mirror reflection with respect to the *xz*-plane on the state with perpendicular magnetization component $M_z > 0$, as illustrated in Fig. 2.2a. Under such a transformation, the direction of the current density J is unaltered. However, magnetization (being a pseudo-vector) reverses the direction of its components that is parallel to the *xz*-plane, resulting in an equilibrium state with $M_z < 0$ in the mirror state. Consequently, if a particular direction of current allows an equilibrium magnetization state with a positive *z* component, *i.e.* $M_z > 0$, the same direction of current should also favor a state with $M_z < 0$. Therefore, a given current direction does not favor a unique perpendicular magnetization orientation, and no deterministic switching is obtained. This argument suggests that in order to achieve current-induced switching of perpendicular magnetization, the mirror symmetry with respect to the *xz*-plane also has to be broken. This has been achieved in previous works using an external magnetic field H_{ap} [53] [54]along the current direction, as depicted in Fig. 2.2b. The mirror transformation in this case also reverses the external magnetic field direction. Thus, by fixing the direction of the external field along the current, the symmetry between magnetic states with opposite *z*-components of magnetization is broken, allowing for a unique magnetic state. (For the case shown, a positive/negative external field favors the state with positive/negative M_z). Formally, such a scenario has also been explained by solving for the equilibrium magnetization orientation in the presence of SOTs within a single-domain model [54].

(ii) ***Mirror symmetry-breaking along both z- and y-axes***: when the mirror symmetry along the *y*-axis is also broken, a particular direction of current can uniquely determine the *z*-component of magnetization. This is illustrated in Fig. 2.2c, where the structural asymmetry along the *y*-axis consists of a varying thickness (*i.e.* wedge shape) of the insulating layer along

this axis. The mirror transformation in this case reverses both the direction of M_z and the direction of J (with respect to the wedge), hence associating each current direction with a unique orientation of M_z. In this sense, breaking structural inversion symmetry along the lateral direction can replace the role of the external bias field. This fact is also reflected in the form of the allowed current-induced SOT terms. Using a symmetry-based phenomenology[55], similar to section 1.5, the current-induced SOT terms (up to quadratic order in $\boldsymbol{m}$) arising due to mirror asymmetry along both the *y*- and *z*-axes are given by,

$$\boldsymbol{T}_{SOT} = \gamma H_y^{\mathrm{FL}} \boldsymbol{m} \times \boldsymbol{y} + \gamma H_y^{\mathrm{DL}} \boldsymbol{m} \times \boldsymbol{m} \times \boldsymbol{y} + \gamma H_z^{\mathrm{FL}} \boldsymbol{m} \times \boldsymbol{z} + \gamma H_z^{\mathrm{DL}} \boldsymbol{m} \times \boldsymbol{m} \times \boldsymbol{z} \,. \qquad (2.1)$$

In the last two terms of Eq. (1), H_z^{FL} and H_z^{DL} parameterize the strengths of the current-induced effective fields arising from the additional inversion asymmetry, respectively representing the new FL and DL SOT terms. The new FL term gives rise to a current-induced effective field H_z^{FL} along the *z*-axis (depicted in Fig. 2.2c) and can thus facilitate current-induced deterministic switching of perpendicular magnetization in the absence of an external magnetic field[56]. In the following, we provide an experimental demonstration of this new SOT-induced perpendicular effective field and switching.

2.2.2 Experimental demonstration

Experiments were carried out on sputter-deposited Ta(5.0 nm)/$Co_{20}Fe_{60}B_{20}$(1.0 nm)/TaO_x(wedge) films. The top oxide layer was formed by first depositing a Ta film, the thickness of which was varied across the wafer, as shown in Fig. 2.3a. The TaO_x was then formed by exposing the sample to a radio-frequency O_2/Ar plasma to create a $Co_{20}Fe_{60}B_{20}/TaO_x$ interface. Due to the variation of the top Ta-layer thickness, the thickness of the resulting oxide as well as the oxygen content at the $Co_{20}Fe_{60}B_{20}/TaO_x$ interface change continuously across the wafer. The film was then patterned into an array of Hall bars, the structure of which is shown in

Figs. 2.3a and 2.3b. The transverse direction of the Hall bars (*i.e.* the *y*-axis) is along the TaO_x wedge, as shown in Fig. 2.3a, breaking the mirror symmetry with respect to the *xz*-plane. Thus, the application of a current along the Hall bars is expected to produce an out-of-plane effective magnetic field, based on the symmetry arguments discussed above.

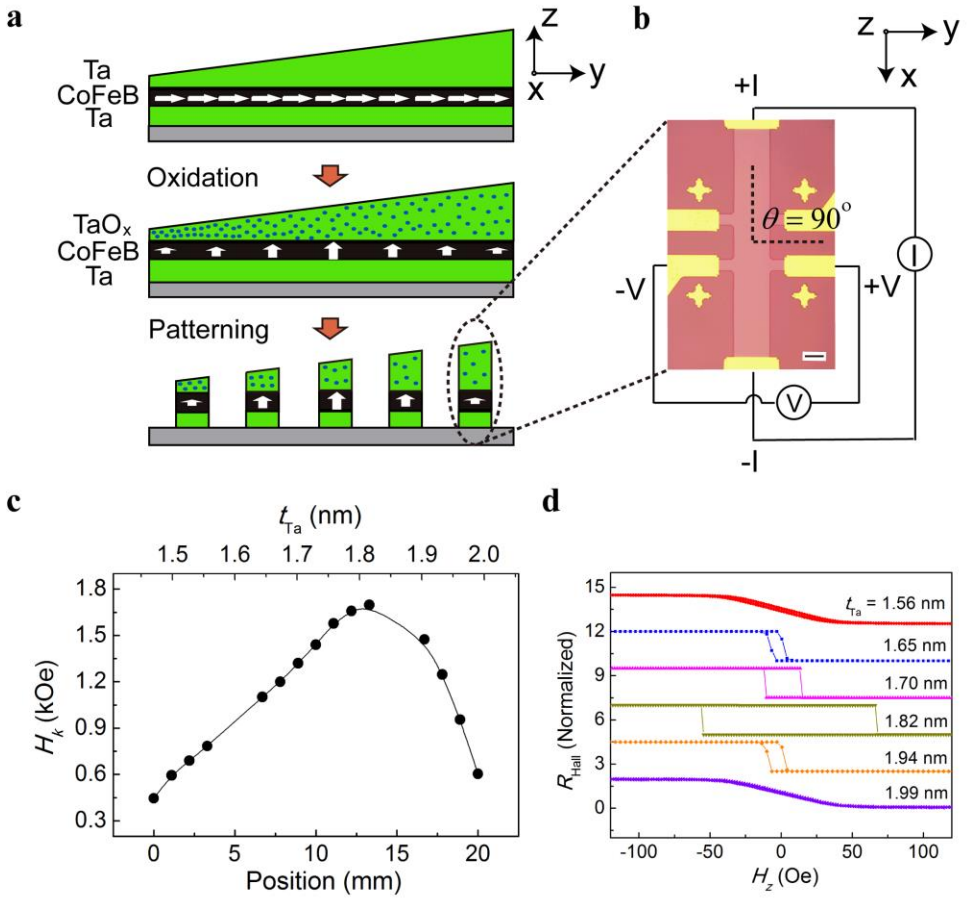

Fig. 2.3 Device geometry and magnetic perpendicular anisotropy**. a**, Procedure for growth and patterning of the devices. The Ta layer on top of the CoFeB film was deposited with a varying thickness across the wafer, resulting in a wedge shape. After the O_2/Ar plasma oxidation and annealing, nonuniform perpendicular magnetic anisotropy was realized. **b,** Structure of one device in the array (10 μm scale bar) and the measurement configuration. Each individual device is designed to have a lateral asymmetry due to the wedge in the TaO_x. **c**, Effective perpendicular anisotropy field (H_k) as a function of position/thickness of the devices. Due to the nonuniform oxidation at the interface, which depends on the thickness of the

initially deposited Ta, a non-monotonic distribution of H_k is obtained. Notice that the variation of H_k with respect to position (dH_k/dy) can be positive or negative, depending on the device location along the wedge. **d,** Perpendicular magnetization of Ta/CoFeB/TaO_x measured by extraordinary Hall effect (EHE) for the devices. A good correlation is found between the out-of-plane coercivity and H_k, obtaining a maximum coercivity near the peak of the distribution of H_k as a function of position.

The devices were characterized using extraordinary Hall effect (EHE) measurements, as shown in Fig. 2.3b. The effective perpendicular anisotropy field (H_k) of the $Co_{20}Fe_{60}B_{20}$ layer (in the absence of current-induced SOT) was determined using EHE measurements as a function of the applied in-plane magnetic field. Fig. 2.3c shows the measured H_k as a function of position along the TaO_x gradient direction. The curve shows a non-monotonic dependence of the perpendicular magnetic anisotropy (PMA) on position, indicating an increase of H_k on the thinner side ($dH_k/dy > 0$) and a decrease of H_k on the thicker side ($dH_k/dy < 0$) of the wedge. The perpendicular magnetization, measured as a function of perpendicular magnetic field, is shown in Fig. 2.3d. For devices located on the central region of the wedge with the largest H_k, the EHE perpendicular loops are square-shaped and show a large coercivity. As expected, the loops become less square-shaped and eventually turn into hard-axis-like loops on both sides of the wedge where H_k is smaller. The observed PMA is due to the interfacial magnetic anisotropy between the $Co_{20}Fe_{60}B_{20}$ film and its adjacent TaO_x and Ta layers, similar to recent reports in other material systems[57-59]. The anisotropy associated with the TaO_x interface is in turn affected by the appearance of Fe-O and Co-O bonds at the interface[58, 59], exhibiting a non-monotonic dependence on the oxygen content[60, 61]. As a result, the change of PMA across the wedge reflects the gradient of oxygen concentration at the $Co_{20}Fe_{60}B_{20}/TaO_x$ interface across the wafer.

We next performed EHE measurements on the Hall bar devices for a set of different direct currents applied along the *x*-axis. Figs. 2.4a-c show the measured EHE signals for one device (device A, t_{Ta} = 1.65 nm prior to oxidation) in the dH_k/dy > 0 region. As expected, small currents have almost no influence on the switching behavior, as shown in Fig. 2.4a. At larger currents, however, the centers of the hysteresis loops are gradually shifted to the left for currents of a positive polarity, which indicates the presence of a perpendicular effective field, $\boldsymbol{H}_z^{\mathrm{FL}} = H_z^{\mathrm{FL}}\boldsymbol{z}$ induced by the current. The value of H_z^{FL} can be extracted from the average of the positive (H_S^+) and negative (H_S^-) switching fields, *i.e.* $H_z^{FL} = -(H_S^+ + H_S^-)/2$. For currents in the opposite direction, the hysteresis loops are shifted to the right. At current values of I = ±10 mA, the separation between the two loops for this device (Fig. 2.4c) is H_z^{FL}(10 mA) − H_z^{FL}(−10 mA) ≈ 22 Oe. It is interesting to compare this to the measurements shown in Figs. 2.4d-f, which show the EHE signal for a different device (device B, t_{Ta} = 1.94 nm prior to oxidation) in the dH_k/dy < 0 region (*i.e.* on the opposite side of the anisotropy peak in Fig. 2.4c). In this case, the sign of the current-induced field is opposite to device A for the same direction of current flow. The separation between the two loops at I = ±10 mA is H_z^{FL}(10 mA) − H_z^{FL}(−10 mA) ≈ −66 Oe for device B. Thus, by comparing the H_z^{FL} of these two devices, it is evident that $H_z^{\mathrm{FL}}(I > 0)$ − H_z^{FL}(*I*

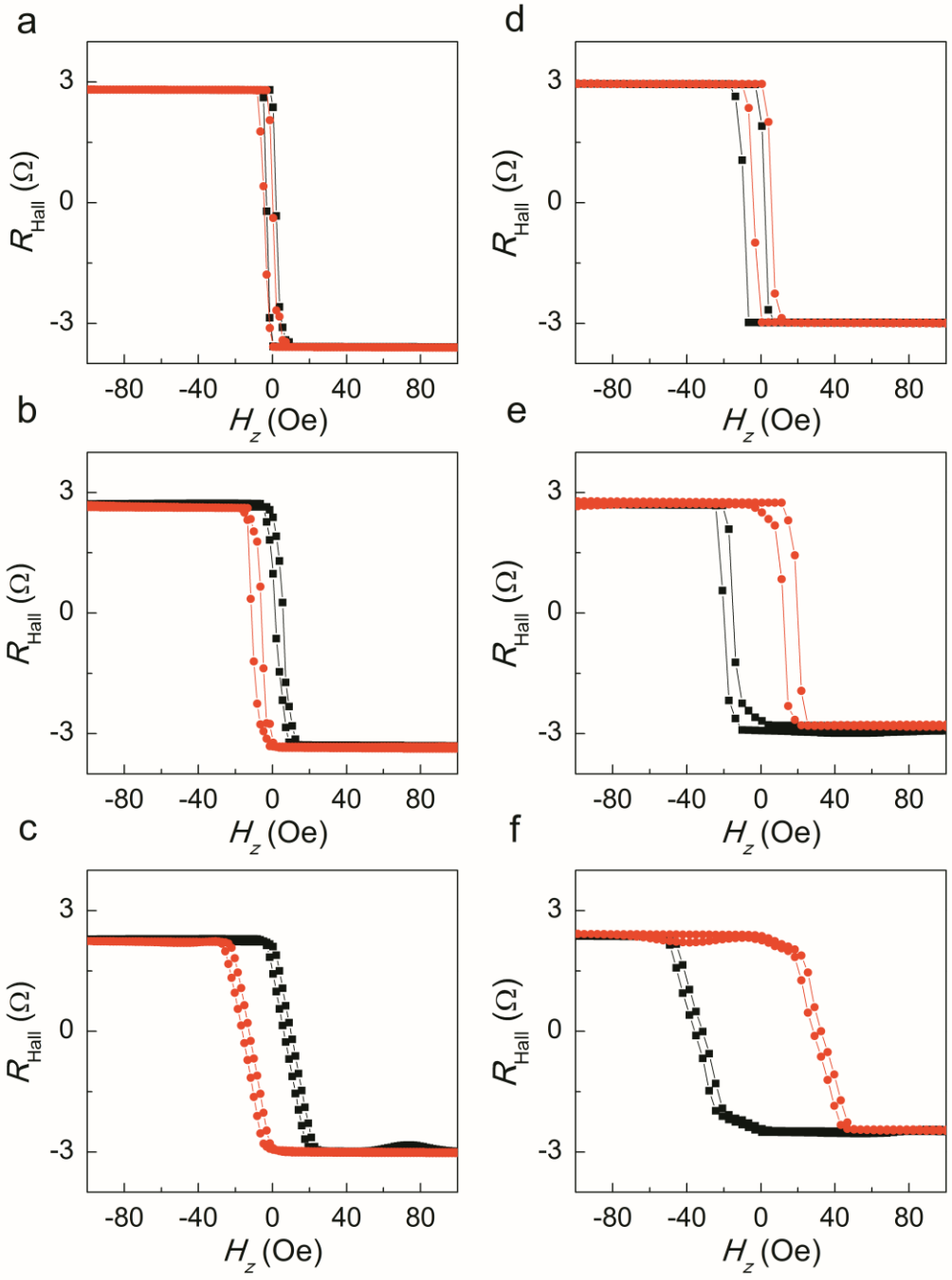

Fig. 2.4 Effect of H_z^{FL} induced by current. The figures show the perpendicular magnetization of Ta/CoFeB/TaO_x measured by EHE, while a current of ±1 mA ((**a**) and (**d**)), ±6 mA ((**b**) and (**e**)), and ±10 mA ((**c**) and (**f**)) is applied to the devices. Figures **a-c** show results for a typical device (t_{Ta} = 1.65 nm before oxidation, device A) in the $dH_k/dy > 0$ region, while **d-f** show results for a typical device (t_{Ta} = 1.94 nm before oxidation, device B) in the $dH_k/dy < 0$ region. The shift directions of the EHE loops with

respect to current, which reflect the directions of H_z^{FL} induced by the current, are opposite for these two devices with opposite signs of dH_k/dy.

< 0) > 0 [*i.e.* $dH_z^{\mathrm{FL}}/dI > 0$] in the d$H_k$/d$y$ > 0 region, while $H_z^{\mathrm{FL}}(I > 0) - H_z^{\mathrm{FL}}(I < 0) < 0$ [*i.e.* $dH_z^{\mathrm{FL}}/dI < 0$] in the d$H_k$/d$y$ < 0 region.

To quantify the H_z^{FL} induced by current, the values of H_{S}^{+} and H_{S}^{-} for the two devices(obtained from EHE loops in Fig. 2.4) are summarized in Figs. 2.5a and 2.5b, for different applied currents. The current-induced perpendicular field can then be obtained by fitting the current dependence of $H_z^{FL} = -(H_{\mathrm{S}}^{+} + H_{\mathrm{S}}^{-})/2$. Here, Fig. 2.5a corresponds to device A (dH_k/dy > 0), and Fig. 2.5b corresponds to device B (dH_k/dy < 0). For both cases, the resultant H_z^{FL} can be fitted well to a linear curve, and hence can be expressed as $H_z^{\mathrm{FL}} = \beta J$, where J is the applied current density. The values of β, extracted in a similar fashion for all devices measured along the wedge, are shown in Fig. 2.5c, with the largest absolute value of β reaching ~ 56 Oe per 10^{11}Am^{-2}. The plot also shows dH_k/dy as a function of position along the wedge for comparison. It can be seen that both the sign and magnitude of β, and hence H_z^{FL}, correspond well with dH_k/dy. Thus, in addition to the sign and magnitude of the applied current, the current-induced H_z^{FL} also depends on the sign and magnitude of dH_k/dy. This, in turn, establishes the correlation of H_z^{FL} with the symmetry-breaking along the y-axis, confirming the central hypothesis of this work.

2.2.3 Possible microscopic origin of new torque

The symmetry argument presented above does not provide any details on the microscopic mechanisms behind the current-induced shift seen in the hysteresis loops, which is characterized by a new effective perpendicular field. Hence, in addition to the new spin-orbit terms due to

lateral symmetry-breaking, in principle two other microscopic mechanisms may also contribute to the observed perpendicular switching, namely, current-induced magnetic (Oersted) fields and spin-orbit terms due to symmetry-breaking along the growth direction in conjunction with the anisotropy gradient. However, the latter two microscopic mechanisms can be ruled out in our devices, as will be explained in the following. Due to the nonuniform oxidation of the TaO_x layer, the structural asymmetry may cause the current density to be nonuniform along the width of our devices. Hence, assuming there will be a larger current density on one side (less oxidized part) of the Hall bar, this asymmetry will produce a net perpendicular magnetic field within the Hall bar area. Considering that the less oxidized part has a thicker metallic film and hence smaller resistance, for a particular current direction, this kind of Oersted field would be expected to point in the same direction for *all* Hall bars, since they all have an identical direction of the TaO_x thickness gradient. Therefore, based on the asymmetric sample structure shown in Fig. 2.3a, the Oersted field should result in a negative sign of β for all devices, which is not the case observed in our experiments. This indicates that Oersted fields are not the origin of the observed H_z^{FL} in our samples. In addition, the estimated value of the Oersted field induced by current is ~16 times smaller than the largest current-induced perpendicular shift (created by H_z^{FL}) observed in our experiments. Thus, the role of Oersted fields can be excluded.

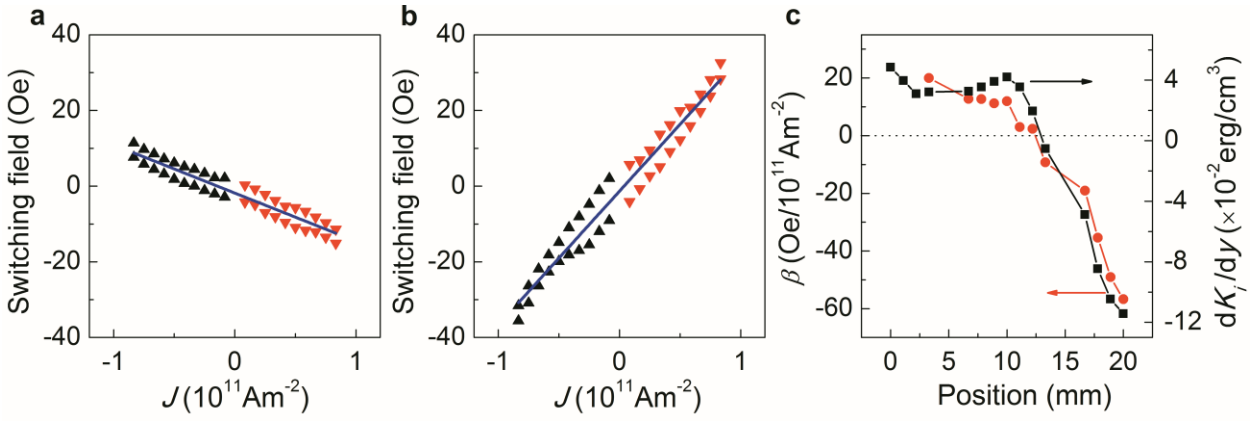

Fig. 2.5 The switching fields as a function of applied current densities, and β as a function of position of the Hall bar devices on the wafer. **a, b**, Measured switching fields as a function of current for the devices A (**a**) and B (**b**) discussed in Figure 3, with dH_k/dy = 0.09 Oe/μm and −0.24 Oe/μm, respectively. The blue lines are linear fits. The values of β, representing the perpendicular effective field ($H_z^{\mathrm{FL}} = \beta J$), are extracted from the slope. **c,** The red circles correspond to β and the black squares correspond to dH_k/dy, indicating a clear correlation between dH_k/dy and H_z^{FL}. This is in agreement with the expected relationship between lateral symmetry breaking and the strength of H_z^{FL}. The dashed line corresponds to zero for both sides of the vertical coordinates.

It should be noted that, considering the size of the present samples and the relatively low perpendicular anisotropy, the magnetization reversal process occurs via a micromagnetic reversal process, such as nucleation and propagation of domain walls. It is worth noting, however, that the symmetry-based argument presented earlier does not assume a single-domain reorientation process and is valid in the case of such micromagnetic reversal processes as well. For example, it has been shown recently that when the lateral symmetry is broken by an applied magnetic field along the current direction, fixing the magnetization in the wall, conventional SOTs can drive the domain walls resulting in deterministic switching[62]. In the present work no such magnetic field is present; however, the lateral symmetry is indeed broken by the anisotropy gradient. Thus, in principle, the presence of lateral symmetry-breaking due to an anisotropy gradient in conjunction with the conventional SOTs can result in the observed switching via a non-trivial nucleation process, an interesting phenomenon in its own right. However, we rule out this possibility by directly measuring the SOTs through independent second-harmonic measurements [63] in the presence of large external magnetic fields. The applied field was larger than the saturation field of our samples, ensuring single-domain behavior during the experiment. The results showed an

excellent agreement between the current-induced H_Z^{FL} extracted from second-harmonic measurements (i.e. where the samples were single domain) and the values extracted from hysteresis loop shifts. Based on this agreement of the two independent measurements in all tested samples, we believe that a new spin-orbit field-like torque due to lateral symmetry breaking is most likely the origin of the observations in our switching experiments.

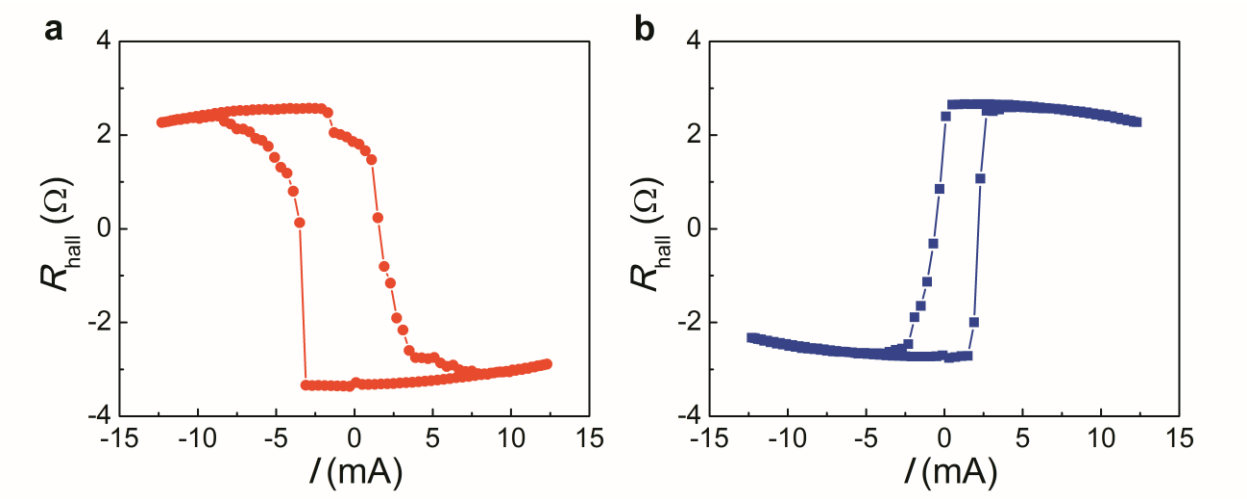

Fig. 2.6 Switching of perpendicular magnetization by current in the absence of external fields. Perpendicular magnetization as a function of direct current for device C (t_{Ta} = 1.67 nm before oxidation) (**a**) and B (t_{Ta} = 1.94 nm before oxidation) (**b**) with dH_k/dy = 0.10 and −0.24 Oe/μm, respectively. The favored magnetization direction for each current direction is opposite for these two devices, due to the opposite orientations of the current-induced H_Z^{FL}.

Microscopically, the new field-like torque appears to stem from the lateral oxidation gradient at the $Co_{20}Fe_{60}B_{20}/TaO_x$ interface, which can induce Rashba-like spin-orbit coupling with the effective electric field direction pointing along the wedging direction y. Namely, a microscopic electron Hamiltonian of the form $\mathcal{H} \sim \boldsymbol{\sigma} \cdot (\boldsymbol{y} \times \boldsymbol{p})$ [64], at the $Co_{20}Fe_{60}B_{20}/TaO_x$ interface, could in principle account for a field-like torque of the form $\boldsymbol{T^{FL}} \sim \boldsymbol{m} \times \boldsymbol{H_z^{FL}} \sim \boldsymbol{m} \times$

$(\boldsymbol{y} \times \boldsymbol{J})$. Here $\boldsymbol{\sigma}$ and $\boldsymbol{p}$ stand for the Pauli matrices and the electron's momentum operator, respectively. As shown in Fig. 2.2d, an electric field along the wedging direction could, in turn, originate from the redistribution of charges near the interface depending on the oxygen content, which is also responsible for the non-monotonic dependence of H_k on position[61]. However, a more detailed understanding of these electric fields and their possible contribution to H_z^{FL} is needed and requires first-principles calculations.

2.2.4 Current-induced switching in the absence of external fields

Finally, we demonstrate that the perpendicular effective field H_z^{FL}, induced by an in-plane current along the *x*-axis, can be used to deterministically switch the magnetization in an out-of-plane magnetized film without the assistance of external magnetic fields. This is shown in Figs. 2.6a and b for two representative devices on different sides of the H_k peak in Fig. 2.3c. We were able to reversibly switch the perpendicular magnetization by currents of ~6 mA (corresponding to a current density of 5.0×10^6 A/cm^2) for device C (t_{Ta} = 1.67 nm before oxidation) in Fig. 2.6a and by currents of ~3 mA (corresponding to a current density of 2.5×10^6 A/cm^2) for device B in Fig. 2.6b. For the first device, which is in the $\mathrm{d}H_k/\mathrm{d}y > 0$ region, positive currents favor a positive magnetization (resulting in a negative Hall resistance R_{Hall}). For the latter device, which is in the $\mathrm{d}H_k/\mathrm{d}y < 0$ region, positive currents favor a negative magnetization. The favored direction of magnetization for a particular current direction is dependent on the sign of β and hence depends on the location along the wedge, as expected. Thus, currents of opposite polarities can be used to switch the perpendicular magnetization in opposite directions, and the favored direction of magnetization for each current is determined by the sign of the lateral device asymmetry, as quantified by the sign of $\mathrm{d}H_k/\mathrm{d}y$. We obtained similar results for several other devices measured at different points along the wedge. Due to the correlation between $\mathrm{d}H_k/\mathrm{d}y$ and the strength of

H_z^{FL} (see Fig. 2.5c), we expect that the current density required for switching can be further reduced by increasing the value of dH_k/dy, *i.e.* by creating a larger structural asymmetry in the device. Moreover, the perpendicular H_z^{FL} can be used together with the conventional SOTs to switch the device. The conventional SOTs can in this case bring the perpendicular magnetization into the sample plane, where it is metastable[65]. The role of the new torques, in turn, would be to determine the switching direction.

For device applications, the perpendicular H_z^{FL} induced by currents in this work can be used in three-terminal structures, where the perpendicular ferromagnetic free-layer is part of a magnetic tunnel junction, allowing for readout of its state via the tunneling magnetoresistance (TMR) effect. No external in-plane magnetic fields would be needed to operate the device. It should also be noted that the nonuniform oxidation method used to create the lateral asymmetry in this work is not the only approach that could be used for this purpose. For integration into large device arrays (*e.g.* memory chips), requiring uniformity across the wafer, a more localized method of generating the lateral asymmetry may be more appropriate. We expect that this work will motivate research to develop such asymmetric device structures that exhibit and utilize perpendicular effective fields. By providing large perpendicular effective fields, in combination with the conventional SOTs, such structures could result in new ultralow-power and highly scalable SOT-based spintronic memory and logic circuits.

2.3 Ultra-low current-induced magnetization switching in topological insulator-based magnets

Besides heavy metals, topological insulators (TIs) [38, 66, 67], in which the SOC is large enough to invert the band structure [68], are expected to be the most promising candidate to

exploit the SOTs when coupled to magnetic moments [69, 70]. In addition, the recently demonstrated magnetism in magnetically doped TIs (*e.g.*, Cr-doped TIs) [71-75]makes it accessible to study the SOTs in the TI/magnetic-TI bilayer heterostructures. In this section, we demonstrate the magnetization switching by in-plane current injection into epitaxial TI/Cr-doped TI bilayer films. Most importantly, we find that the effective field to current ratio, is nearly three orders of magnitude larger than those reported in heavy metal/ferromagnetic heterostructures (HMFHs) so far, allowing to switch with *1000 times smaller currents* . This giant SOT, together with the current-induced switching behavior, suggests that magnetically doped TI heterostructures could potentially be the materials/structures to generate SOTs with efficiency beyond today's HMFHs and could bring dynamic power of spin-orbitronic devices well below transistors.

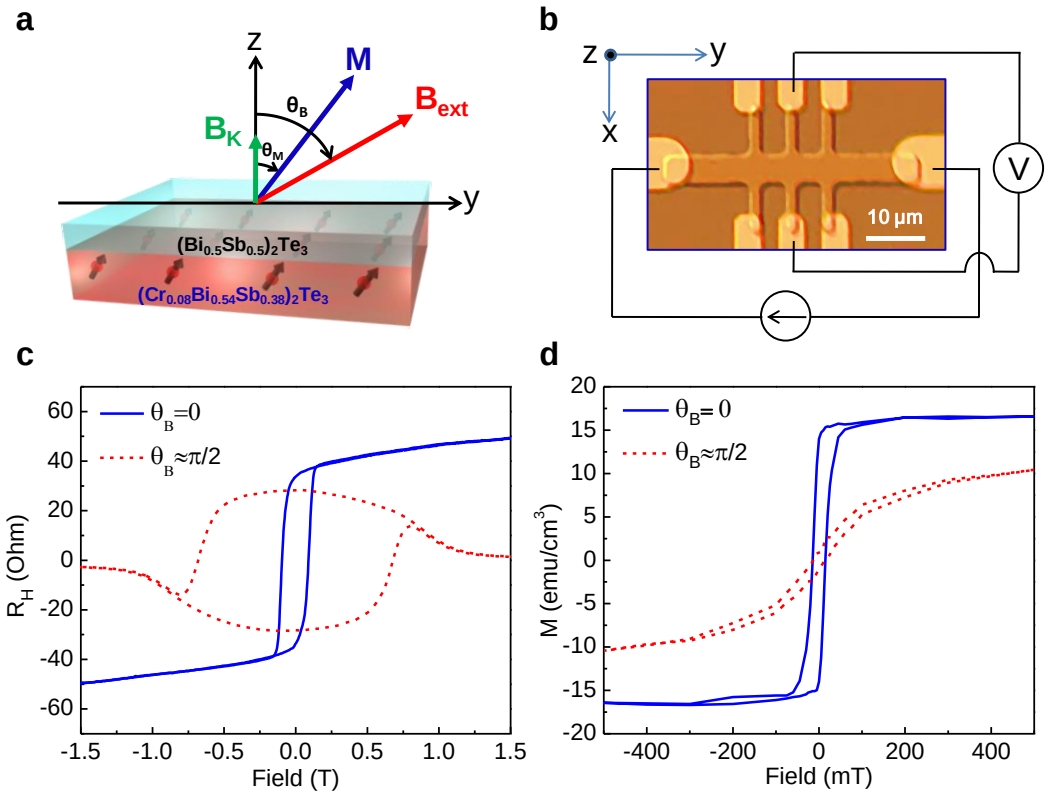

Fig. 2.7 Experimental setup and magnetic properties of the $(Bi_{0.5}Sb_{0.5})_2Te_3$ /$(Cr_{0.08}Bi_{0.54}Sb_{0.38})_2Te_3$ bilayer heterostructure. **a,** Three-dimensional schematic of the bilayer heterostructure. The top layer (light blue) shows the 3QLs $(Bi_{0.5}Sb_{0.5})_2Te_3$ and the bottom layer (light red) presents the 6QLs $(Cr_{0.08}Bi_{0.54}Sb_{0.38})_2Te_3$. $\boldsymbol{B_{ext}}$ (red arrow) represents the external magnetic field and $\boldsymbol{M}$ (blue arrow) denotes the magnetization of the bottom $(Cr_{0.08}Bi_{0.54}Sb_{0.38})_2Te_3$ layer. $\boldsymbol{B_K}$ (green arrow) is the out-of-plane anisotropy field. **b,** Micro-graph of the Hall bar device with schematic illustration of the Hall measurement set-up. The width of the Hall bar and the length between two neighboring Hall contacts are both 5 μm. **c,** The Hall resistance as a function of the applied external magnetic field for both the out-of-plane ($\theta_B = 0$) and nearly in-plane ($\theta_B \approx \pi/2$) directions, respectively, at 1.9K. **d,** SQUID measurement of the magnetization for both the out-of-plane ($\theta_B = 0$) and in-plane ($\theta_B \approx \pi/2$) directions, respectively, at 5K for external magnetic fields up to ±500mT.

2.3.1 Material system: asymmetric magnetic topological insulator

Epitaxial $(Bi_{0.5}Sb_{0.5})_2Te_3$ /$(Cr_{0.08}Bi_{0.54}Sb_{0.38})_2Te_3$ bilayer films are first grown on an insulating GaAs (111) substrate using the modulation-doped molecular beam epitaxy (MBE) growth method [71], as illustrated in Fig. 2.7a. The top $(Bi_{0.5}Sb_{0.5})_2Te_3$ layer thickness is chosen to be 3 quintuple layers (QLs) while the bottom $(Cr_{0.08}Bi_{0.54}Sb_{0.38})_2Te_3$ layer is 6 QLs, with atomically sharp hetero-interfaces. In this structure, the Bi/Sb ratio is adjusted to 0.5/0.5 in the top $(Bi_{0.5}Sb_{0.5})_2Te_3$ layer and 0.59/0.41 in the bottom $(Cr_{0.08}Bi_{0.54}Sb_{0.38})_2Te_3$ layer so that both layers display similar conductivities (222.7 S/cm and 219.5 S/cm, respectively), which guarantees a uniform current distribution inside the entire structure.

Pronounced ferromagnetism has recently been reported in $(Cr_xBi_ySb_{1-x-y})_2Te_3$ films, and with an appropriate doping concentration, the quantum anomalous Hall phase [37] is also obtained. To investigate the SOTs in our TI/Cr-doped TI heterostructure, micrometer-size Hall

bar devices were prepared, as shown in Fig. 2.7b. When applying a large enough external magnetic field $\boldsymbol{B_{ext}}$ in the yz-plane, the magnetization $\boldsymbol{M}$ becomes polarized, and the relative positions between $\boldsymbol{B_{ext}}$ and $\boldsymbol{M}$ are illustrated in Fig. 2.7a, where θ_B and θ_M are the polar angles of $\boldsymbol{B_{ext}}$ and $\boldsymbol{M}$ from the z-axis, respectively. Here, $\boldsymbol{B_K} = K\cos\theta_M \hat{\boldsymbol{z}}$ is the out-of-plane anisotropy field with K the anisotropy coefficient in the material is found to be around 0.9 Tesla (T) by measuring the field required to saturate the sample in-plane.

Field-dependent Hall resistance measurements of the TI/Cr-doped TI bilayer heterostructure for both the out-of-plane ($\theta_B = 0$) and nearly in-plane ($\theta_B \approx \pi/2$) directions were carried out at 1.9 K, and the results are displayed in Fig. 2.7c. The nearly square-shape magnetic hysteresis loop of R_H at $\theta_B = 0$ clearly suggests that the magnetization easy axis is out-of-plane (*i.e.*, along the z-direction). In addition, superconducting quantum interference device (SQUID) measurements were carried out to directly probe the magnetization $\boldsymbol{M}$ for both the out-of-plane ($\theta_B = 0$) and in-plane ($\theta_B \approx \pi/2$) directions, and the results are shown in Fig. 2.7d. The saturation magnetization M_S is measured to be around 16 emu/cm^3 along the out-of-plane ($\theta_B = 0$) direction for applied magnetic fields greater than 100 mT. In contrast, $\boldsymbol{M}$ does not show any saturation behavior even when $|\boldsymbol{B_{ext}}| > 500$ mT for fields along the in-plane ($\theta_B \approx \pi/2$) direction, again indicating the robust out-of-plane magnetic anisotropy of our TI/Cr-doped TI heterostructure sample.

2.3.2 Current-induced magnetization switching

Similar to the heavy metal case discussed in section 2.2, in our conductive TI/Cr-doped TI bilayer heterostructure, a dominant spin accumulation in the Cr-doped TI layer with spin polarized in the transverse direction is expected when passing a charge current in the y-direction

due to the SHE in the bulk and the spin polarization arising from the Rashba-type interactions at the interfaces. A strong enhancement of the interfacial spin accumulation can be expected due to the spin-momentum locking of the topological surface states [76]. The accumulated spins' angular momentum can be directly transferred to the magnetization $\boldsymbol{M}$ and therefore affect its dynamics. In particular, such a SOT can be described as (see section 1.5), $\boldsymbol{\tau} = -\gamma \boldsymbol{M} \times \boldsymbol{H_I}$, where the effective spin-orbit field is, $\boldsymbol{H_I} = I\lambda_{SO}\hat{\boldsymbol{x}} \times \boldsymbol{m}$ (note that here we have defined field opposite to the convention in section 2.2, this is to make measured coefficient λ_{SO} positive) . Here γ is

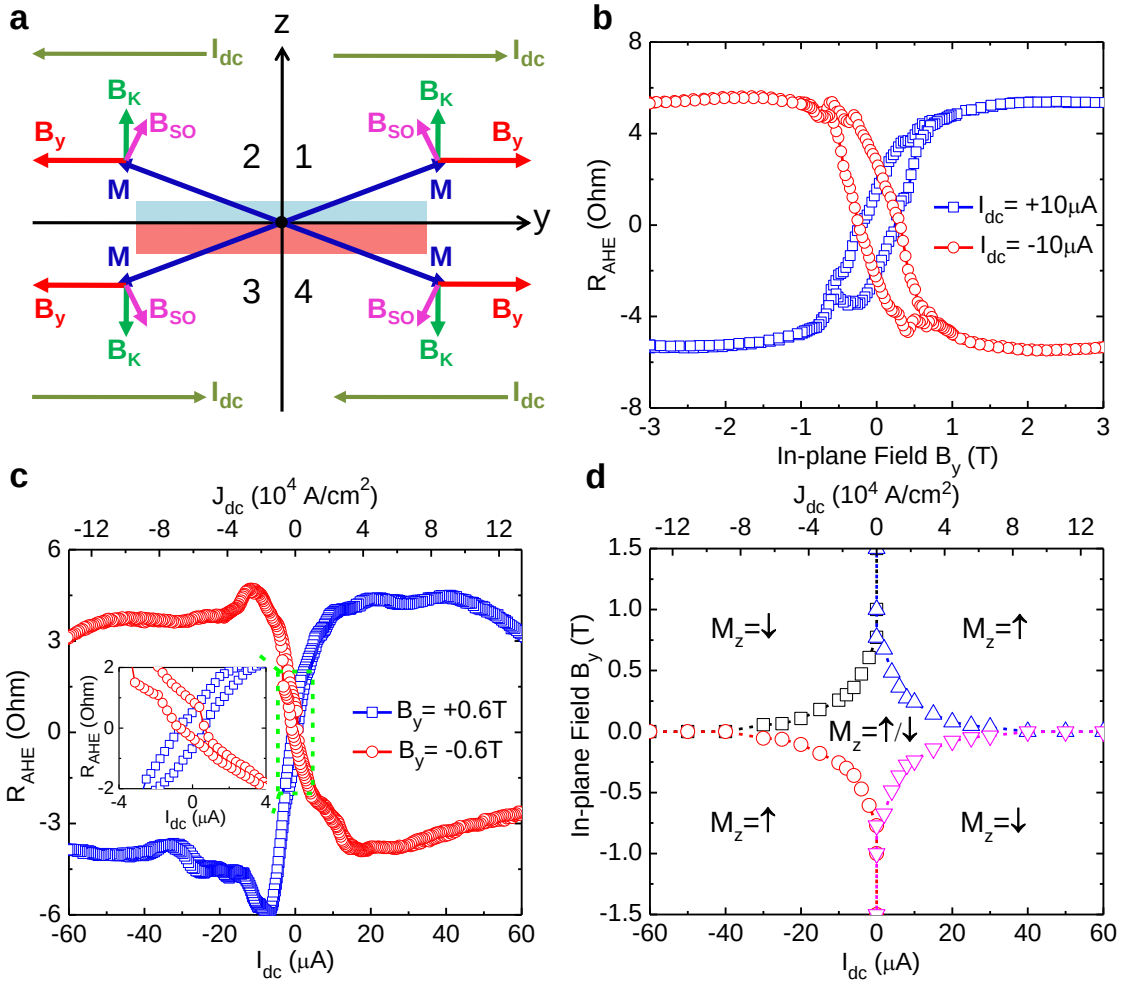

Fig. 2.8 Magnetization switching due to the SOT induced by an in-plane DC current**. a,** Schematic of the four stable magnetization states (panels 1-4) when passing a large DC current, I_{dc}, and applying an in-

plane external magnetic field, $\boldsymbol{B_y}$, in the $\pm y$ directions. The effective spin-orbit field $\boldsymbol{B_{SO}}$ induced by the DC current and the anisotropy field $\boldsymbol{B_K}$ are both considered. **b,** The AHE resistance R_{AHE} as a function of the in-plane external magnetic field when passing a constant DC current with $I_{\rm dc} = +10\mu$A (blue squares) and $I_{\rm dc} = -10\mu$A (red circles) along the Hall bar, respectively, at 1.9K. **c,** Current-induced magnetization switching in the Hall bar device at 1.9K in the presence of a constant in-plane magnetic field with $B_y = +0.6$T (blue squares) and $B_y = -0.6$T (red circles), respectively. Inset: expanded scale to show the hysteresis windows. **d,** Phase diagram of the magnetization state in the presence of an in-plane external magnetic field $\boldsymbol{B_y}$ and a DC current $I_{\rm dc}$. The dashed lines and symbols (obtained from experiments) represent switching boundaries between the different states. In all panels, the symbol ↑ means $M_z > 0$ and ↓ means $M_z < 0$, not $M_z = \pm M_S$.

the gyromagnetic ratio, λ_{SO} is the coefficient characterizing the SOC strength in the system, I is the charge current conducting along the longitudinal direction and $\boldsymbol{m}$ is the unit vector denotes the magnetization direction. Note that we have only included the damping-like SOT as the field-like SOT term is found to be order of magnitude smaller in our structure, via an independent measurement. Accordingly, we illustrate the four stable states in Fig. 2.8a where the applied DC current, $I_{\rm dc}$, conducts along the longitudinal direction (*i.e.*, $\pm y$-axis), and the external magnetic field is also applied along the $\pm y$-axis. In panel 1 of Fig. 2.8a, for example, we show the case where the DC current, $I_{\rm dc}$, and the in-plane external magnetic field, $\boldsymbol{B_y}$, are both applied along the $+y$-axis. The effective damping-like field is pointing along the tangential $-\widehat{\boldsymbol{\theta}}$ direction of $\boldsymbol{M}$, which tilts $\boldsymbol{M}$ up to obtain a positive z-component, M_z, when in equilibrium. The other three cases for different configurations of the applied $I_{\rm dc}$ and $\boldsymbol{B_y}$ are illustrated in the panels 2-4 of Fig. 2.8a, correspondingly. To summarize, in the presence of a constant external magnetic field in the y-direction, the z-component magnetization M_z can be switched, depending on the DC

current conduction direction; likewise, when the applied DC current is fixed, M_z can also be switched by changing the in-plane external magnetic field.

Based on such a scenario, we carried out the (I_{dc}-fixed, $\boldsymbol{B_y}$-dependent) and the ($\boldsymbol{B_y}$-fixed, I_{dc}-dependent) experiments at 1.9K; the results are shown in Fig. 2.8b and 2.8c, respectively. Specifically, when $I_{\mathrm{dc}} = +10\mu\mathrm{A}$ (blue squares in Fig. 2.8b), the AHE resistance R_{AHE} goes from negative to positive as the applied in-plane magnetic field $\boldsymbol{B_y}$ gradually changes from $-3\mathrm{T}$ to $3\mathrm{T}$, indicating the z-component magnetization M_z switches from $-z$ to $+z$. In contrast, when $I_{\mathrm{dc}} = -10\mu\mathrm{A}$, the AHE resistance reverses sign (red circles in Fig. 2.8b) and M_z varies from $+z$ to $-z$ as $\boldsymbol{B_y}$ is swept from $-3\mathrm{T}$ to $3\mathrm{T}$. It should be noted that in both cases the AHE resistance hysteresis loops agree well with our proposed scenario. At the same time, when we scan the DC current I_{dc} at a given fixed magnetic field, we also observe similar magnetization switching behavior: the AHE resistance R_{AHE} changes from negative to positive for $B_y = +0.6\mathrm{T}$ (blue squares in Fig. 2.8c), but reverses its evolution trend, *i.e.*, changes from positive to negative, for $B_y = -0.6\mathrm{T}$ (red circles in Fig. 2.8c). For this case, the small hysteresis window in R_{AHE} is clearly visible on expanded scale as shown in the inset of Fig. 2.8c. Consequently, both the (I_{dc}-fixed, $\boldsymbol{B_y}$-driven) and ($\boldsymbol{B_y}$-fixed, I_{dc}-driven) magnetization switching behaviors clearly demonstrate that the magnetization can be effectively manipulated by the current-induced SOT in our TI/Cr-doped TI bilayer heterostructure. We summarize these switching behaviors in the phase diagram in Fig. 2.8d. For the four corner panels in Fig. 2.8d where the field value B_y and I_{dc} are large, the magnetization state is deterministic; however, in the central panel where B_y and I_{dc} are small, both magnetization states, up and down, are possible; this behavior agrees with the hysteresis windows, as shown in Fig. 2.8b and 2.8c, where in the low B_y and small I_{dc} region the two magnetization states are both allowed. Based on this phase diagram, it

can be clearly seen that the magnetization can be easily switched with only tens of μA DC current (*i.e.*, below 8.9×10^4 A/cm^2 in current density J_{dc}), suggesting that the current-induced SOT in our TI/Cr-doped TI bilayer heterostructure is quite efficient.

This giant SOT observed in our TI/Cr-doped TI bilayer heterostructure is attributed to the strong SOC interaction in the whole structure and the coexisting magnetism, in conjunction with the breaking of the reflection symmetry in the growth direction by Cr-doping. The topological surface states may play an important role in the current-induced SOT because of the spin-momentum locking mechanism which is expected to be a much more efficient way to generate spin current compared with heavy metals. The role of the topological surface states and the various associated spin-galvanic/magneto-electric phenomena discussed in refs. [77] warrant additional and more elaborate experiments.

The challenge remaining for this direction is to construct a room temperature material system. Note that this is not a fundamental problem.The reason the measurements in the present system are restricted to cryogenic temperatures is that the dilute magnetic system created has a low Curie temperature. Exploring interfaces with topological insulator with ferromagnetic insulators could provide the required breakthrough and deserves future experimentation.

CHAPTER 3: SOT-induced creation and motion of solitons

The contents of this chapter are adapted from work originally published in Ref. [78-80]

3.1 Motivation

In this chapter we go beyond the single domain magnetization switching, focusing on SOT-induced manipulation of a collection of spins, which behave like particles, i.e. can be moved around maintaining their configuration. In general, such particle-like solutions are known as solitons. The first known description of soliton dates back to 1834, when John Scott Russell noted a water-wave front moving without distortion to long distance in the Union Canal in Scotland [81]. From then solitons have been found everywhere in nature with examples spanning from bubble-rings created by dolphins and smokers to impulses created in brain and the field of optics for communication. The appeal of solitons is that they can be used to carry useful information without distortion to long distances.

In magnetism, this fact was utilized in the 1970-80's to create a magnetic-bubble memory, where a circular domain with magnetization pointing in a direction opposite to the rest of the film (see Fig.3.1F closed domain schematic, referred to as magnetic bubble) was used to store information which was moved around using magnetic-field gradients [82]. However, because of the large dynamic power (due to the use of magnetic fields for manipulation of bubbles) and larger size of these objects, bubble memory could not compete with its charge-based analogs. Motivated by this, recently STT-induced motion of another magnetic soliton, referred to as the domain wall (which is a region of transition of magnetization vector oriented in two different directions, see Fig. 3.1A), has been similarly proposed for both memory [83] and logic [84] applications. However, the current level involved in inducing motion of domain walls have also

remained notoriously high requiring alternate low power mechanisms. One major issue for this high current requirement is that these solitons tend to pin to impurities in the sample. More recently, spin-orbit interaction has been shown to move, with orders of magnitude lower depinning currents, a particular class of solitons which are topologically non-trivial (to be made precise below) magnetization configuration, known as skyrmions, stabilized at low temperatures.

In this chapter, motivated by reducing energy consumption for beyond memory applications, we demonstrate theoretically and experimentally SOT-induced manipulation of magnetic solitons at *room temperature*. Specifically, first utilizing inhomogeneous current-induced SOT we create skyrmions, much like blowing bubbles out of a thin soap-film, and then we demonstrate its motion for the first time at room temperature. Next, we theoretically combine effect of voltage- and current-induced SOT demonstrating guiding of skyrmions by electric field, which is used to construct proof of principle of a transistor- and multiplexer-like functions based on skyrmions. Finally, for domain-wall solitons we remove the need for power hungry currents completely showing theoretical motion of domain walls by voltage-induced SOT.

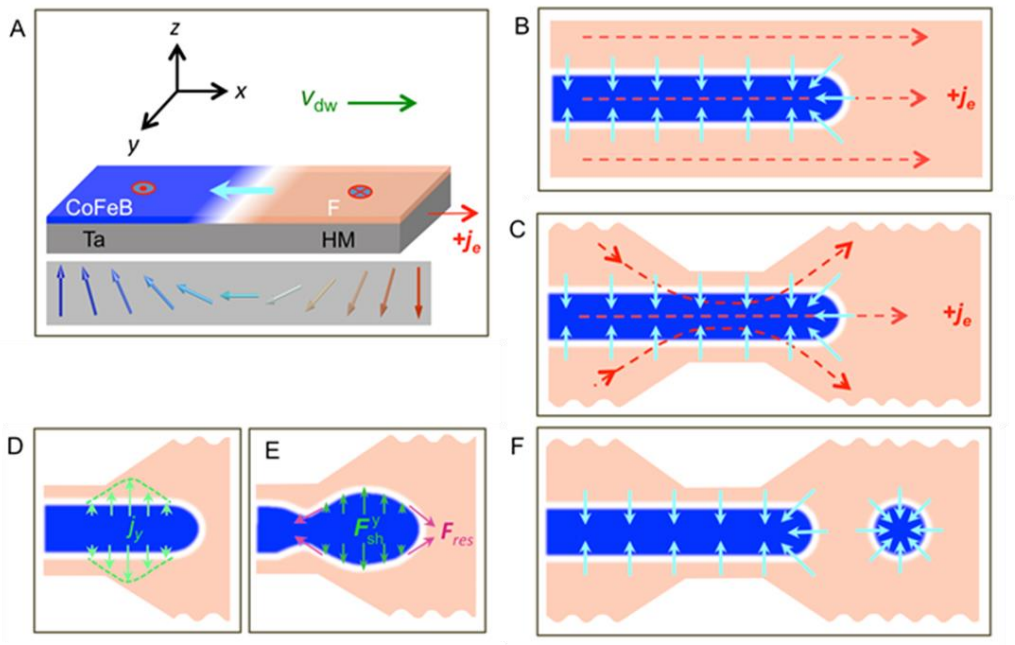

Fig. 3.1 Schematic of the transformation of stripe domains into magnetic skyrmion bubbles. (A) Infinitesimal section of a chiral DW in a ferromagnet (F) / heavy metal (HM) bilayer illustrating the relationship between local magnetization vectors and the SOT-induced chiral DW motion of velocity V_{dw} in a device with a homogeneous electron current flow j_e along the $+x$ axis. Blue color corresponds to upward orientation of magnetization, while orange color is the downward orientation of magnetization. Bottom panel illustrates the magnetization directions inside of the Néel wall. (B) Top view of a trilayer device. The blue region is a stripe-shaped domain. Light blue arrows show the in-plane magnetization direction of the DW (as shown in the bottom panel of A) and indicate that the domain has left-handed chirality. The red arrows correspond to the current distribution. (C) Introducing a geometrical constriction into the device gives rise to an inhomogeneous current distribution, which generates a flow along the *y*-axis, j_y around the narrow neck. This current distribution is spatially divergent to the right and convergent to the left of the constriction. The *y*-component of the current distribution is highlighted in (D). This introduces an effective spin Hall force $\boldsymbol{F}_{sh}^{y}$ along the *y*-axis that (E) locally expands the stripe domain on the right side. (F) Once the expansion approaches a critical point, the resultant restoring forces $\boldsymbol{F}_{res}$ associated with the surface tension of the DWs, are no longer able to maintain the shape and the stripe domains break into circular bubble domains, resulting in the formation of synthetic Néel skyrmions.

3.2 Blowing magnetic skyrmion bubbles

The structure of interest in this chapter is same as discussed in section 2.2, i.e. NM/F/I. The ferromagnet has an easy axis along the growth direction resulting in an out of plane domain wall. Central to the creation of skyrmions is to understand how electric currents can manipulate a chiral magnetic domain wall (DW), i.e., the chirality of the magnetization rotation (as shown in Fig. 3.1A) is identical for every domain wall. This fixed chirality is stabilized by the interfacial DMI, as discussed in section 1.5. In addition, when a current is passed through the heavy metal,

the damping-like component of current-induced SOT, as discussed in section 1.5 can be written as:

$$\boldsymbol{H^{DL}} = H^{DL}\left(\hat{m} \times (\hat{z} \times \hat{j}_e)\right) \qquad 3.1$$

where $\hat{m}$ is the magnetization unit vector, $\hat{z}$ is the unit vector normal to the film plane and $\hat{j}_e$ is the direction of electron particle flux. In the material system discussed in the current chapter, the microscopic mechanism of spin-Hall effect is thought to be a dominant mechanism for generating this damping-like component. Following this observation, we denote here H^{DL} by B^{sh}, which can, in turn, be written as $B^{sh} = (\hbar/2|e|) \cdot \left(\theta_{sh} J_c / t_f M_s\right)$, where $\hbar/2$ is the spin of an electron, e is the charge of an electron, t_f is the thickness of the ferromagnetic layer, and M_s is the saturation (volume) magnetization. The spin Hall angle $\theta_{sh} = J_s/J_c$ is defined by the ratio between spin current density (J_s) and charge current density (J_c). For homogeneous current flow along the *x* axis (Fig. 3.1B), a chiral SOT enables efficient DW motion [85-87]. In the case of a stripe domain with a chiral DW (Fig. 3.1B), the symmetry of Eq. 1 leads to a vanishing torque on the side walls parallel to the current and therefore only the end of the stripe domain is moved; if the opposite end is pinned, this results in an elongation of the stripe.

The situation becomes more complex when the stripe domain is subjected to an inhomogeneous current flow. This can be achieved by introducing a geometrical constriction into a current-carrying trilayer wire (Fig. 3.1C). Such a constriction results in an additional current component along the *y* axis - j_y around the narrow neck (Fig. 3.1D). The total current *j* is spatially convergent/divergent to the left/right of the constriction. Consequently, inhomogeneous effective forces on the DWs (caused by the spin Hall field) are created along the *y* axis - $\boldsymbol{F}_{sh}^{y}$, these forces act to expand the end of the domain (Fig. 3.1E). As the domain end continually expands its radius the surface tension in the DW (resulting from the increasing DW energy

determined by the combination of exchange and anisotropy fields) increases [88], which results in breaking the stripes into circular domains (Fig. 3.1F).

This process resembles how soap bubbles develop out of soap films upon blowing air through a straw, or how liquid droplets form in fluid flow jets [89]. Because of the interfacial DMI in the present system, the spin structures of the newly formed circular domains maintain a well-defined (left-handed) chirality [90-93]. These created synthetic hedgehog (Néel) skyrmions [91, 93], once formed, are stable thanks to topological protection and move very efficiently following the current direction, a process that can be described based on a modified Thiele equation [94]. The dynamic skyrmion conversion could, in principle, happen at the other side of device where the spatially convergent current compresses stripe domains. However, sizeable currents/SOTs are required to compensate the enhanced (repulsive) dipolar interaction. The proposed mechanism differs from a recent theoretical proposal with similar geometry, where skyrmions are formed from the coalescence of two independent DWs extending over the full width of a narrow constriction at a current density $\approx 10^8$ A/cm^2 [95]. For repeated skyrmion generation, this latter mechanism requires a continuous generation of paired DWs in the constriction, which is inconsistent with the experimental observations described below.

3.2.1. Experiment : Transforming chiral stripe domains into skyrmions.

We demonstrate this idea experimentally with a Ta(5nm)/$Co_{20}Fe_{60}B_{20}$(CoFeB)(1.1nm)/TaO_x(3nm) trilayer grown by magnetron sputtering [96, 97] and patterned into constricted wires via photolithography and ion-milling [98]. The wires have a width of 60 μm with a 3-μm wide and 20-μm long geometrical constriction in the center. Our devices are symmetrically designed across the narrow neck to maintain balanced

demagnetization energy. A polar magneto-optical Kerr effect (MOKE) microscope in a differential mode [99] was utilized for dynamic imaging experiments at room temperature. Before applying a current, the sample was first saturated at positive magnetic fields and subsequently at a perpendicular magnetic field of $B_{\perp}$ = +0.5 mT, sparse magnetic stripe and bubble domains prevail at both sides of the wire (Fig. 3.2A). The lighter area corresponds to negative perpendicular magnetization orientation and darker area corresponds to positive orientation, respectively.

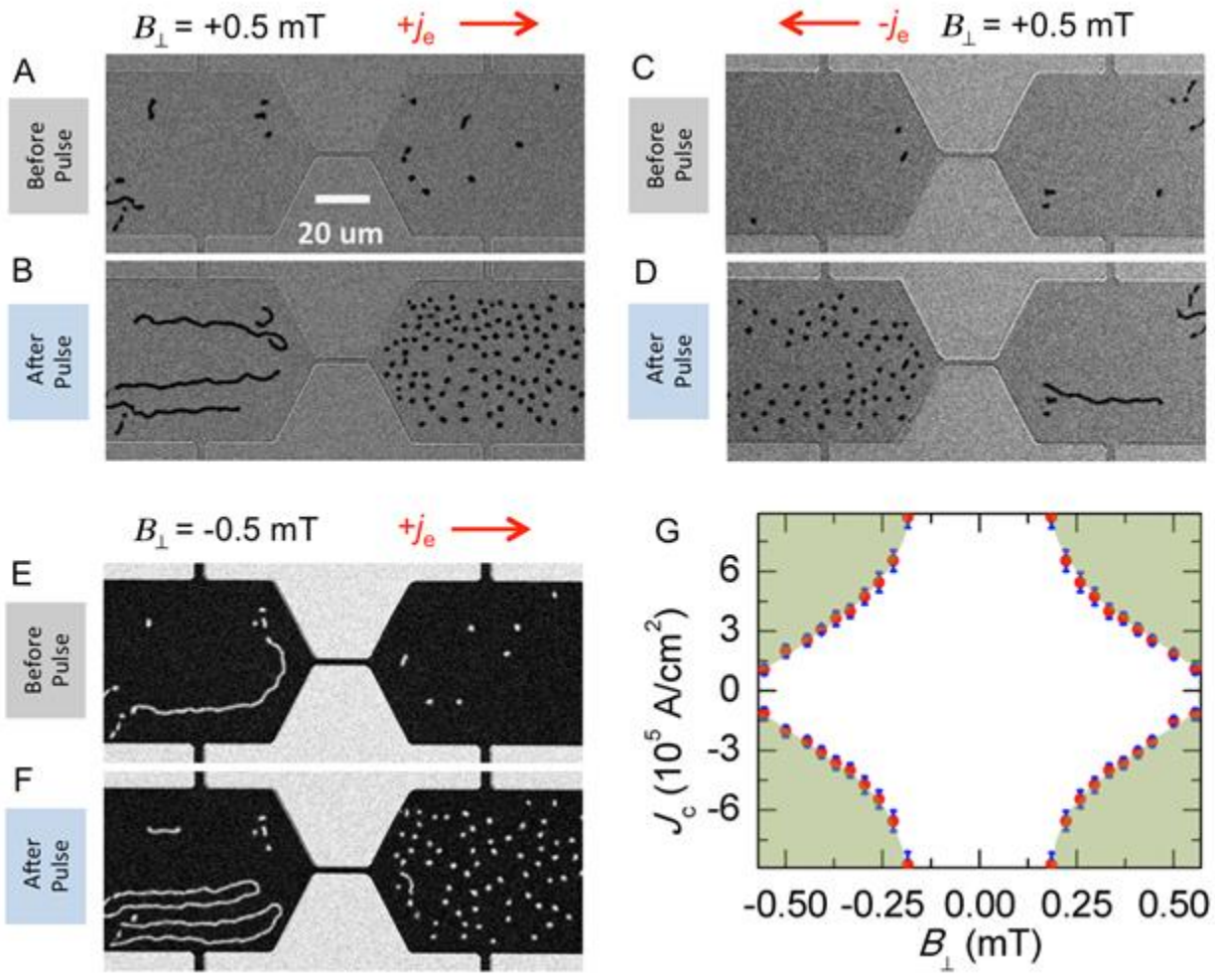

Fig. 3.2 Experimental generation of magnetic skyrmions. (A) Sparse irregular domain structures are observed at both sides of the device at a perpendicular magnetic field of $B_{\perp}$ = +0.5 mT. (B) Upon passing

a current of j_e = +5×10^5 A/cm^2 through the device, the left side of the device develops predominantly elongated stripe domains, while the right side converts into dense skyrmion bubbles. (C)–(D) By reversing the current direction to j_e = -5×10^5 A/cm^2, the dynamically created skyrmions are forming at the left side of device. (E)–(F) Changing the polarity of external magnetic field reverses the internal and external magnetization of these skyrmions. (G) Phase diagram for skyrmion formation. The shaded area indicates field/current combinations that result in the persistent generation of skyrmions after each current pulse.

In contrast to the initial magnetic domain configuration, after passing a 1 s single pulse of amplitude j_e = +5×10^5 A/cm^2 (normalized by the width of device – 60 μm), it is observed that the stripe domains started to migrate, subsequently forming extended stripe domains on the left side. These domains were mostly aligned with the charge current flow and converged at the left side of constriction. The stripes were transformed into skyrmion bubbles immediately after passing through the constriction (Fig. 3.2B). These dynamically created skyrmions, varying in size between 700 nm and 2 μm (depending on the strength of the external magnetic field), are stable and do not decay on the scale of a typical laboratory testing period (at least 8 hours). The size of the skyrmions is determined by the interplay between Zeeman, magnetostatic interaction and interfacial DMI. In the presence of a constant electron current density of j_e = +5×10^5 A/cm^2, these skyrmions are created with a high speed close to the central constriction and annihilated/destroyed at the end of the wire. Capturing the transformation dynamics of skyrmions from stripe domains is beyond the temporal resolution of the present setup. Reproducible generation of skyrmions is demonstrated by repeating pulsed experiments several times [98]. Interestingly, the left side of the device remains mainly in the labyrinthine stripe domain state after removing the pulse current, which indicates that both skyrmion bubbles and stripe domains are metastable.

When the polarity of the charge current is reversed to j_e = -5×10^5 A/cm^2, the skyrmions are formed at the left side of device (Figs. 3.2, C and D). This directional dependence indicates that the spatially divergent current/SOT, determined by the geometry of the device, is most likely responsible for slicing stripe DWs into magnetic skyrmion bubbles, qualitatively consistent with the schematic presented in Fig. 3.1. At a negative magnetic field $B_\perp$= -0.5 mT and current at j_e = +5×10^5 A/cm^2 (Figs. 3.2, E and F), the reversal contrast due to opposite of inner/outer magnetization orientations are observed as compared with positive fields. We varied the external magnetic field and charge current density systematically and determined the phase diagram for skyrmion formation shown in Fig. 3.2G. A large population of synthetic skyrmions is found only in the shadowed region, whereas in the rest of phase diagram, the initial domain configurations remain either stationary or flowing smoothly, depending on the strength of current density, as discussed below. This phase diagram is independent of pulse duration for pulses longer than 1 μs. It should be mentioned that no creation of skyrmions in regular shaped device with a homogeneous current flow (as illustrated in Fig. 3.1B) is observed up to a current density of j_e = +5×10^6 A/cm^2.

3.2.2 Capturing the transformation process

The conversion from chiral stripe domains into magnetic skyrmions can be captured by decreasing the driving current, which slows down the transformational dynamics. Figs. 3.3, A-D show the dynamics for a constant *dc* current density of j_e = +6.4×10^4 A/cm^2 at $B_\perp$= +0.46 mT. The original (disordered) labyrinthine domains on the left side squeeze to pass through the constriction (Fig. 3.3B). The stripe domains become unstable after passing through the constriction and are eventually converted into skyrmions on the right side of the device, as

shown in Figs. 3.3, C and D. Because the *x*-component of the current results in an efficient motion of DWs, the skyrmion formation can happen away from the constriction. The synthetic skyrmions do not merge into stripe domains and in fact repel each other, indicating their topological protection as well as magnetostatic interactions.

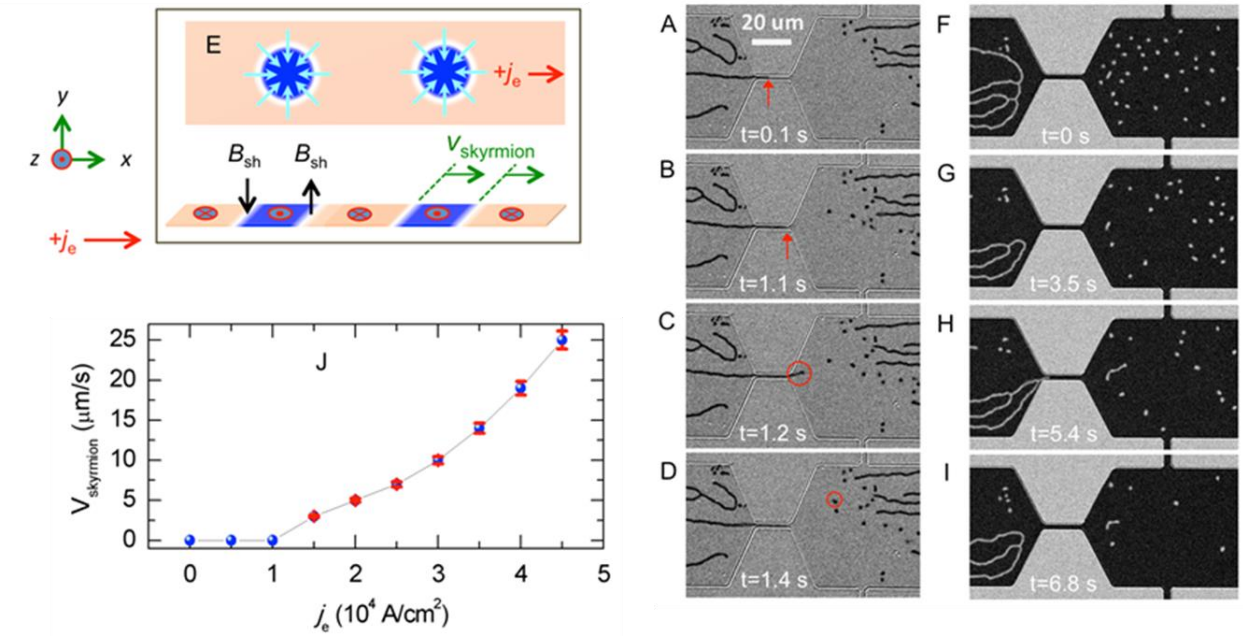

Fig. 3.3 Capturing the transformational dynamics from stripe domains to skyrmions and motion of skyrmions. (A)–(D) At a constant *dc* current j_e = +6.4×10^4 A/cm^2 and $B_\perp$ = +0.46 mT, the disordered stripe domains are forced to pass through the constriction, and are eventually converted into skyrmions at the right side of the device. Red circles highlight the resultant newly-formed skyrmions. (E) Illustration of the spin-Hall effective field acting on these dynamically created skyrmions; the direction of motion follows the electron current. (F)–(I) The efficient motion of these skyrmions for a current density j_e = +3×10^4 A/cm^2. (F) First, a 1 s long single pulse j_e = +5×10^5 A/cm^2 initializes the skyrmion state. (G)–(I) Subsequently, smaller currents (below the threshold current to avoid generating additional skyrmions through the constriction) are used to probe the current-velocity relation. It is observed that these skyrmions are migrating stochastically, and moving out of the field of view. (J) The current-velocity

dependence of skyrmions is acquired by studying approximately 20 skyrmions via averaging their velocities by dividing the total displacement with the total time period.

Some important features should be noticed. There exists a threshold current j_{e-sk} = $\pm 6\times10^4$ A/cm^2 for persistently generating skyrmion bubbles from stripe domains for pulses longer than 1 μs. Above this current, the enhanced spin-orbit torques produce the instability of the DWs, which results in the continuous formation of skyrmions. The present geometry for skyrmion generation is very efficient, resulting in the observed threshold current 3 orders of magnitude smaller than suggested by previous simulation studies ($10^{7\text{-}8}$ A/cm^2) in MnSi thin films with a bulk DMI where the driving mechanism is the conventional spin transfer torque [100]. Below this threshold for continuous skyrmion generation, there is a threshold depinning current j_{e-st} = $\pm 4.1\times10^4$ A/cm^2 that produces a steady motion of stripe domains. The force (pressure) on the stripe from SOT at this current exceeds the one required to maintain its shape. When $j_{e-st} < j_e < j_{e-sk}$, the stripe domains are moving smoothly through the constriction and prevail at both sides of devices, with just the occasional formation of skyrmions.

3.2.3 Effect of topology on the dynamics:

(a) Depinning and Motion of synthesized S = 1 skyrmions

The magnetic skyrmion bubbles discussed so far have a topological charge given by the skyrmion number S = 1, as is determined by wrapping the unit magnetization vector over the sphere $S = {}^{1}/_{4\pi} \int \boldsymbol{m} \cdot \left(\partial_x \boldsymbol{m} \times \partial_y \boldsymbol{m}\right) dxdy$ [101, 102]. These S = 1 synthetic skyrmions move thanks to the opposite direction of effective SOTs on the opposite sides of the skyrmion (Fig. 3.3E). Following the initialization by a current pulse j_e = $+5\times10^5$ A/cm^2 (which is larger than the threshold current j_{e-sk} for generating skyrmions), we studied the efficient depinning and

motion of synthetic skyrmions (Figs. 3.3, F-I) at $B_\perp$ = -0.5 mT. At the current density j_e = +3×10^4 A/cm^2, there is no migration of stripe domain through the constriction (hence an absence of newly-formed skyrmions). It is however, clear to see that the previously generated skyrmions at the right side of the device are gradually moving away following the electron flow direction. During the motion, no measurable distortion of these synthetic skyrmions is observed within the experimental resolution, consistent with the well-defined chirality of the skyrmion bubble. The average velocity ($\bar{v} = \ell/\Delta t$) is determined by dividing the displacement (ℓ) with the total time period (Δt). For the present current density, the motion of synthetic skyrmion is stochastic and influenced by random pinning with an average velocity of about 10 μm/s, the current dependence of which is summarized in Fig. 3.3J. The ratio of the velocity to the applied current is comparable to what is observed for the chiral DW motion in the related systems [85, 86].

(b) Current characteristics of *S* = 0 magnetic bubbles

Because of the competition between long-range dipolar and short-range exchange interaction, a system with a weak perpendicular magnetic anisotropy undergoes a spin reorientation transition with in-plane magnetic fields that is typified by a stripe-to-bubble domain phase transition [99, 103]. Such an in-plane field induced bubble state is established by sweeping magnetic field from $B_\parallel$ = +100 mT to $B_\parallel$ = +10 mT. Current-driven characteristics of the in-plane field induced magnetic bubbles are in stark contrast to the mobile magnetic skyrmions generated from SOTs. These bubbles shrink and vanish in the presence of a positive electron current density (Figs. 3.4, A-E), or elongate and transform into stripe domains in the presence of negative electron current density (Figs. 3.4, F-J). Such a distinct difference directly indicates the

different spin structures surrounding these field induced bubbles, and thereby different skyrmion numbers.

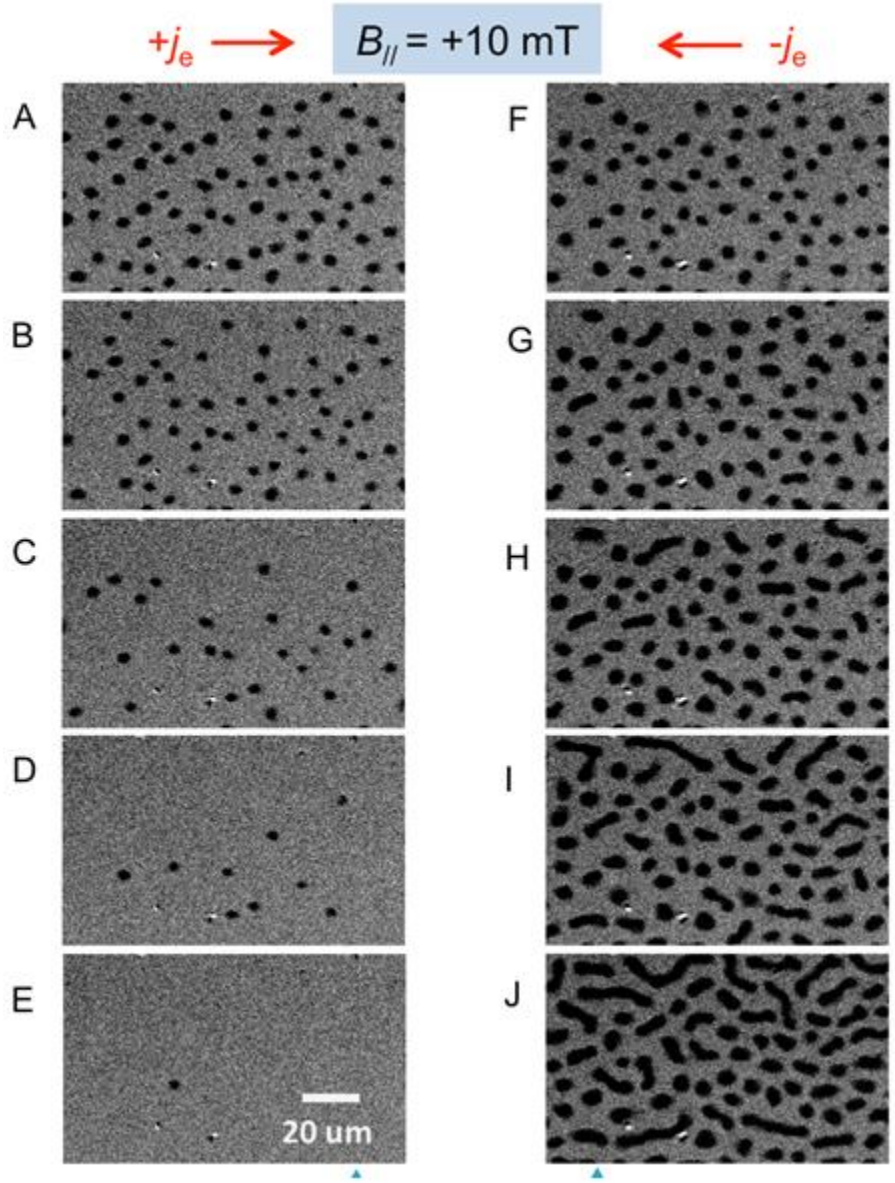

Fig. 3.4 Absence of motion for the in-plane magnetic fields stabilized S = 0 magnetic bubbles. (A) In-plane magnetic field induced bubbles are created by first saturating at in-plane field $B_{\|}$ = +100 mT and subsequently decreasing to $B_{\|}$ = +10 mT. Depending on the direction of the current, these magnetic bubbles either shrink or expand. (A) – (E) The shrinking bubbles are observed upon increasing the current

density from j_e = +5×10^4 A/cm^2 to +2.5×10^5 A/cm^2 in 5×10^4 A/cm^2 steps. (F)–(J) The expansion of bubbles is revealed for currents from j_e = -0.5×10^5 A/cm^2 to -2.5×10^5 A/cm^2 in 5×10^4 A/cm^2 steps.

For the in-plane field induced magnetic bubbles, because the spin structures of DWs follow the external magnetic fields [62, 87, 104] (Fig. 3.5), the corresponding skyrmion number is S = 0. Because of the same direction of the spin Hall effective fields given by the reversed DW orientations, topologically trivial S = 0 magnetic bubbles experience opposite forces on the DWs at opposite ends. This leads to either a shrinking or elongation of the bubbles depending on the direction of currents, which is consistent with our experimental observation. This also explains the in-plane current induced perpendicular magnetization switching in the presence of in-plane fields [62, 105].

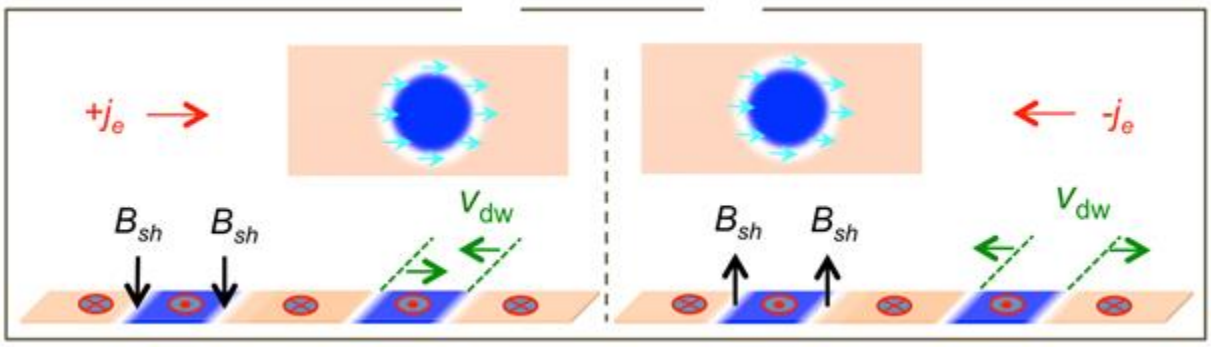

Fig. 3.5 Illustration of topology's effect on dynamics: the results are linked to the different spin textures that were stabilized along the DW by the in-plane magnetic fields, namely, S = 0 skyrmion bubbles, which lead to different orientations of the spin Hall effective fields and different directions of DW motion as illustrated.

3.2.4 Outlook for skyrmionics

Recent experimental efforts towards creating individual magnetic skyrmions use either tunnelling current from a low-temperature spin-polarized scanning tunnelling microscope [106] or geometrical confinement via sophisticated nanopatterning [107-109]. Our results demonstrate that spatially divergent current-induced SOTs can be an effective way for dynamically generating mobile magnetic skyrmions at room temperature in commonly accessible material systems. The size of these synthetic skyrmions could be scaled down by properly engineering the material specific parameters that control the various competing interactions in magnetic nanostructures [91, 92, 110]. We expect that similar instabilities will be generated from divergent charge current flows. Whereas the mechanism for synthetic skyrmion generation can be qualitatively linked to the spatially divergent spin Hall spin torque, a comprehensive understanding of this dynamical conversion, particularly at the picosecond/nanosecond time scale where the intriguing magnetization dynamics occurs, requires further experimental and theoretical investigations. Spatially divergent SOT-driven structures also offer a readily accessible model system for studying topological transitions and complex "flow" instabilities [89], where the parameters governing the flow, such as surface tension, can be systematically tuned by the magnetic interactions. At the same time, this dynamic approach for skyrmion generation in the near future could enable the demonstration of advanced skyrmionic device concepts, for example, functional skyrmion racetrack memory [91, 93, 94, 111].

3.3 Electric-field guiding of magnetic skyrmions

Having demonstrated motion of skyrmions by current-induced SOT, we now show theoretically that when combined with voltage-induced SOT these skyrmions can be guided along desired pathways. In particular, we find that for a fixed current, the electric-field (via voltage-induced SOT) can control both the speed and the direction of skyrmion motion. More

importantly, we show that by applying electric-fields in a certain pattern, defined via gated structures, skyrmions can be guided along desired trajectories. We also identify the mechanism for this electric-field control of skyrmion motion, which can be explained in terms of the change in the static properties of skyrmions, brought about by the electric-field induced modification of the micromagnetic free energy. Finally, utilizing this additional electrical knob we show that the realm of *skyrmionics* can be extended beyond the race-track-like memory applications, to possibly realize logic and computing functionalities. To this end, the structure we study theoretically is similar to the experimental structure presented in previous section (heavy metal/ferromagnet/insulator) and is depicted in Fig.3.6. The ferromagnet has a perpendicular easy axis and a skyrmion in such a film is stabilized by dipolar interactions [112] even in the absence of DMI.

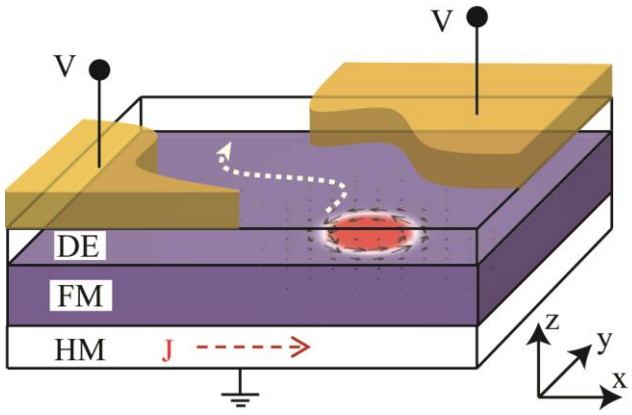

Fig. 3.6 Schematic of the system: A ferromagnet(FM) layer with a skyrmion, sandwiched between a heavy metal(HM) and a dielectric, breaking the symmetry along the z axis. A current through HM with density J drives skyrmion via SOT, while simultaneously local electric fields (oriented along z) can be applied at a gate region by an external voltage V.

3.3.1 Electric-field effect: statics

The dynamic control of skyrmions, as will be explained later, can be understood in terms of the modification of their static properties. To this end, we discuss first the electric-field effect on the static properties of a skyrmion. In general, two separate regimes can be defined based on the stability of the skyrmion. In the first regime, the skyrmion remains stable with a smooth change in its diameter D_s, and the domain-wall width Δ_w, surrounding the skyrmion. This change occurs in order to minimize the micromagnetic energy corresponding to the electric-field induced modification of perpendicular anisotropy: the energy cost, due to deviation of magnetization from the easy axis in the wall region, increases with increasing K. In an attempt to reduce this energy cost, the domain wall area ($\sim\ 2\pi\ D_s\Delta_w$) is reduced resulting in decrease of both diameter of skyrmion and the wall-width. In the second regime, on the other hand, the skyrmion itself becomes unstable. This instability occurs close to the out-of-plane to in-plane transition of magnetization when the perpendicular anisotropy is lowered to a value, such that, the perpendicular anisotropy energy is overwhelmed by the dipole-dipole interaction, due to the out of plane component of the magnetization

To demonstrate the qualitative picture presented above in a specific numerical model, we perform micromagnetic simulations for a DDI-stabilized skyrmion(i.e. with DMI strength set to zero) with saturation magnetization, $M_s = 920$ emu/cm^3 and exchange stiffness $A = 1\ \mu$-erg/cm^3. In order to take electric-field-induced modification of perpendicular anisotropy into account, the strength of perpendicular anisotropy was varied in the range $K = [2, 5.5] \times 10^6$erg/cm^3. This range corresponds to films with $K = 4.25 \times 10^6$ erg/cm^3, in the absence of electric-field, and a maximum value of electric-field being $\sim$ 1MV/cm, for a coupling constant $\zeta = 20$erg/V·cm^2. These material parameters are typical for strain-based ferromagnet/dielectric

heterostructures such as CoPd(alloys)/PMN-PT, which are chosen as they exhibit one of the largest values of magneto-electric coupling (i.e. ζ) at room temperature [113]. In addition, a DDI skyrmion state has been found to be stable in finite-sized nanodisks of cobalt- and iron-based ferromagnets with similar material parameters [114, 115]. The simulated magnetic films are assumed to be two-dimensional with periodic boundary conditions in the film plane and a thickness of $t = 32$ nm. Additionally, an external magnetic field of strength $H_a/H_d = 0.3$ with $H_d = 4\pi M_s$, is applied along the $z$axis, which is needed to stabilize a DDI skyrmion for films of infinite extent.All micromagnetic simulations are performed using LLG Micromagnetic Simulator [116] with temperature set to zero.

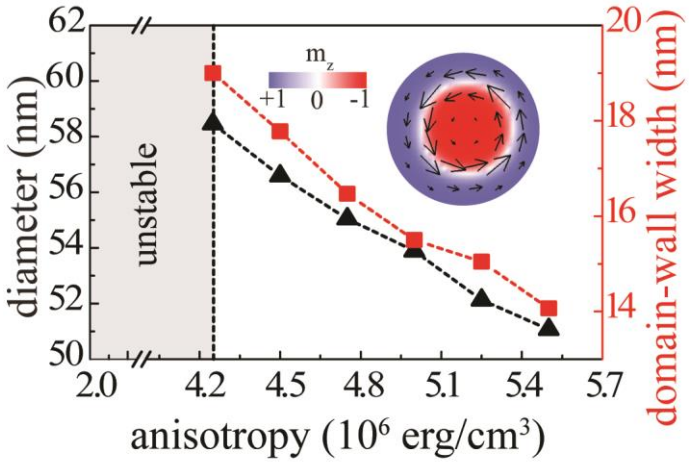

Fig. 3.7 Static properties of skyrmion as a function of perpendicular anisotropy K: broken vertical line marks approximate boundary between two regions. For $K > 4.25 \times 10^6$ erg/cm^3, skyrmion is stable, with its micromagnetic configuration for $K = 4.5 \times 10^6$ erg/cm^3 shown at top right corner. Here m_z denotes the out of plane component of the magnetization vector, while the in-plane components are shown with an arrow. The diameter and domain-wall width surrounding the skyrmion in this region is represented by triangle and square markers, respectively. For $K < 4.25 \times 10^6$ erg/cm^3 the skyrmion is unstable, instead a multi-domain/ in-plane state is favored.

To study the static properties of a skyrmion, the initial magnetization was set close to a film with a single skyrmion state, i.e. with a central region of sufficiently large diameter pointing along $-z$ and the rest of the film oriented along $+z$. This initial configuration was then allowed to relax to equilibrium for each value of perpendicular anisotropy. The result of such a procedure is summarized in Fig. 3.7. For anisotropy strength, $K < K_c = 4.25 \times 10^6$ erg/cm^3 the single skyrmion state is unstable, favoring a multi-domain (for relatively strong K, i.e between 3- and 4.25×10^6 erg/cm^3) or in-plane magnetization (for still weaker anisotropies, i.e. $K < 3 \times 10^6$ erg/cm^3). Such a behavior is typical for films, where the out-of-plane magnetization-induced dipole energy ($\sim M_s^2$) starts dominating the perpendicular anisotropy energy (K). This picture can be further confirmed by calculating the so-called quality factor $Q = K/2\pi M_s^2$ which has a value of $Q_c \sim 0.8$, i.e. close to one, at the critical anisotropy, K_c. On the other hand, for $K > K_c$ in the simulations, the resulting equilibrium configuration is that of a single skyrmion (shown in the inset of Fig. 3.7). As expected, in order to minimize the dipole-dipole interaction energy in the wall, the DDI skyrmion is ``Bloch-like" with skyrmion number $N = 1$. Moreover, increasing anisotropy results in decreasing diameter and wall-width surrounding the skyrmion, supporting the qualitative argument presented above.

3.3.2 Electric-field effect : dynamics

In this section we show how the modification of static properties of the skyrmion results in the electric-field control of current-induced skyrmion motion. Corresponding to the two regimes, defined for modification of static properties, there exist two qualitatively different regimes for the dynamic control.(i) When a uniform electric field with a magnitude below a

critical value is applied, such that the skyrmion remains stable, the change in D_s and Δ_w results in change in the magnitude and the direction of skyrmion motion. (ii) On the other hand, defining unstable regions for skyrmions by application of a non-uniform electric-field above the critical value, results in constraining skyrmion motion along desired paths (which we refer to as the ``guiding regime" below). To gain more insight into this connection between electric-field-induced static and dynamic control, we begin with an analytical model of current-induced skyrmion motion based on Thiele's collective coordinate approach.

Analytical model – In the collective coordinate approach, the relevant degrees of freedom, describing the equation of motion of a magnetic-texture, are given by the so- called soft modes [117]. The most relevant soft modes for a skyrmion in an infinite film are its rigid translations in the film plane. Consequently, the collective coordinates included for describing the motion of a skyrmion are (X, Y) which label the position of the skyrmion's center along the x and y axis, respectively. Within this approximation, LLG equation can be reduced to the following equation of motion[117]

$$\boldsymbol{G} \times \boldsymbol{v} - \Gamma \boldsymbol{v} + \boldsymbol{F^s} + \boldsymbol{F^u} = 0 \tag{3.2}$$

where $\boldsymbol{v} \equiv (\dot{X},\ \dot{Y})$ is the velocity vector, while $\boldsymbol{G} \equiv (0, 0, \mathcal{G})$ with $\mathcal{G} \equiv -\int \boldsymbol{m} \cdot \partial_x \boldsymbol{m} \times \partial_y \boldsymbol{m}$. Inclusion of other modes, such as wall fluctuations, results in deviations from the rigid motion approximation and endows Eq.3.2 with a ``mass term" [118], which is not the focus of the current study. The first term describes the ``Lorentz force" due to the skyrmion's non-trivial topology induced fictitious magnetic field [119]. Furthermore, the integrand in $\mathcal{G}$ is the local solid angle, making $\mathcal{G}$ independent of the exact magnetization texture and simply proportional to the skyrmion number, i.e. $\mathcal{G} = 4\pi N$. The second and third terms originate from the Gilbert damping and current-induced spin-orbit field term in LLG, respectively, with $\Gamma = \alpha \int \partial_x \boldsymbol{m} \cdot$

$\partial_x \boldsymbol{m}$ and $F_i^S = \gamma\eta J \int \partial_i \boldsymbol{m} \cdot \boldsymbol{m} \times \boldsymbol{y}$, where i labels the cartesian coordinates. Finally, the fourth term represents the force due to variation of the skyrmion's ``potential energy'' U, i.e. $\boldsymbol{F^u} = -\boldsymbol{\nabla} U$. The skyrmion's potential energy is, in turn, defined as $(X, Y) \equiv (\gamma t / M_s) \int \mathcal{F} + \frac{\zeta E m_z^2}{2}$, where the integral is performed for the magnetic configuration of a skyrmion with its center located at (X, Y). In contrast to $\mathcal{G}$; Γ, $\boldsymbol{F_i^s}$ and $\boldsymbol{F^u}$ depend on the exact functional form of the magnetization.

In general, the functional form of $\boldsymbol{F^u}$ will depend on the interaction of the skyrmion with its ``environment'' and will be discussed for the two regimes below, while analytical expressions are obtained for the dissipative and spin-orbit forces using Thiele's ansatz [120] for a skyrmion's magnetic configuration as $\Gamma = \alpha\pi^2 D_s / \Delta_w$ and $\boldsymbol{F^s} = (0, \gamma\eta J \pi^2 D_s / 2)$. Within this Thiele's ansatz, the integrand for Γ and $\boldsymbol{F^s}$ is assumed to be non-zero near the wall region, where the magnetization profile, parameterized by the polar(θ) and azimuthal(ϕ) angles as $\boldsymbol{m} = (\sin\theta\cos\phi, \sin\theta\sin\phi, \cos\theta)$, is given by $\cos\theta(r) = \tanh \pi r / \Delta_w$. Additionally, in order to compare to micromagnetics, the Bloch-like DDI skyrmion configuration with $N = 1$ is used, i.e. $\phi(\varphi) = \varphi + \pi/2$ with (r, φ) representing the two-dimensional film plane in cylindrical coordinates.

We begin by looking at the regime when a uniform electric-field, having a magnitude below the critical value required to make the skyrmion unstable, is applied to the infinite film. In this case, the skyrmion's potential energy is independent of its location and hence $\boldsymbol{F^u} = 0$. Consequently, solving Eq.3.2 for velocity, we obtain:

$$v = \frac{\gamma\eta J D_s}{8\sqrt{\left\{1 + \left(\frac{\alpha\pi D_s}{4\Delta_w}\right)^2\right\}}}; \psi = \tan^{-1}\frac{\alpha\pi D_s}{4\Delta_w} \tag{3.3}$$

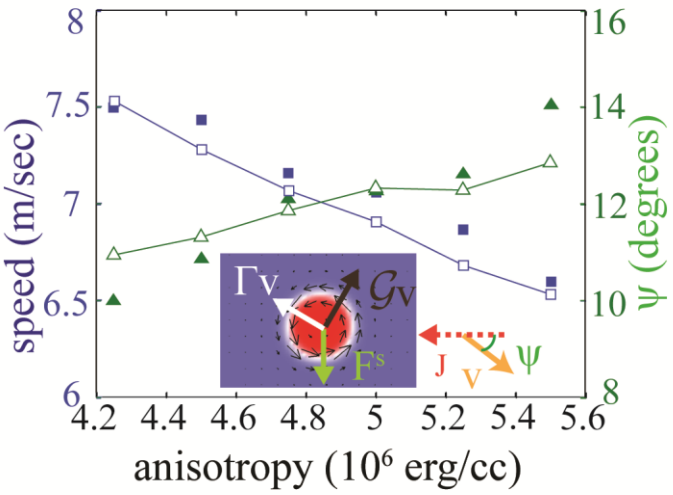

Fig. 3.8 Velocity modulation for uniform electric-field: the schematic in the bottom shows the steady-state of skyrmion moving with velocity $\boldsymbol{v}$and the corresponding forces acting on it. $\boldsymbol{F^s}$ represents current-induced spin-orbit force, while $\mathcal{G}\boldsymbol{v}$ and $\Gamma\boldsymbol{v}$ represent the Lorentz and damping force, respectively. Open square and triangle markers represent speed and the angle ψ (between current and $\boldsymbol{v}$ as shown in the schematic) as obtained from analytical model. The corresponding speed and angle from micromagnetic simulations are represented by the closed square and triangle markers.

where v is the skyrmion's speed and ψ is the angle between the skyrmion's motion and the current (see inset of Fig.3.8 for a schematic). This constitutes one of the main results of the analytical model, relating the skyrmion's static and dynamic properties. The electric-field control of skyrmion's motion in this regime is thus expected to enter via modification of D_s and Δ_w, as discussed in section III, and is shown in Fig.3.8 for the diameter and domain wall width extracted from static micromagnetic simulations. These analytical results are compared later against the velocities and angles extracted directly from dynamic micromagnetic simulations.

The dependence of U on electric-field suggests another qualitatively different route to control the skyrmion's dynamics via application of non-uniform electric-field and consequently

``engineering" desired forces $\boldsymbol{F^u}$. Interestingly in multiferroics, electric-field gradient-induced forces have been theoretically shown to induce Hall-like skyrmion motion [121]. Here, we propose the scenario where unstable regions [such as the one shown in the inset of Fig.3.9 (a)] can be defined for skyrmions, where magnetization deviates from the out-of-plane direction, due to the application of an electric field above the critical value. In this case, $\boldsymbol{F^u}$ becomes non-zero as the skyrmion approaches the boundary between the stable and unstable regions due to dipolar interaction, as explained next. The dipolar fields originating from the ``core" (i.e. the region inside the skyrmion's diameter) point in a direction opposite to the core's magnetization in the region outside the skyrmion's core. Deviation of magnetization from this dipolar field direction in the unstable region will thus result in a higher dipolar energy when compared with skyrmions interacting with the film in the absence of unstable regions [as illustrated in Fig.3.9 (b)].

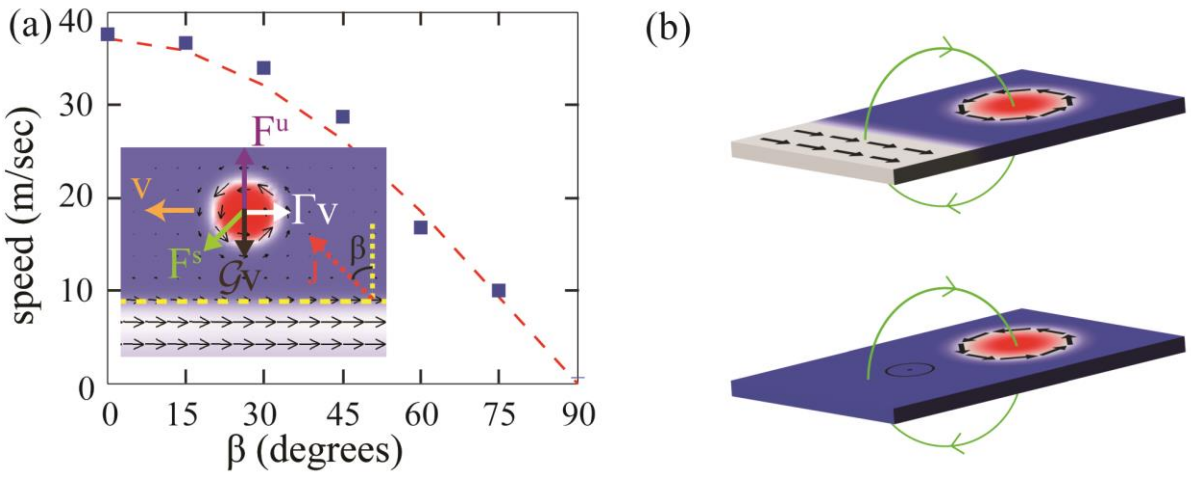

Fig. 3.9 Skyrmion guiding regime: (a) the bottom schematic shows the steady-state of a skyrmion moving along the boundary between stable and unstable regions (marked by a horizontal broken line) and corresponding forces. The angle between current and the normal to this boundary is represented by β. In addition to current-induced force, the damping force and the Lorentz force (as also shown in Fig. 3.8), there exist a dipolar force between the skyrmion and in-plane magnetization in the unstable region, denoted by $\boldsymbol{F^u}$. The skyrmion's speed along the boundary as a function of β as obtained from the

micromgnetic simulations is shown by the square marker. While the broken curve shows the result from the analytical model, i.e. Eq.3.4, for same current density. The origin of the dipolar force is illustrated in (b), which compares the interaction of a skyrmion with the environment in the presence (top schematic) and the absence (bottom schematic) of an unstable region. The red circular region represents the core of the skyrmion, with the magnetization inside and outside the skyrmion pointing along - and + z, respectively, while the lines emanating from the cylinder represent the dipolar field due to the core region. The magnetization in the unstable region for the top schematic points in the plane as shown by the arrows.

Consequently, as the skyrmion moves closer to the boundary between the stable and unstable regions, the dipolar energy increases and results in non-zero $\boldsymbol{F^u}$ preventing the skyrmion to enter the unstable region. Due to this additional $\boldsymbol{F^u}$ a new steady state is expected. This situation is very similar to the case of a skyrmion driven in nanowires, where in steady state the skyrmion is driven along the nanowire, with the dipolar forces from the boundary of the nanowire balancing the Lorentz force [122]. Thus generically it is expected that, for a range of drive currents, the skyrmion can be guided along the boundary between the stable and unstable regions, as depicted schematically in Fig.3.9. The advantage here, as compared to the nanowire case, is that this boundary is defined by application of the electric-field and hence can be constructed on the fly, providing a controllable method to ``rewire skyrmion current''. A general analytical expression for the velocity depends on the details of $\boldsymbol{F^u}$, however a simple expression can be derived for the case when the magnetization configuration in the unstable region has translational symmetry along the boundary [such as the one shown in the schematic of Fig.3.9 (a)]. This translational symmetry demands that $\boldsymbol{F^u}$ is oriented perpendicular to the boundary, whose magnitude is denoted by $\boldsymbol{F^u}$. Solving for a steady state with the skyrmion moving along the boundary, taking the angle between the current and the normal to the boundary to be β, and

balancing the forces along and transverse to the boundary [as depicted in the inset of Fig.3.9 (a)], we obtain for the guiding regime:

$$v = \gamma \eta J \frac{\Delta_w}{2\alpha} \cos\beta \, ; F_U = 4\pi v. \tag{3.4}$$

We can see from the above expression that by orienting the electric field gate boundary with respect to the current, i.e. changing β, the skyrmion's speed can be controlled dramatically. The position of the skyrmion with respect to the boundary, on the other hand, is given by the balance of Lorentz and dipolar forces, with the skyrmion pushed closer to the boundary for larger currents. We will now compare these analytical insights to the micromagnetic simulations and, in particular, prove the existence of the electric-field-controlled skyrmion guiding regime.

Micromagnetics– The micromagnetic simulations were performed for a DDI skyrmion with the same material parameters as used in the case for static simulations. In addition a current-induced spin-orbit torque, with $\eta = \hbar J \theta_s / 2eM_s t$ and $\theta_s = 0.2$ [31], was turned on as the driving force for all the simulations presented in this section. As noted in previous chapter a field-like SOT will not induce motion and hence is not included in these simulations. The dynamics were calculated by integrating LLG with a damping parameter $\alpha = 0.05$. In Fig.3.8 we first compare the results for a uniform electric-field with a magnitude below the critical field. These results are obtained for a single skyrmion moving in a film, with periodic boundary conditions along the film plane, and a fixed current density of $J = 10^8$ A/cm^2, while simultaneously varying the anisotropy throughout the film in the stable range. As can be seen, both the speed and the angle of the skyrmion with respect to the current direction are modulated by application of the electric-field. Moreover for the range of electric-field magnitudes studied here, the trend predicted by the analytical model fits the obtained v and ψ well, both qualitatively and quantitatively, substantiating the analytical picture presented above. For the material parameters used, the

electric-field modulation shown in this regime is, however, relatively weak. For a much stronger control of skyrmion dynamics, we next turn towards the other regime, i.e application of a non-uniform electric-field.

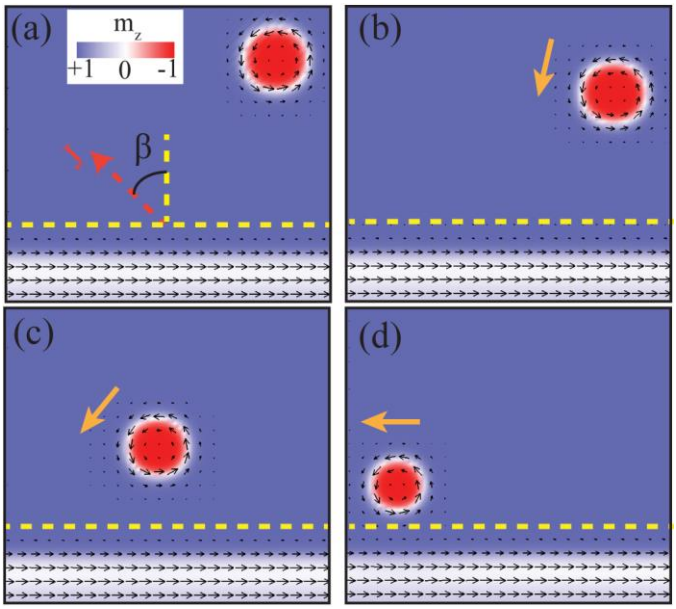

Fig. 3.10 Micromagnetic simulations showing the guiding by electric field: (a) Initial state showing a stable skyrmion with $K = 4.25 \times 10^6$erg/cm^3 in the region above the horizontal dashed line and in-plane magnetization below it, where $K = 2 \times 10^6$erg/cm^3. A current, with density J, and making an angle β with the normal to the boundary between stable and unstable regions, provides the driving force for the skyrmion. The inset shows the color code for out of plane magnetization, while the in-plane components are shown by arrows. The snapshot of simulation after (b) 5 ns, (c) 10 ns and (d) 20 ns, are shown with the arrows alongside the skyrmion representing the instantaneous direction of the skyrmion's motion.

To demonstrate the skyrmion guiding regime by defining unstable regions for skyrmions, micromagnetic simulations were performed with the value of $K = 4.25\ (2) \times 10^6$ erg/cm^3 in the stable (unstable) regions marked in Fig.3.10. The dynamics was then simulated for a skyrmion driven by current, with the initial state of a single skyrmion in the stable region. In Fig.3.10 we

show various snapshots of the results of these simulations. First note that, as was discussed in the section III, the magnetization in the unstable region goes to an in-plane state. In the initial stage of the simulation, i.e. when the skyrmion is relatively far from the the unstable region [Fig 3.10 (b)], the skyrmion behaves very similar to $\boldsymbol{F^u}$ case moving at an angle with respect to the current. However, as the skyrmion approaches the boundary between the stable and unstable region [Fig.3.10 (c)] a non-zero $\boldsymbol{F^u}$ deflects the skyrmion, preventing it from entering the unstable region. After $T = 40$ ns a new steady state is reached with the skyrmion moving along the boundary between the stable and unstable region [Fig.3.10 (d)] and hence proving the existence of the guiding regime. The robustness of this steady state was checked by varying the magnitude of drive current density. For this example, the skyrmion is still driven along the boundary for current density below $J = 5 \times 10^8$ A/cm^2. As the drive force increases, with increasing current density, the skyrmion is pushed closer to the boundary according to Eq. 3.4. However, above $J = 5 \times 10^8$ A/cm^2 the drive force overcomes $\boldsymbol{F^u}$, resulting in the skyrmion entering the unstable region where it is annihilated. Motivated by applications, we next discuss how this regime of skyrmion guiding could provide new opportunities for constructing possible spintronic devices.

3.3.3 Skyrmionics beyond racetracks

Nanosized skyrmions can be used as non-volatile information carriers in a spintronic device owing to their stability against thermal fluctuations. The information stored in the skyrmion can, in turn, be read both optically or electrically (by utilizing various magneto-resistance effects such as topological Hall effect [123], tunneling- [124] or giant- [125, 126] magnetoresistance). One such proposed example of a spintronic device is a race-track memory, where information stored in a magnetic texture is moved by current to a desired location where it

can be read or written [83]. With the discovery of current-induced skyrmion motion, skyrmions in a nanowire are considered as a promising alternate to ``conventional'' domains in a race-track memory as they show very weak pinning by external impurities requiring orders of magnitude lower critical depinning currents. The new possibility of controlling ``skyrmion current'' by the electrical-field presented here is thus expected to open up novel avenues of information processing with skyrmions. We demonstrate this by specifically showing via micromagnetic simulations that electric-field gates can be used to turn ``skyrmion currents'' off, i.e. providing a transistor-like operation, and deflect information carried by skyrmions in specific parts of the spintronic circuit, i.e. a multiplexer-like operation.

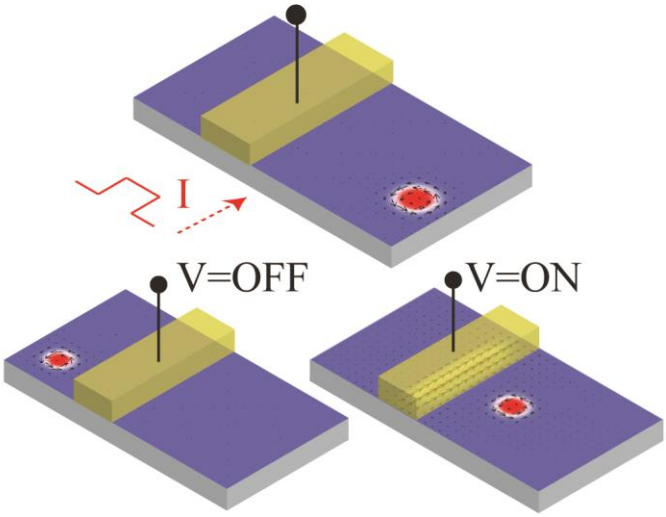

Fig. 3.11 Micromagnetic simulations showing the transistor-like function: top schematic shows the initial state with a skyrmion located on the right end of the nanowire, along with a current pulse of 10 ns passed through the heavy metal underlayer. An external electric-field can be applied locally via a voltage over a gate region indicated in the figure. The resulting location of the skyrmion at the end of the pulse when the gate is in OFF (bottom left) and ON (bottom right) state.

To demonstrate the transistor-like operation, a nanowire geometry is adopted in the simulations with width of the nanowires set at 200 nm. The anisotropy strength was $K = 4.25 \times 10^6$ erg/cm^3 throughout the simulations everywhere in the nanowire except in a region of width 50 nm defined as the gate. To simulate the effect of electric-field applied on the gated region, the anisotropy value was dropped to $K = 2 \times 10^6$ erg/cm^3 when the gate is in the ``ON'' state and kept at $K = 4.25 \times 10^6$ erg/cm$^3$ in the ``OFF'' state. The rest of the parameters are same as for the dynamical simulations presented above. The result of the application of a drive current pulse along the x axis of duration $t_p = 10$ ns is shown in Fig.3.11. When the gate is in the OFF state, the skyrmion is driven past the gate region along the nanowire (Fig.3.11 bottom left). On the other hand, when the same current pulse is applied in the presence of a gate voltage, the skyrmion is blocked by the gate (Fig.3.11 bottom right), due to the repulsive dipolar forces from the unstable gated region, thus exhibiting a transistor-like function. This situation is the special case of the guiding regime, i.e. Eq. 3.4, with $\beta = 90$.

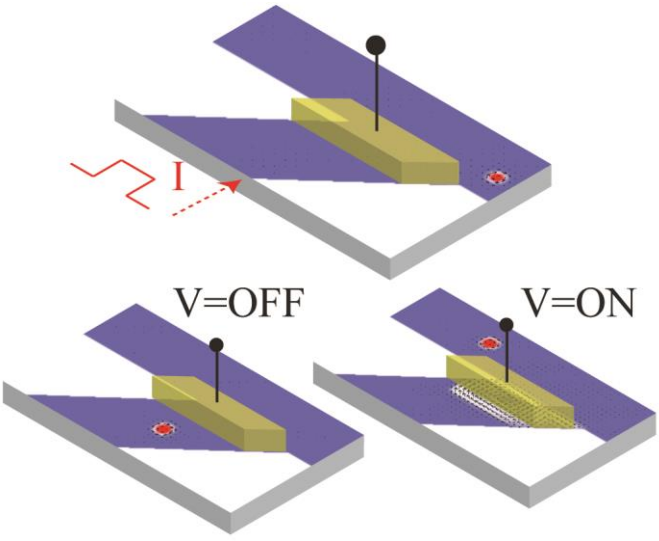

Fig. 3.12 Micromagnetic simulations showing the multiplexer-like function: top schematic shows the initial state for two magnetic nanowires coming together at the ``wing-shaped'' junction with a skyrmion located at the right end of the upper arm. A local external field can be applied at the shown gate region.

The result of the simulation at the end of a current pulse of 10ns passed through the heavy metal underlayer when the gate is OFF (bottom left schematic) and ON (bottom right schematic).

Next we simulate a ``wing-shaped'' nanowire junction, with two nanowires, each of width 200 nm, meeting at an angle representing two different arms of a spintronic circuit. A gate in this case is defined on one of the arms as shown in Fig.3.12 which also shows snapshots of the simulations. When the gate is OFF, a current pulse along the x axis in this case drives the skyrmion to the lower arm (Fig.3.12 bottom left). This motion is similar to a skyrmion moving at an angle with the current due to the Lorentz force, as seen for a skyrmion moving in an infinite film. However, when the gate voltage is turned on, the skyrmion driven by the same current pulse is deflected off the gate region into the upper arm (Fig.3.12 bottom right). Such structures can thus be used to rewire the skyrmion current into specific parts of the circuit.

3.4 Electric-field-induced domain-wall motion

We next turn towards motion of domain walls in the absence of current. This is achieved by using the voltage-induced SOT mentioned in section 1.5. To be specific, we analyze the equilibrium magnetic texture in a ferromagnet(F)\insulator (I)\F heterostructure with an elliptical cross section, i.e., an MTJ, where one of the ferromagnetic layers is pinned and the other free. See Fig. 3.13, where the role of voltage-induced SOT is to control the perpendicular anisotropy. For making connection with experiments we choose the microscopic mechanism for the voltage-induced SOT to be charge-based voltage control of magnetic anisotropy, i.e. VCMA. The presence of inhomogeneous stray fields from the pinned layer are essential to decrease the energy cost for out-of-plane magnetization and therefore encourage out-of-plane texture. By performing micromagnetic simulations, we find that a domain wall can be stabilized when the

perpendicular anisotropy, controlled by applied voltage, overcomes the out-of-plane demagnetization field. Informed by micromagnetic simulations, we study the VCMA-induced dynamics of this confined domain-wall by analytically modeling it as a quasi-one-dimensional magnetic wire. We find that VCMA induces precessional dynamics which can be exploited to switch the chirality of a Neel domain wall or force it to escape confinement.

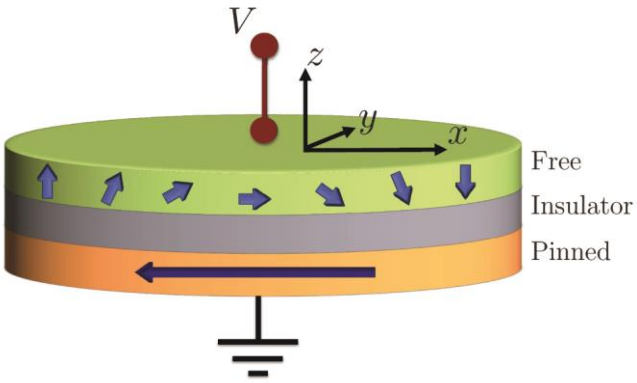

Fig. 3.13 The MTJ stack modeled by micromagnetic simulations: the free layer/insulator interface gives rise to an interfacial anisotropy $K^{\perp}$with vertical easy axis, controlled by a voltage, V. [47, 127] Pinned layer is kept fixed to point along $-x$.

3.4.1. Stabilizing a domain wall : Equilibrium Configurations

We consider a device geometry, shown in Fig. 3.13, which consists of an MTJ with a free ferromagnetic layer and a pinned ferromagnetic layer, pointing along $-x$, separated by an insulator having thicknesses t_F, t_P and t_I respectively. The cross section of the heterostructure is an ellipse where the semimajor axis is along the x direction and the semi-minor axis is along the y direction.

There are several magnetic configurations necessary to characterize the equilibrium states of our system as a function of perpendicular anisotropy. We schematically draw them in Fig. 3.14. The magnetization can be primarily in the plane of the ellipse along the x axis [see Fig.3.14 (a)], however the texture near the edges of the ellipse tend to follow the stray fields of the pinned layer and cant out of plane at angle θ_c. If the perpendicular anisotropy is large enough, the magnetization points entirely along the z axis [see Fig.3.14 (b)]. Fig.3.14 (c) and (d) depict Neel and Bloch domain walls, respectively, where the magnetic domains are along the z axis. A third domain wall, we call Bloch-like, in which the magnetization in the center of the domain wall is in-plane and aligned at an angle ϕ away from the x axis [see Fig.3.14 (e) and Fig.3.15 for a micromagnetic snapshot]. A Neel (Bloch) domain wall is a limiting example of a Bloch-like wall with $\phi = 0$ ($\phi = \pi/2$) and can smoothly interpolate between Neel and Bloch domain walls, as follows: When the domain-wall width (δ_W), schematically drawn in Fig.3.14 (f) and controlled by perpendicular anisotropy, is large the energy is minimized due to dipolar interactions when the central region points along the x axis. As δ_W is decreased, becoming narrower than the semiminor axis of the ellipse, the dipole energy in the Neel wall increases, forcing the magnetization at the center of the wall to orient away from the x axis to a finite value of ϕ.

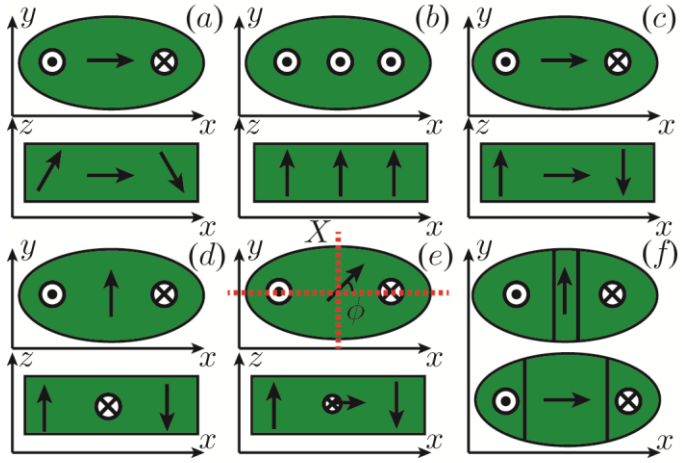

Fig. 3.14 Schematics of the relevant equilibrium configurations: (a) in-plane state with canted edges, (b) perpendicular state, (c) Neel domain wall, (d) Bloch domain wall, and (e) the intermediate domain wall where ϕ is the angle of magnetization at the center of the ellipse with respect to the x axis. The lower right hand frame (f) depicts the domain wall width, i.e. the central region delineated with vertical lines, much larger (top) and smaller (bottom) than the semiminor axis of the ellipse corresponding to a Neel and Bloch wall, respectively.

To develop a precise numerical model using micromagnetic simulations we take the magnetization saturation $M_s = 1200$ emu/cm^3 and exchange stiffness $A = 2\,\mu$-erg/cm. The perpendicular anisotropy is assumed to be of the form, $K^{\perp} = k^{\perp}/t_F$, with $k^{\perp} = 1.35$ erg/cm^2. These choices of material parameters are typical for a CoFeB/MgO interface [128]. For equilibrium simulations we control the perpendicular anisotropy by varying the free layer thickness. The major and minor axes are 300 nm and 100 nm respectively, while the thickness $t_I = 2$ nm and $t_P = 2.5$ nm. All the simulation results presented in this paper are obtained for zero temperature and are performed using the LLG Micromagnetic Simulator.[116] The phase diagram was constructed by initializing the free magnetic layer along x or along the z direction and allowing the system to relax to equilibrium (possibly resulting in two different configurations) for values of t_F ranging between 1.4 nm and 1.6 nm. Although increasing the thickness will change the demagnetization energy and influence of the stray fields, we do not expect it to significantly change our results. Energy of these equilibrium configurations are plotted as a function of perpendicular anisotropy in Fig. 3.15.

When the thickness is large $t_F > 1.5$ nm, the magnetization is primarily in-plane with canted edges and we identify the texture with the schematic in Fig.3.14 (a). As the perpendicular anisotropy increases, θ_c increases until $K^{\perp} \sim 8.7 \times 10^6$ erg/cm^3 when the out-of-plane

perpendicular anisotropy field overcomes the demagnetization field resulting in two stable magnetic configurations. The ground state is a Neel domain wall while we find an additional metastable state with magnetization perpendicular to the interface. The domain wall width decreases monotonically with increasing perpendicular anisotropy and at $K^{\perp} \sim 9.1 \times 10^6$erg/cm^3 the energy of the Neel domain-wall configuration surpasses that of the perpendicular state, which is now the most energetically favorable configuration. Although the perpendicular state remains the ground state, when $K^{\perp} \sim 9.2 \times 10^6$ erg/cm^3 the metastable Neel state undergoes a second-order phase transition to the Bloch-like wall with symmetry broken between $+\phi$ and $-\phi$. Further increasing the perpendicular anisotropy shrinks the domain wall, thus increasing ϕ. This control of ϕ with perpendicular anisotropy will be central in the discussion of dynamics in the following sections.

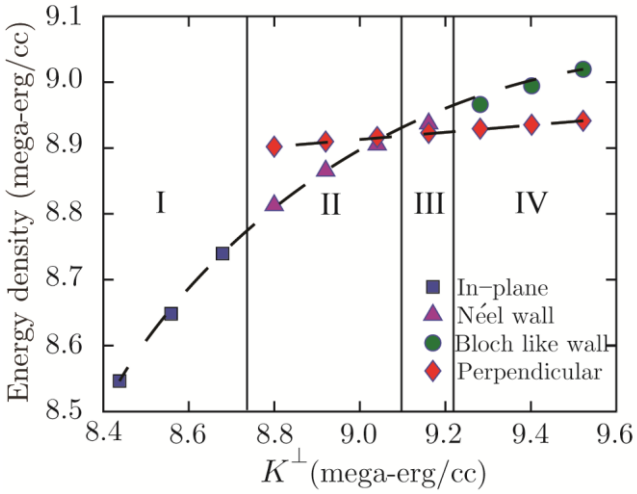

Fig. 3.15 The dependence of energy of equilibrium configurations on the interfacial perpendicular anisotropy: the vertical lines mark approximate boundaries between regions marked I-IV. Region I has only in-plane state with canted edges (schematically shown in Fig.3.14 a) as a stable state, region II has both Neel domain wall (schematically shown in Fig.3.14 c) and pependicular (monodomain) states, with domain walls having lower energy. In region III perpendicular states become lower in energy whereas in

region IV the Neel domain wall starts transforming into Bloch form (referred as Bloch-like wall with its micromagnetic configuration, corresponding to $K^{\perp} = 9.4$ mega-erg/cc, also shown in region IV).

3.4.2 Electric-field-induced domain wall dynamics : Simulations

In this section we consider the dynamic response of Neel wall configuration to voltage. First we focus on the micromagnetics governed by the Landau-Lifshitz-Gilbert (LLG) equation then, informed by these numerical results, we develop a phenomenological quasi-one-dimensional model, based on the Walker ansantz,[129] and find qualitative agreement between the two.

Micromagnetics−The dynamic simulations are performed using the LLG equation:

$$\partial_t \boldsymbol{m} = -\gamma \boldsymbol{m} \times \boldsymbol{H}_{eff} + \alpha \boldsymbol{m} \times \partial_t \boldsymbol{m} \tag{3.5}$$

where $\boldsymbol{m}$ is the unit vector pointing along the position-and time-dependent magnetization configuration of the free layer, α is the Gilbert damping and γ is the gyromagnetic ratio. The effective field, $\boldsymbol{H}_{eff}$, includes contributions from demagnetization field, exchange field and anisotropy field. In particular, now we have specialized to the case of only voltage induced torque, which enters due to electric-field dependent anisotropy field which is taken into account by making $K^{\perp} = (k^{\perp} + \zeta E)/t_F$, in line with recent experiments, where E is the electric field. The magneto-electric coupling coefficient is taken to be $\zeta = 10^{-8}$ erg/V $\cdot$ cm (close to the experimental [130] and theoretical value [131]), $\alpha = 0.01$ and $t_F = 1.5$ nm, while leaving all other parameters as in the previous section. Because we are primarily interested in low dissipation devices, we include the Gilbert damping but do not include other dissipative torques (e.g. spin transfer torque) allowed by symmetry.[44] We initialize the system so that the free layer is a Neel domain wall which, for these parameters, is the ground state of our system. To

induce motion we turn on an electric field abruptly to a non zero value and allow the domain wall to equilibrate to a new equilibrium state. We summarize the resultant motion in Fig.3.16.

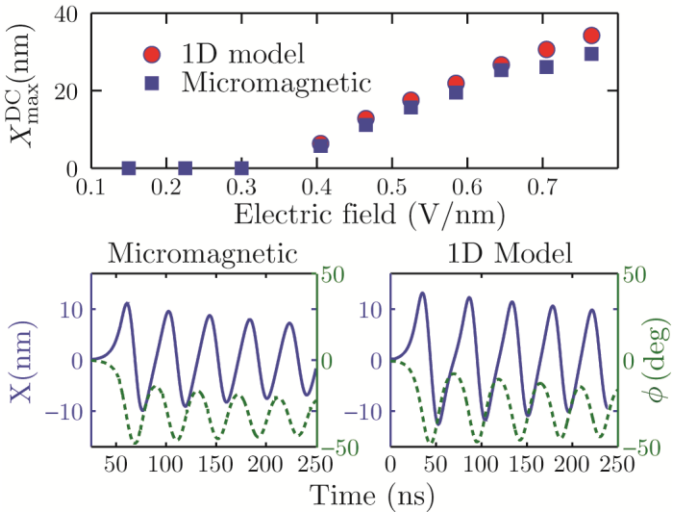

Fig. 3.16 Comparison between micromagnetics and 1D Model: (top panel) the maximum deviation of domain wall from the center, X_{max}^{DC}, obtained for electric field applied in a step-like fashion, (bottom panel) the dynamical approach to a Bloch-like wall from the initial configuration of a Neel wall, for same electric field magnitude in micromagnetic simulations (bottom left) and 1D Model (bottom right). Here solid lines depict the position (X) while the dashed lines show the angle (ϕ) of the domain wall.

The top panel of Fig.3.16 shows the maximum deviation of the domain wall, X_{max}^{DC}, from its equilibrium at the center of the ellipse as a function of the electric field magnitude. Below some critical value of electric field $E_c = 0.35$ V/nm, domain-wall motion is not induced, i.e. $X_{max}^{DC} = 0$. However when the magnitude of the electric field exceeds E_c, the domain wall position and angle oscillate, differing by a $\pi/2$ phase, as shown in the lower left hand panel of Fig. 3.16. Note that the time axis in the lower left hand panel begins at ~ 25 ns because below this time the dynamics are dominated by high frequency modes wherein the long-time dynamics of the domain-wall position, X, and tilt, ϕ are ill-defined. Importantly, E_c corresponds to a perpendicular anisotropy of $K^{\perp} \sim 9.3 \times 10^6$erg/cm^3 which is near the value of perpendicular

anisotropy where the domain wall transitions from Neel to Bloch-like. That is, below the critical field an electric field pulse will change the width of the Neel wall but not the type of domain wall. Above the critical field the domain wall undergoes a Neel-to-Bloch-like transition, which in turn results in domain-wall motion.

3.4.2 Electric-field-induced domain wall dynamics : Analytical model

The micromagnetic simulations imply that the long-time domain-wall dynamics are dominated by the *soft* modes which can be characterized by the generalized coordinates X and ϕ [see Fig.3.14 (e)] . To construct a phenomenological model of the domain-wall motion, we begin by writing down the free energy density consistent with the symmetries of our device geometry which is invariant under a mirror transformation in the yz plane as well as a mirror transformation in the xz plane followed by a π rotation around the z axis. Because $X \to -X$ under the former and $\sin\phi \to -\sin\phi$ under the latter, only even contributions of X and $\sin\phi$ are allowed:

$$\mathcal{F}(X,\phi) = \frac{C}{2}X^2 + K_1 \sin^2\phi + K_2 \sin^4\phi \tag{3.6}$$

In principle C, K_1, K_2 are dependent on the material parameters, i.e. A, M_s, $K^{\perp}$, and device dimensions, which can be obtained by the substitution of the domain-wall configuration in the micromagnetic free energy, including contributions from dipole, exchange and anisotropy energies. However, analytical expressions of this dependence cannot be obtained due to complicated form of dipolar interactions among the ``magnetic charges" residing at the top and bottom surface of the free layer, in the bulk of the domain wall, side surfaces (xz plane) of the finite sized free layer and the ends of the pinned layer. In the present case we thus obtain C, K_1 and K_2 by comparing the phenomenological results with micromagnetic simulations as will be

discussed later. Qualitatively, C, parameterizing the strength of a parabolic confining potential due to both inhomogeneous stray fields from the pinned layer and the finite size of the free layer, is expected to increase with increasing dipolar energy and hence with increasing M_s of both pinned and free layers. The relative strength of K_1 and K_2 determines the easy plane of domain wall magnetic texture. On the other hand, as explained in section II, the angle which the easy plane makes with the x axis increases with decreasing domain-wall width. Thus, K_1/K_2 decreases with decreasing domain-wall width which, in turn, decreases with increasing $K^{\perp}$ and decreasing A . Because a positive K_2 is required for a smooth transition of equilibrium states from Neel to Bloch wall, we henceforth take $K_2 > 0$ to match micromagnetic simulations. Higher order interactions and interactions of the form X^4 and $X^2 \sin^2 \phi$ are in principle allowed but not necessary to reproduce Neel and Bloch-like equilibrium configurations and are thus disregarded in the spirit of constructing a minimal model. To find the equation of motion for the generalized coordinates we use the one-dimensional Walker ansatz which states, for $\boldsymbol{m} = (\sin\theta\cos\varphi, \sin\theta\sin\varphi, \cos\theta)$ with θ and φ being polar and azimuthal angles, respectively, $\varphi = \phi$ and $\ln\tan\frac{\theta}{2} = \frac{x-X}{\delta_W}$. The equations of motion for our generalized coordinates are immediately determined following Ref. [117]:

$$\alpha\frac{\dot{X}}{\delta_W} + \dot{\phi} = \frac{\gamma H_c X}{\delta_W}$$

$$\frac{\dot{X}}{\delta_W} - \alpha\,\dot{\phi} = \gamma \sin 2\phi\,(H_1 + H_2 \sin^2\phi) \tag{3.7}$$

where we have defined $H_c \equiv \frac{\delta_W C}{M_s}$, $H_1 = \frac{K_1}{M_s}$ and $H_2 \equiv \frac{2K_2}{M_s}$. Because $H_C > 0$ and $H_2 > 0$, the stable fixed points of Eq. 3.7, (X_0, ϕ_0), depend on the value of H_1. For all stable solutions, the domain wall is at the center of the ellipse ($X_0 = 0$) while the domain-wall angle takes the values

0, $\sin^{-1}\pm\sqrt{\left\{\frac{|H_1|}{H_2}\right\}}$ and ± 1 for $H_1 > 0$, $0 > H_1 > -H_2$ and $-H_2 > H_1$ which correspond to a Neel, Bloch-like, and Bloch domain wall, respectively. The symmetry of the structure admits two solutions for any value of H_1.

In this model the phenomenological anisotropy fields, H_1 and H_2, and confining field H_C, are implicitly dependent on the perpendicular anisotropy $K^{\perp}$ and hence functions of the electric field. We therefore identify E_C with the value of electric field at which H_1 becomes negative. The observed domain-wall motion in micromagnetic simulations can then be explained as the following. If $E < E_C$, the equilibrium position is the same for both, when electric field is on and off, and thus the domain-wall tilt, as well as the position, is always in the equilibrium resulting in no motion. However, if $E > E_C$, ϕ_0 for the case when the electric field is on is different from when the electric field is off. The approach of ϕ to the new equilibrium in turn induces domain-wall motion according to Eq. 3.7.

In order to compare with micromagnetic simulations, we numerically integrate Eq. 3.7 first extracting values for the phenomenological parameters: H_C is found by comparing the displacement of the Neel domain-wall in the micromagnetics and the phenomenological model as a function of externally applied magnetic field along the z axis. H_1 and H_2 can then be obtained by matching ϕ_0 and the resonance frequency of the micromagnetics to the quasi-one-dimensional model. The dynamics of the phenomenological model are shown in the lower right hand panel of Fig.3.16 showing the time dependence of a domain wall, initially in a Neel configuration, after an electric field is turned on. We find the phenomenological model qualitatively matches the micromagnetic simulations. The presented minimal model is also able to provide a reasonable quantitative estimate of X_{max}^{DC}, which will be useful in the following section.

3.4.3 Outlook for applications: Electric-field-induced depinning and chirality switching

Next we study the dependence of the electric field pulse duration, T, on domain-wall motion. In contrast to the previous section, T is much shorter than the time for the domain-wall to reach equilibrium. By exploiting the VCMA-induced dynamics we find that a short pulsed electric field can switch the domain-wall chirality, i.e. $\phi_0 \rightarrow \phi_0 + \pi$, or induce a maximum displacement greater than the quasiequilibrium response, i.e. $X > X_{max}^{DC}$, for the same pulse magnitude. We comment on the application of the former to magnetic memory storage and the latter to racetrack memory.

We perform micromagnetic simulations using the geometry and material parameters given in the previous section. In Fig.3.18 (upper panel), we plot the maximum displacement of the domain wall, X_{max}^{P}, and find an oscillatory dependence as a function of pulse length. This is similar to pulsed switching of a monodomain by an applied magnetic field: [132] when an electric field pulse of magnitude $E > E_C$ is applied to our structure, the equilibrium domain-wall tilt changes from zero to a finite value which forces ϕ to oscillate around the new equilibrium. Because ϕ and X are conjugate variables, the maximum domain-wall displacement increases with increasing tilt angle. Thus, turning off electric field pulse when ϕ is large enhances X_{max}^{P}, relative to X_{max}^{DC}. Control of X_{max}^{P}, by the duration of current pulses has likewise been demonstrated for the case of spin-torque induced domain-wall motion.[133]

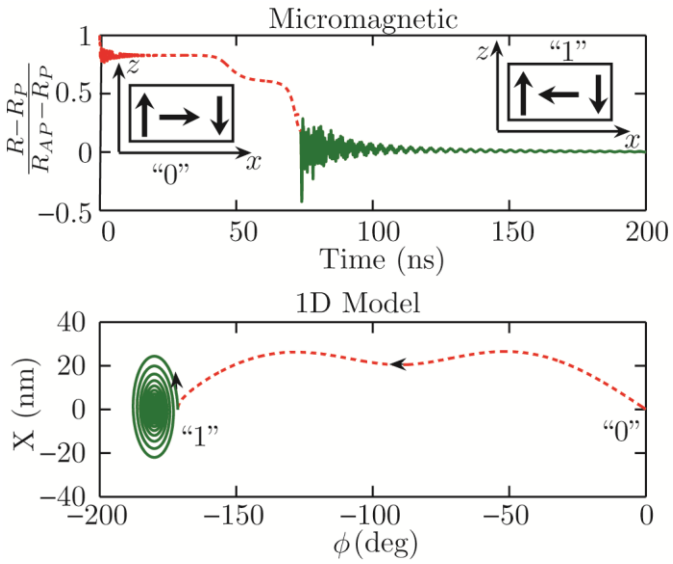

Fig.3.17 Chirality switching: (top panel) switching from state ``0", having resistance of $R_{AP}$, to state ``1", having a resistance of R_P (along with the respective domain-wall configurations in free layer depicted schematically), obtained via micromagnetic simulation for a pulsed electric field, $E = 0.65$ V/nm, of duration 75 ns, (bottom panel) switching trajectory in phase space from 1D model for the switching between state ``0" and state ``1" for the same electric field.

Chirality switching– This control of the maximum amplitude of ϕ can be used to reverse the chirality of the domain wall. See Fig.3.17 (upper panel). In micromagnetic simulations we apply an electric field of magnitude 0.65 V/nm to a Neel wall initialized at $\phi_0 = 0$ which forces a new equilibrium value at $\phi_0 \sim 50°$. As ϕ precesses around ϕ_0, it goes past 90° at which time the electric field is turned off and ϕ precesses towards the nearest Neel wall equilibrium, $\phi_0 = 180°$, switching the chirality. Likewise, we reproduce chirality switching in the phenomonological model [Fig.3.17 (lower panel)]. Using the chirality to encode bit information, ``0" when $\phi = 0$ and ``1" when $\phi = 180°$, tunnel magneto-resistance [124] with state ``0" (having resistance $R_{AP}$) and state ``1" (having resistance R_P) to read the chirality, and VCMA to switch it, domain-wall memory switch can be constructed. Although current-induced spin torque has also been used to

switch domain-wall chirality, [134] electric-field induced chirality switching provides a low-power attractive alternative. Moreover, the chirality affects the direction of the domain-wall velocity in the case of spin Hall driving. [34] Switching chirality via voltage can thus be used to reverse the direction of the spin-Hall driven motion (assuming one can overcome the barrier set by the Dzyaloshinskii-Moriya interaction [50, 51]).

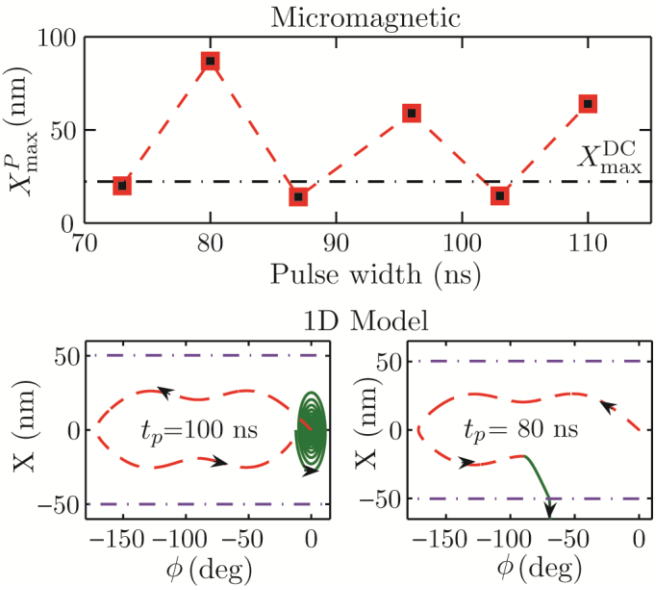

Fig. 3.18 Pulse width dependence of maximum domain wall deviation and depinning: (top panel) oscillatory enhancement of maximum deviation of domain wall from center, obtained from micromagnetics for electric field $E = 0.65$ V/nm. The dash-dotted horizontal line depicts the long-time maximum deviation for the same electric field as reference, (bottom panel) phase plot depicting the dependence of depinning on the pulse width as obtained within the 1D model for $E = 0.65$ V/nm. The extent of the parabolic potential $X_C = 50$ nm is marked by the horizontal dash-dot lines while the trajectory for which the pulse is on and off is marked by a dashed and a solid line, respectively. Depinning occurs when pulse is turned off for ϕ close to 90° (bottom right panel) whereas no depinning occurs when pulse is turned off for ϕ close to 0 (bottom left panel).

Depinning of domain walls—We depart slightly from the free energy used in the previous sections, Eq. 3.6, and consider, instead of a parabolic potential $CX^2/2$, a ``pinning parabolic potential" in which for $X > X_C$ the parabolic potential vanishes leaving all other parameters and the equation of motion, Eq. 3.7, unaltered. In this potential, if the displacement of the domain wall exceeds $X_C$ the domain wall is no longer localized to $X = 0$, i.e. ``depins." Experimentally, this can be realized by depositing a pinned layer with length of the order of X_C on top of a nanowire. Taking $X_C = 50$ nm and a pulse magnitude of $E = 0.65$ V/nm, we use the modified quasi-one-dimensional model to study the effect of pulse width on depinning. When $T = 100$ ns [Fig.3.18 (lower left panel)], the pulse turns off at $\phi\approx0$ and the domain wall returns to $X = 0$. A pulse width of $T = 80$ ns [Fig.3.18 (lower right panel)] ends at $\phi \sim \pi/2$ displacing the domain wall further than X_C, and depinning it. The ability to achieve depinning via pulsing electric field, in the absence of currents, could provide a major technological advantage in terms of power consumption in, for instance, racetrack memory. [83] Another key difference from the corresponding spin-torque induced domain-wall motion is the direction of electric-field induced domain-wall motion. In the present case, the domain wall can move either to $+x$ or to $-x$ as the new equilibrium exists at both $\pm\phi_0$. A small $\pm y$ directed magnetic field, sufficient to overcome the thermal fluctuations, can break the aforementioned symmetry and favor $\pm\phi_0$, thus controlling the direction of motion.

CHAPTER 4: SOT in magnetic insulators & magnon-induced soliton motion

4.1 Motivation

Perhaps the biggest advantage offered by spin-orbit torques is that it provides a mechanism to excite magnetization dynamics even in magnetic insulators. The rise in interest in the use of magnetic insulators is again due to the main driving point of the thesis: cutting down on energy dissipation channels. In magnetic insulators the information is carried by magnons, the quantum of collective magnetic excitations known as spin-waves. As opposed to charge excitations, magnons are free from Joule heating and are thus desirable means of transport of spin, also referred to as "pure spin current". In addition, a non-zero angular momentum carried by these Joule heating free magnons can be exchanged with magnetic solitons to induce their motion. Since magnetic insulators do not carry charge current it was not possible to apply spin transfer torque via the "traditional techniques". However, SOT can still be applied by interfacing magnetic-insulators with heavy metals and hence allowing for electrical control of magnetic insulators.

In this chapter we specifically demonstrate quantitatively non-zero SOT on a magnetic insulator: Yittrium Iron Garnet (YIG). YIG is the golden standard for magnon-based information processing, referred to as *magnonics*. In the process, we develop an optical scheme to quantify SOT and show its superiority over the transport methods, especially for magnetic insulators, used up until now to characterize SOTs. Moreover as a proof of principle of ability of magnons to transfer angular momentum, we also demonstrate motion of domain walls induced by thermally excited magnons.

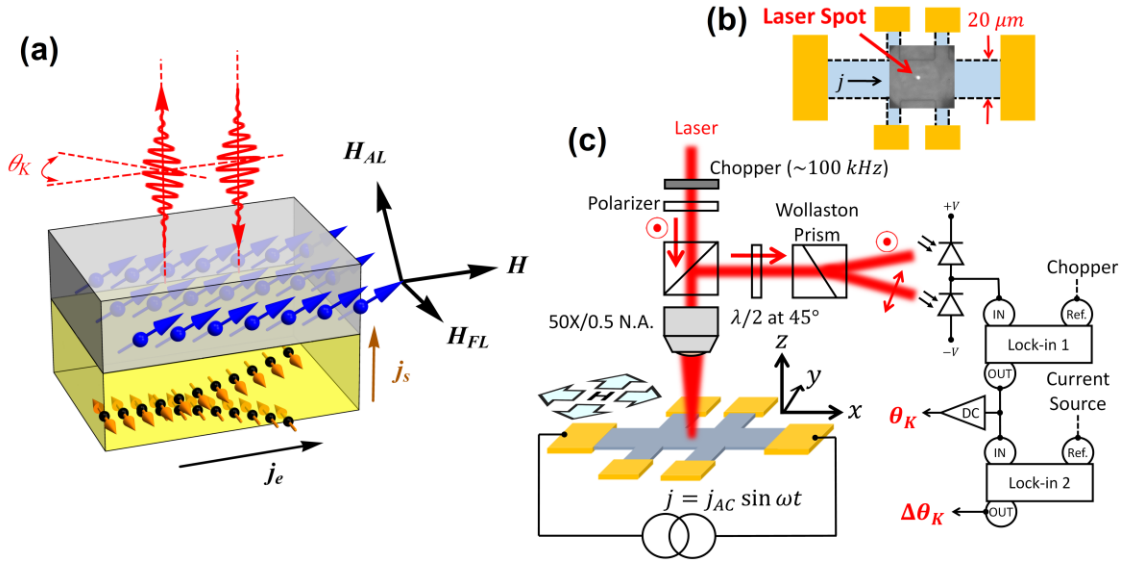

Fig 4.1 **Microscopy of spin-orbit fields. a**, Schematic of the current-induced magnetization dynamics by spin-orbit fields which is directly investigated for both metallic and insulating magnetic structures through the interaction of light with the magnetic order. **b**, The optical microscope image of the central region of the device in which the laser (white spot) is tightly focused at around the center of the device. The laser spot size is measured at $\sim 1\,\mu m$, which is much smaller than the dimensions of the device, implying the imaging capabilities of the optical probe. **c**, Schematic of the experimental setup depicting the in-plane current and magnetic field and the backscattering geometry of the probe laser beam.

4.2 Experimental setup and theoretical considerations

The contents of this and the next section are adapted from work submitted as: M Montazeri, P. Upadhyaya *, M.C. Onbasli, G. Yu, K.L. Wong, M. Lang, Y. Fan, X. Li, P.K. Amiri, R.N. Schwartz, C.A. Ross, K.L. Wang, "Magneto-optical investigation of spin-orbit torques in metallic and insulating magnetic heterostructures", submitted (Nature Nanotechnology)*

The interaction of light with magnetic order through the magneto-optical Kerr effect (MOKE) is known as a powerful magnetometry approach for both metallic and insulating

magnets. In particular, linear and nonlinear dynamics of the magnetization in virtually any direction, and with high spatial and time resolution, can be studied by employing various microscopy and sub-picosecond pump-probe techniques [135, 136]. Here we utilize this MOKE technique to quantitatively image magnetic oscillations induced by SOT.

The experimental setup is schematically shown in Fig. 4.1, and details can be found in Methods. In short, a linearly polarized laser beam is tightly focused at the center of a $20\,\mu m \times 130\,\mu m$ Hall bar device. The laser spot is measured at $\sim 1\,\mu m$, much smaller than the dimensions of the device (Fig. 4.1b). With an in-plane magnetic field, the magnetization at the laser spot is probed through the magneto-optical Kerr rotation (θ_K). The dynamics are induced through the SOT via an in-plane AC current $j = j_{\mathrm{AC}} \sin \omega t$ while, at the same time, the adiabatic current-induced change of the magnetization ($\Delta\theta_K$) at the laser spot is measured. In this backscattering geometry, the Kerr angle is linearly proportional to the out-of-plane component of the magnetization while the in-plane magnetization contributes through a second order term that is sensitive to the polarization of the incident light. Thus, θ_K is given by

$$\theta_K = f_\perp m_z + f_\parallel m_l m_t \tag{4.1}$$

where m_z is the OOP magnetization, m_l and m_t are longitudinal and transverse components of the IP magnetization with respect to the polarization of the light, and $f_\perp$ and $f_\parallel$ are first and second order magneto-optical coefficients that parameterize the strength of the coupling of the light to the OOP and the IP magnetization [137].

The current-induced magnetization dynamics can be described here by the Landau-Lifshitz-Gilbert (LLG) equation given by

$$\partial_t \boldsymbol{m} = -\gamma \boldsymbol{m} \times \boldsymbol{H}_{\mathrm{eff}} + \alpha\, \boldsymbol{m} \times \partial_t \boldsymbol{m} \tag{4.2}$$

where $\boldsymbol{m} = \boldsymbol{M}/M_s$ is the magnetization unit vector normalized to the spontaneous magnetization M_s, γ is the gyromagnetic constant and α parameterizes the damping. The effective field terms of relevance for this section can be written as $\boldsymbol{H}_{\text{eff}}$:

$$\boldsymbol{H}_{\text{eff}} = \boldsymbol{H}_a + H_k\, \boldsymbol{m}_z + \boldsymbol{H}_{Oe} + \boldsymbol{H}_{FL} + \boldsymbol{H}_{DL} \tag{4.3}$$

where $\boldsymbol{H}_a$ is the applied external magnetic field, H_k is the effective perpendicular anisotropy field, and $\boldsymbol{H}_{Oe}$ is the current-induced Oersted field. The last two terms are the spin-orbit fields, namely field-like (FL) and anti-damping-like (DL) components, with $\boldsymbol{H}_{FL} = \lambda_{FL}\, \boldsymbol{j} \times \boldsymbol{z}$ and $\boldsymbol{H}_{AL} = \lambda_{AL}(\boldsymbol{j} \times \boldsymbol{z}) \times \boldsymbol{m}$. Here, $\boldsymbol{j}$ is the current, $\boldsymbol{z}$ is the unit vector normal to the plane, and λ's quantify the strength of the spin-orbit fields. Since the non-resonance current-induced dynamics (with frequency of $\sim 10^3\ Hz$) are orders of magnitude slower than the magnetization precession frequency ($\sim 10^9\ Hz$), it is reasonable to assume that the magnetization adiabatically follows the effective field and thus the quasi-equilibrium condition is described by $\boldsymbol{m} \times \boldsymbol{H}_{\text{eff}} = 0$. Furthermore, we treat the SOT-induced non-resonance oscillation of the magnetization as a perturbation on the equilibrium condition defined by $j = 0$.

4.3 Spin-orbit fields in insulating YIG/Pt.

We use the optical probe to examine a prototype magnetic-insulator/heavy-metal structure in which the magnetization of the insulator (YIG) is modulated by an in-plane current through the heavy-metal (Pt). As shown in Fig. 4.2a, the structure consists of micrometer-size $4\ nm$-thick Pt Hall bar device on a mm-size $50\ nm$-thick YIG film grown on a GGG substrate. Furthermore, the YIG exhibits in-plane magnetization. The laser is focused on a $\sim 1\ \mu m$ spot at the center of the device while the magnetic field is kept in-plane. Due to the IP magnetization, the θ_K remains constant (zero) whereas, a pronounced current-induced $\Delta\theta_K$ is observed. An example of $\Delta\theta_K$ with the current density $j_{\text{AC}} = 5 \times 10^6\ A/cm^{-2}$ is shown in Fig. 4.2b wherein

both the current and the polarization of the incident light are parallel to the field. Two distinct regimes are identified: a sharp diverging-like feature at lower fields and a broader, slow decaying component most evident at the higher fields. With this geometry, the H_{AL} and H_{FL} point along the OOP and IP respectively (schematics in Fig. 4.2b). Thus, ignoring the in-plane anisotropy, for the current parallel to the magnetic field ($\phi_H \approx 0°$), the differential Kerr signal induced by an in-plane current reads

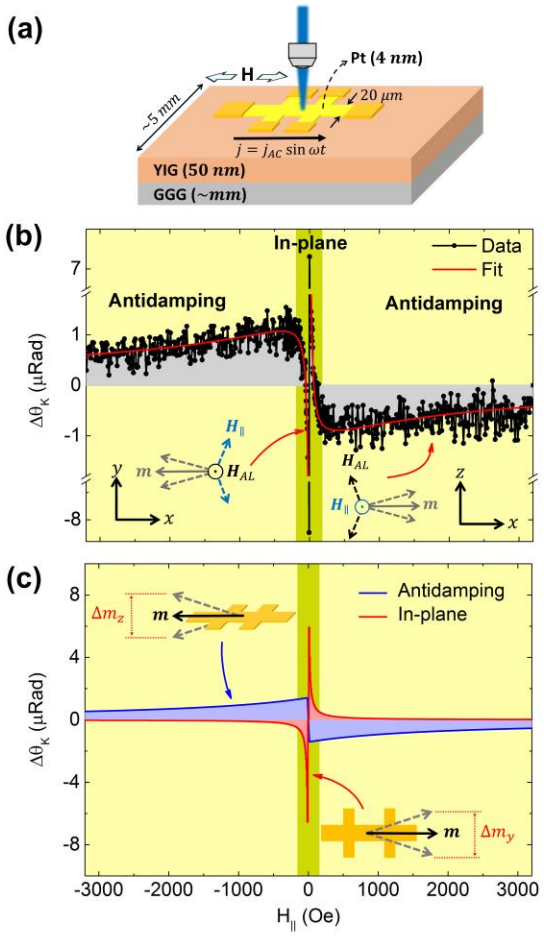

Fig. 4.2 **Current-induced differential Kerr of insulating YIG/Pt structure.** **a**, The structure of the device in which a micron-size 4 nm thick Pt device is fabricated on a mm-size 50 nm thick insulating YIG substrate. **b**, The differential Kerr angle of YIG/Pt with the magnetic field and the polarization of the incident light parallel to the current. With this geometry, the anti-

damping field drives the out-of-plane oscillation of the magnetization, whereas the field-like and Oersted fields drive the in-plane oscillation. The sharp diverging-like features at low fields corresponds to the in-plane oscillations partly driven by the field-like effective field, whereas the broader component, most evident at higher fields, corresponds to the out-of-plane oscillation driven by the anti-damping field. Equation (6) fits well to the experimental data (solid red line in **b**) wherein the individual contributions due to anti-damping and in-plane fields are shown in **c**.

$$\Delta\theta_K = f_\perp \Delta m_z + f_\parallel \Delta(m_l m_t) = -\frac{f_\perp H_{AL}}{H_a - H_k} + \frac{f_\parallel h_\parallel \cos 2\phi_p}{H_a} \tag{4.4}$$

where $H_k < 0$, ϕ_p is the angle between the current and the polarization of the incident light, and $h_\parallel = H_{FL} - H_{Oe}$. Both anti-damping-like and field-like effective fields contribute to the differential signal. Furthermore, the non-resonance OOP oscillation is induced by H_{AL} and competes against the H_k with a $1/(H_a - H_k)$ dependence, while the "free" IP oscillation is partly driven by H_{FL} and diverges at $H_a = 0$. Comparing with the experimental data in Fig. 4.2b, we find that the fast and the slow components are associated with the current-induced IP and OOP oscillations, respectively. The experimental data fits very well with the Eq. 4.4 (solid line in Fig. 4.2b) using the individual contributions of the IP and OOP oscillations that are demonstrated in Fig. 4.2c.

It is noted that the differential Kerr of the IP oscillation is sensitive to the polarization of the incident light, whereas the AL component is insensitive to the polarization as verified experimentally. This polarization dependence is unique to the optical probe and has no analogous counterpart in transport measurements. Figure 4.3 summarizes the polarization dependence of $\Delta\theta_K$ at a given current density. The diverging component, corresponding to the IP reorientation, shows a strong polarization dependence with maximum and minimum at

$\phi_p = 0°$ and 90°, respectively. On the other hand, the $\Delta\theta_K$ at higher fields, corresponding to the H_{AL}-induced OOP oscillations, shows no obvious polarization dependence as illustrated in Fig. 4.3c. The relative amplitude of the $h_{\parallel}$ vs polarization is extracted from a theoretical fit of Eq. 4.4 to the experimental data and is plotted in Fig. 4.3d. The data fits well with $\cos 2\phi_p$ (solid line in Fig. 4.3d) as predicted by Eq. 4.4. The small shift in vertical direction might be due to possible in-plane anisotropy or higher order effects that are ignored here. These observations strongly support the attribution of the OOP and IP oscillations to the slow and the fast components of $\Delta\theta_K$, respectively. Although in principle it is possible to extract the value of the H_{FL}, here however, we expect that the H_{Oe} dominates the IP oscillation.

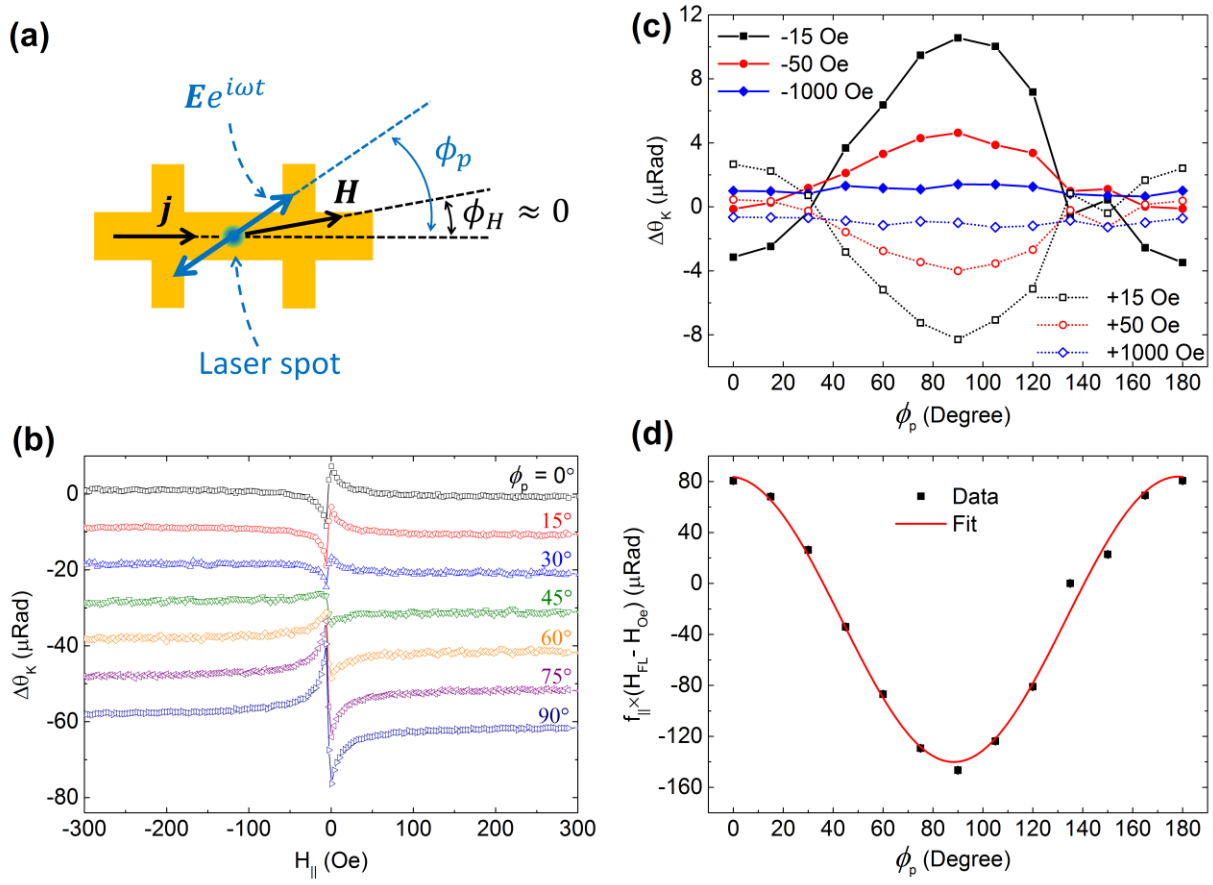

Fig. 4.3 **Polarization dependence of the differential Kerr of YIG/Pt.** **a**, Schematic of the measurements in which the magnetic field is parallel to the current and the polarization of the

perpendicularly incident light is varied with respect to the current. **b**, Comparison of the differetial Kerr of YIG/Pt at lower fields for different polarizations of the light. **c**, Polarization dependence of $\Delta\theta_K$ at various external fields. While the differential Kerr shows sinosudial dependence at low fields, it is insensitive to the polarization at higher fields. **d**, Amplitude of $\Delta\theta_K$ due to in-plane oscillations extracted from a theoretical fit of equation (6) to the experiment. The solid line in **d** is a theoretical fit to $\cos 2\phi_p$. The contribution of the in-plane oscillation to $\Delta\theta_K$ vanishes at $\phi_p \approx 40°$.

Furthermore, it is noted that the contribution of the IP oscillation is completely suppressed at $\phi_p \approx 40°$ and thus, at this polarization the signal is dominantly induced by the anti-damping field.

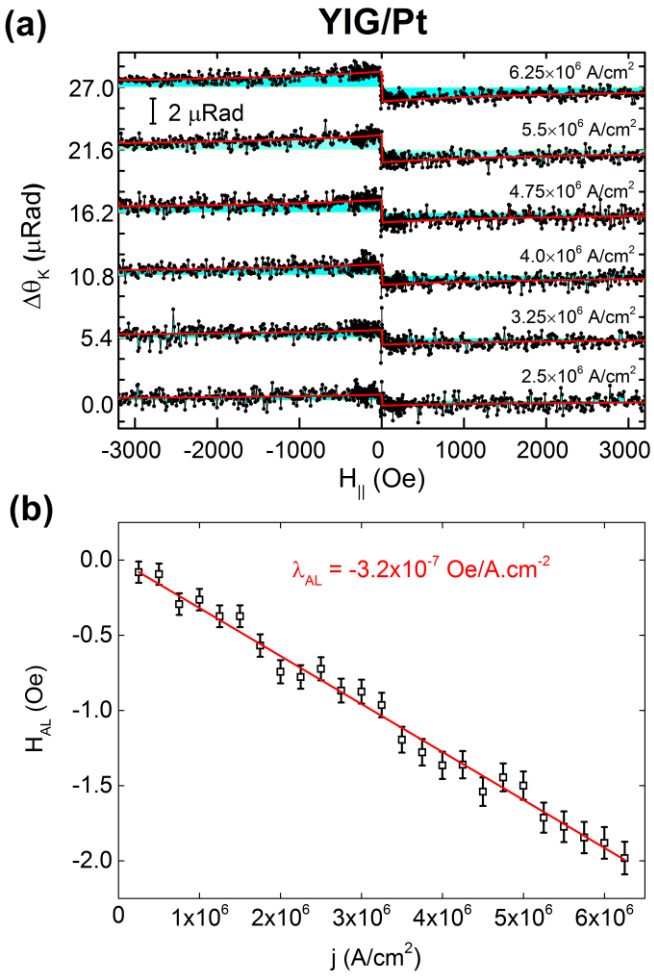

Fig. 4.4 Optically measured anti-damping field of YIG/Pt. **a**, Current dependence of the differential Kerr with the polarization of the light set to $\phi_p \approx 40°$ to diminish the contribution of the in-plane oscillation. Solid red lines in **a** are theoretical fits of the anti-damping-induced component of equation (6) to the experimental data. **b**, The measured anti-damping field in YIG/Pt vs the current density through the Pt device. The solid red line in **b** is a linear fit to the data that yields the anti-damping coefficient $\lambda_{AL} = -(3.19 \pm 0.04) \times 10^{-7}\, Oe/A.cm^{-2}$.

We report the current dependence of $\Delta\theta_K$ of YIG/Pt in Fig. 4.4a with the polarization set to $\phi_p = 40°$ in which evidently there is only contribution of anti-damping field. The data fits very well to the first term of Eq. 4.4 providing a quantitative measure of the H_{AL}. The coefficient $f_\perp$ in Eq. 4.4 is independently measured. Figure 4.4b shows the measured anti-damping effective field at various current densities demonstrating a linear dependence. The AL coefficient is extracted by a linear fit to the data resulting in $\lambda_{AL} = -(3.19 \pm 0.04) \times 10^{-7}\, Oe/A.cm^{-2}$.

4.4 Thermal magnons-induced domain wall motion

The contents of this section are adapted from work originally published in Ref.[138]

In this section, we show the appeal of magnons for doing active work by showing motion of solitons in absence of any currents. A temperature gradient can drive DW motion in a magnetic insulator by a mechanism that is analogous to the conduction electron spin transfer torque (STT) mechanism in transition metal ferromagnets [139, 140]. Here, the thermally excited magnonic current J_m [141] transfers its spin angular momentum to the local magnetization inside the DW, which in turn yields a spin-wave/magnonic STT [142-144]. Specifically, a total change of spin angular momentum of $2\hbar$ would be imparted by the propagating spin wave to the DW in the absence of angular momentum losses [142-146]. In addition, through observing the

amplification of spin wave excitation in the presence of a temperature gradient, Padrón-Hernández *et al*., have suggested that the local magnetization can be affected by magnonic STT [147].

One key feature of DW motion induced by magnonic STT is that, as a result of the continuity of spin angular momentum, the DW travels in a direction opposite to the direction of spin wave propagation, *viz*., from the cold region towards the hot region in the presence of a temperature gradient, as predicted theoretically [142-146, 148]. The underlying adiabatic approximation is validated as the wavelength of the thermally excited magnons (λ ~ 6 nm) is smaller than the DW width [($\sigma_{dw} \sim \sqrt{A / K_U}$ ~ 60 nm): λ/σ_{dw} ~ 0.1] [88]. It is also conceivable that thermal phonon fluxes could contribute to DW motion in magnetic insulators, particularly due to a force exerted on a DW that is thinner than the thermal phonon wavelength. In the opposite, adiabatic limit, magnonic STT is a more natural scenario. This is confirmed by our data, in which DWs move opposite to the direction of the applied heat current.

DW dynamics in YIG in the presence of small temperature gradients can be described by substituting the Walker ansatz into the Landau-Lifshitz-Gilbert (LLG) equation: $M_S(1-\alpha \boldsymbol{m})\times\partial_t \boldsymbol{m} + \gamma \boldsymbol{m}\times \boldsymbol{H}_{\text{eff}} = \gamma\hbar J_{\text{m}}(\partial_x \boldsymbol{m} - \beta \boldsymbol{m}\times\partial_x \boldsymbol{m})$ with the effective magnetic field $\boldsymbol{H}_{eff} = (K_U m_z)\hat{z} - (2\pi {M_S}^2 m_x)\hat{x} + A\nabla^2 \boldsymbol{m}$ [142], and magnetization vector is given by $\boldsymbol{m} = (m_x, m_y, m_z)$. Below the Walker breakdown, the DW velocity ($v = \partial_t X$) which is quite similar to the current driven DW motion [149], can be written as:

$$v = -\frac{\beta}{\alpha}\frac{\gamma\hbar}{M_S} J_{\text{m}} \tag{4.4}$$

where M_S is the saturation magnetization, γ is the gyromagnetic ratio, α and β are dimensionless damping constants. For a given temperature gradient (∇T), the amplitude of J_{m} can be estimated

as $J_m = -\frac{k_B \nabla T}{6\pi^2 \lambda \hbar \alpha} F_0$, where $F_0 \approx 1$ is a coefficient arising in the kinetic theory of magnonic STT [142, 148, 150]. At room temperature (RT), the resultant DW velocity in YIG films in the presence of a temperature gradient ∇T = 20 K/mm can thus be estimated to be v = 1300 μm/s (assuming $\alpha = \beta$) [142]. It should be noted that magnon-magnon/phonon/disorder scatterings would lower the estimated value of the DW velocity.

4.4.1 Experimental setup and results

The magnetic systems exploited here are 2 μm thick yttrium iron garnet (YIG) films with a perpendicular anisotropy of composition $(YSmLuCa)_3(FeGe)_5O_{12}$, grown by a liquid phase epitaxial technique on (111) orientated $Gd_3Ga_5O_{12}$ (GGG) garnet substrates [88]. DW dynamics

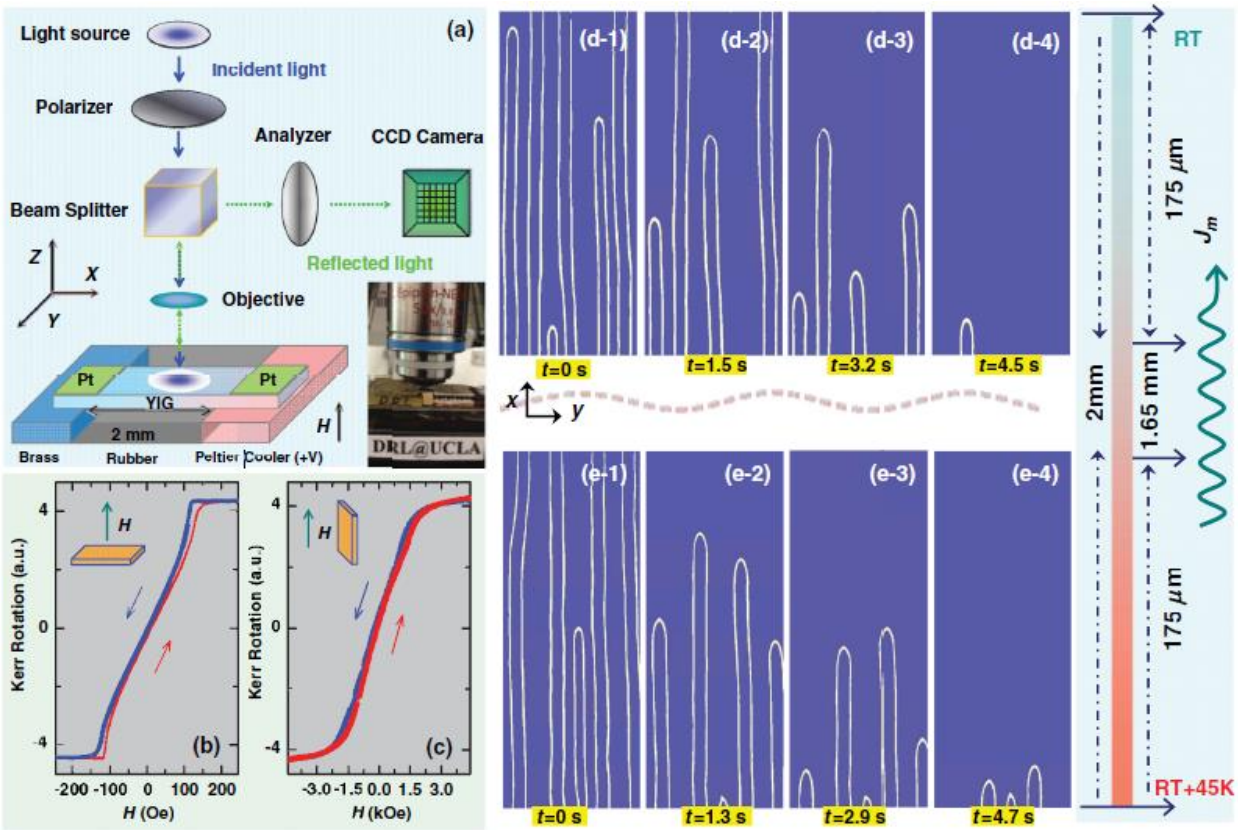

Fig. 4.5 Experimental demonstration of DW motion driven by a temperature gradient. (a) The schematic illustration of polar MOKE microscope for DW imaging. (b) and (c) are *M vs. H* hysteresis loops measured using a MOKE magnetometer for polar and longitudinal orientations, respectively. (d) Snapshots of the position of the DW as a function of time in the cold region, and hot region (e), respectively. These sequential images demonstrate that the direction of motion of the DWs in both cold and hot regions is the same, *viz.*, from the cold region (RT) to the hot region (RT + 45 K), with an average DW velocity of $\bar{v} = 200 \pm 5$ μm/s.

were monitored using a polar MOKE microscope [99]. The damping factor was estimated to be α = 0.0075. Temperature gradients (∇T) were generated by a Peltier Cooler, as confirmed by real time monitoring the resistances of Pt stripes (width 10 μm, thickness 15 nm). Good thermal contact was made by using silver epoxy. It is noted that the temperature gradient produced by the on-chip Joule heating *should* be avoided in YIG films: (a) a magnetic field gradient [88]; (b) spin waves excited by spin Hall effect (Pt, Ta in particular) [35]; and (c) an inhomogeneous temperature gradient [151-153].

Figure 4.5(a) is a schematic illustration of the experimental setup. Temperature gradients of various magnitudes (∇T) were applied along the *x* direction, as depicted. During the experiments, the sample is initially saturated (H = 300 Oe) and then decreased to a constant magnetic field (H = 60 Oe) that is applied normal to the sample plane in the *z* direction. The above geometry is kept throughout this report. Figures 4.5(b) and 4.5(c) display MOKE hysteresis loops measured with the magnetic field perpendicular/parallel to the plane of the YIG film, which confirm that the easy axis is normal to the film plane [88]. These data reveal that the out-of-plane saturation field is approximately 135 Oe, whereas the in-plane saturation field is ~1750 Oe; the saturation

magnetization M_S = 84 emu/cm^3, and K_U = 610 J/m^3 was determined using a SQUID magnetometer.

A polar MOKE microscope was subsequently used to experimentally visualize the time resolved DW motion driven by the temperature gradient. Sequential images are shown for the cold side in Figure 4.5(d1-e4) and for the hot side in Figure 4.5(e1-e4) in the presence of a temperature gradient (∇T = 22.5 K/mm). It is evident from the above sequential images, the DW moves from the cold region towards the hot region. During this process, the DW shape remains approximately unchanged, at least within the measurement limit of the MOKE microscope. These experimental results share qualitative features with the corresponding theoretical prediction based on magnonic STT [142-144, 146]; *i.e.*, the DW moves from the cold side towards the hotter region in the presence of a temperature gradient.

An important characteristic of the temperature gradient induced DW motion in the present system is that it behaves discontinuously. Specifically, an avalanche like behavior is observed that differs from its counterpart produced by either a magnetic field, or an electric current [139, 140], as well as the corresponding simulation [144]. The occurrence of this avalanche-like behavior is typically related to the Barkhausen effect [99], *viz*., a sudden change in the size or orientation of magnetic domains. The physical origin of the above jerky behavior lies in the competition between the driving force generated by the magnonic STT and the pinning force produced by defects/impurities (not considered in the corresponding simulation results [144]). It is noted that the average DW velocity $\bar{v}$ is defined in terms of the total DW displacement ($X(t)$) divided by the time when a Barkhausen avalanche occurs (t_1) (*i.e.*, in the time frame where the motion occurs), rather than the total imaging period (t) in order to minimize the scattering in $\bar{v}$ values due to the Barkhausen effect.

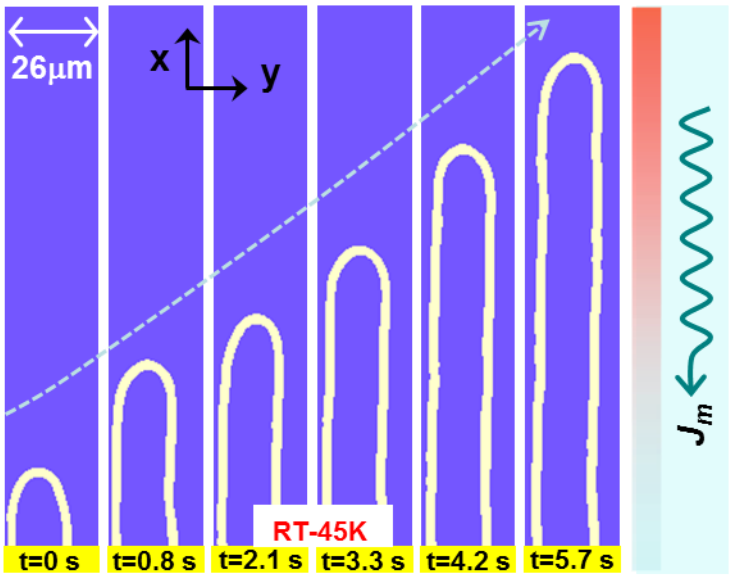

Fig. 4.6 Dependence of DW motion on the negative direction of the temperature gradient. Applying the same positive bias magnetic field (H = +60 Oe) as used in Figure 1, with the temperature gradient orientation reversed (*viz.*, ∇T = -22.5 K/mm); again, the direction of motion is preserved, *i.e.*, from the cold end towards the hot end, with an average DW velocity of $\bar{v}$ = 185 ± 5 μm/s.

For the temperature gradient ∇T = 20 K/mm, one realizes that the measured DW velocity $\bar{v} \approx 200 \pm 5$ μm/s is about the same order compared to the simulation based on the Landau-Lifshitz-Bloch (LLB) equation of motion ($\bar{v}$ = 1000 μm/s) (which is however, made based on the damping constant of 1) [144], and the theoretical estimation given previously ($\bar{v}$ = 1300 μm/s). The above differences between simulation and experiment may originate from: (a) magnon-magnon/phonon/disorder momentum scatterings [142, 148]; and (b) the precise value of the ratio β/α is, furthermore, unknown at present for YIG [142].

When a negative temperature gradient (∇T = -22.5 K/mm) was applied by reversing the input voltage into Peltier cooler, the direction of magnon propagation is opposite as compared to the positive ∇T. The direction of DW motion however, remains the same, *viz.*, from the cold

region towards the hot region, in accordance with theory [142-144], as evident in Figure 4.6. By analyzing the DW dynamics depicted in Figure 4.6, one finds that the average DW velocity ($\bar{v}$ = 185 ± 5 μm/s) is smaller than the DW motion displayed in Figures 4.5. The above observation is consistent with the current driven DW motion in transition metal ferromagnets in which the direction of motion is opposite to the injected current.

4.4.2 "Nonlocal geometry": a consistency check for magnon-driven motion

As the thermally excited magnon propagates from the hot side towards the cold side, it also penetrates into the cold side which is set at a constant temperature (namely, on top of thermal bath, which is marked region III in Figure 3 (a)) [148, 154]. As a result, in the region of constant temperature that is however, away from the region with the temperature gradient (region

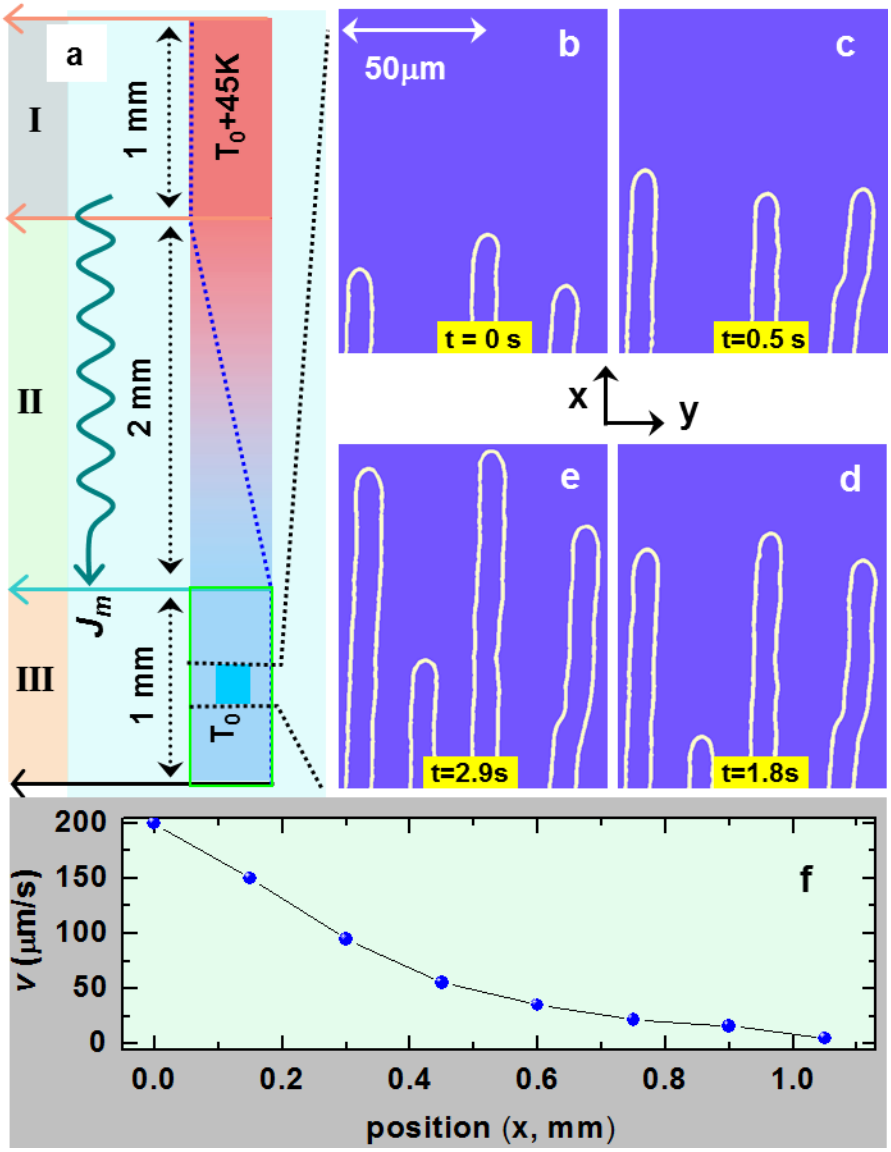

Fig. 4.7 Observation of DW motion due to the decay of magnonic current that is associated with the decay of magnonic temperature bias. Figure (a) is the schematic demonstration of DW motion due to the decaying magnonic current in region (III) of constant temperature (RT), which is away from region (II) with a temperature gradient. In such a region (~ 0.4 mm away from a temperature gradient ∇T = 22.5 K/mm), the decaying magnonic current induced DW motion is evident with an estimated velocity of $\bar{v}$ = 90 ± 5 μm/s, shown in Figures 3 (b)-(e). The evolution of the DW velocity as a function of distance to the temperature gradient is shown in Figure 3 (f) which can be empirically fitted by using $v = v_0 e^{-L/L_0}$ with characteristic length $L_0 \approx 1$ mm.

II) as depicted in Figure 4.7 (a), the thermodynamic force due to the DW energy gradient is consequently minimized [155-158], and the predominant force can be attributed to the magnonic STT that results from the (decaying) magnonic current which is associated with the decay of magnonic temperature, as suggested in other SSE experiments [154]. In such a region (~ 0.4 mm away from a temperature gradient ∇T = 22.5 K/mm, as III in Figure 4.7 (a)), the decaying magnonic current-induced DW motion is clearly revealed with an average velocity of $\bar{v}$ = 90 ± 5 μm/s, shown in Figures 4.7 (b)-(e). Note that the constant temperature (RT ± 0.2 K) in this region (III) is confirmed by measuring the resistance of several Pt stripes. Figure 4.7 (f) clearly shows that the measured DW velocity as a function of the distance to region II with a temperature gradient (∇T = 22.5 K/mm) exhibits an exponential decay function. Such a decay function can be empirically fitted by using $v = v_0 e^{-L/L_0}$, where v_0 is the DW velocity in the region with a temperature gradient (marked as II in Figure 4.7 (a)), v is the DW velocity at varying distance (L) on top of the heat bath; the characteristic length $L_0 \approx 1$ mm is related to the thermalization length of magnons in YIG, which is a collective quantity determined by magnon-phonon and magnon-magnon interaction [148]. The same length scale perhaps governs spatial characteristics of the SSE [141]. This experiment also serves as evidence in support of the difference between magnon and phonon thermal distributions, as suggested by other SSE experiments [154]. The above experiment, which is *non-local* in nature, can also be extended to metallic systems to avoid the inhomogeneous temperature gradient created by Joule heating [151].

The evolution of DW motion under different temperature gradients was also studied. Selected images are shown in Figure 4.8. Clearly, the average DW velocity monotonically

decreases as the applied temperature gradient decreases (in the temperature gradient range 5 K/mm < ∇T < 22.5 K/mm). This behavior is expected as a consequence of the decreasing

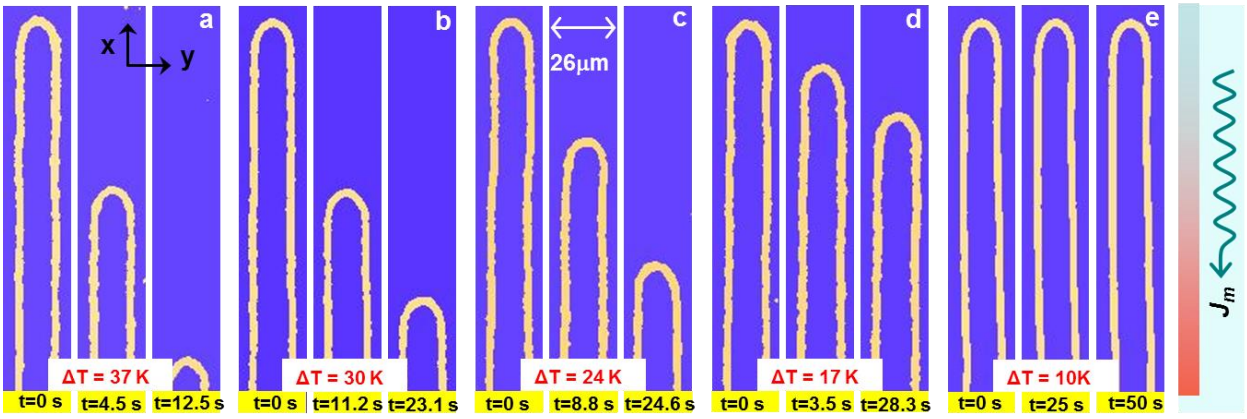

Fig. 4.8 Evolutionary demonstration of DW motion under varying temperature gradients. In the presence of the progressively decreasing temperature gradient, one clearly sees that the overall DW displacements decrease and the time intervals spent in traveling increase. These images together yield the decreasing average DW velocity. Here the corresponding temperature gradients for each measurement are (a) ∇T = 18.5 K/mm, (b) ∇T = 15 K/mm, (c) ∇T = 11.5 K/mm, (d) ∇T = 8.5 K/mm, and (e) ∇T = 5 K/mm.

(average) magnitudes of the excited magnons accompanied with the decreasing applied temperature gradient, which in turn limits the absorbed spin angular momentum. Dependence of $\bar{\nu}$ *v.s.* ∇T is displayed in Figure 4.9, which exhibits two distinct features. For 5 K/mm < ∇T < 22.5 K/mm, an approximately linear function is evident; while for ∇T < 5 K/mm, $\bar{\nu}$ = 0. Specifically, these results reveal the existence of a threshold temperature gradient ∇T_{th} (> 5 K/mm), *i.e.*, a minimal temperature gradient required to overcome the energy barrier, which is again, consistent with the threshold electrical current density J_{th} in current driven DW motion. It should be noted that the threshold temperature gradient ∇T_{th} is approximately the same over the 2 mm spacing between the cold and hot sides.

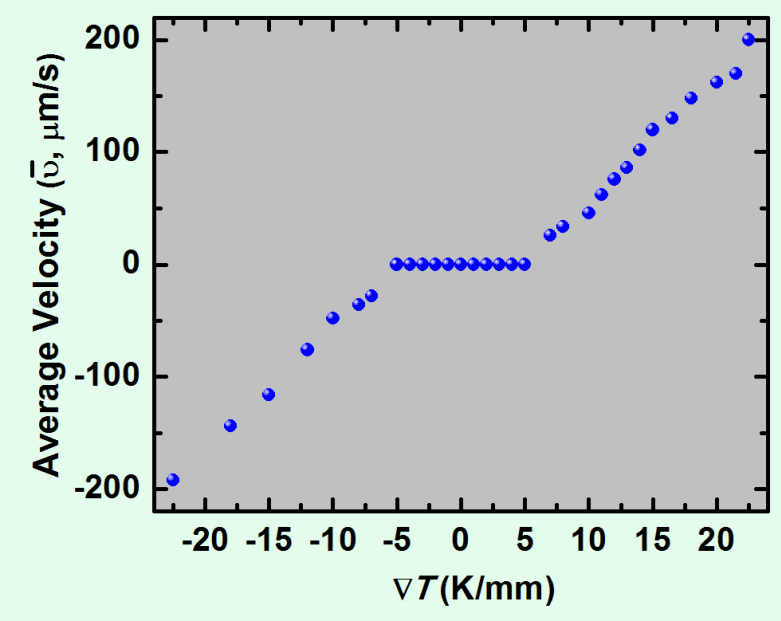

Fig. 4.9 Average DW velocity dependence on temperature gradient. The plot of $\bar{v}$ *versus* ∇T manifests the existence of a threshold temperature gradient $\nabla T_{\text{th}} \approx 5$ K/mm. Here, $\bar{v}$ is an approximately linear function in the temperature range of 5 K/mm < ∇T < 22.5 K/mm, -22.5 K/mm < ∇T < -5 K/mm, and in the range of -5 K/mm < ∇T < 5 K/mm, $\bar{v}$ is zero.

4.5 Comparison between metallic and insulating system

First focusing on SOTs, the magnitude of λ_{AL} in YIG/Pt is nearly one order of magnitude smaller than that of metallic Ta/CoFeB/MgO. One should note however that the $50\ nm$-thick YIG is substantially thicker than the $1.1\ nm$-thick CoFeB. Furthermore, the spin transmission efficiency at the YIG/Pt interface could be as small as 0.15 [159]. A more quantitative comparison can be obtained by noting $\lambda_{AL} \sim T\theta_{SH}/(t_{FM}M_S)$ in which θ_{SH} is the spin-Hall angle of the heavy-metal, t_{FM} is the thickness of the magnetic layer and T characterizes the effective spin transmission at the interface of heavy-metal and magnetic layer. Using the experimentally measured λ_{AL} for YIG/Pt and Ta/CoFeB/MgO, we obtain $(T\theta_{SH})_{\text{YIG/Pt}}/(T\theta_{SH})_{\text{Ta/CoFeB}} = 0.78$.

Here we used M_s of 75 emu/cm^3 and 700 emu/cm^3 for YIG and CoFeB, respectively. Overall, our data suggest that the anti-damping field in YIG/Pt is relatively large and can potentially be used to switch the magnetization by reducing the thickness and perhaps the lateral dimensions of the YIG, as well as using materials with higher spin-Hall angle such as topological insulators. YIG has attracted much attention for investigating the physics of magnonics and related phenomena due to its small damping. Due to the experimental limitations inherent in the transport techniques, very limited efforts have been reported to quantify the strength of the SOTs in YIG-based structures and spintronic devices. Very few examples found in the literature have employed indirect approaches either through the inverse spin-Hall effect or resonance of a dipole-coupled magnetic AFM tip for devices with a very specific geometry and thickness [159]. The optical measurements; however, overcome these problems and provide a direct measure of the spin-orbit fields in virtually any magnetic insulator structures.

Similarly, for solitons, a comparison with electrical current driven DW motion in metallic systems can also be made. The threshold current density in metallic systems J_e is typically 10^{11-12} A/m^2, with the accompanied Joule heating resulting in a local temperature increase up to 600-1000 K [139, 160]. In contrast, simply by applying a small temperature gradient (∇T > 5 K/mm) to a magnetic insulator YIG, we have observed pronounced DW motion.

CHAPTER 5: Conclusions

There have been several occasions in the past where the end of CMOS era has been predicted and successfully averted by the innovations in engineering community, pushing the limits of miniaturization to unimaginable extent. However, now it has become clear that this race towards shrinking devices is having adverse effects in terms of power wastage. In Chapter 1 this problem was highlighted as the prime reason for a shift towards need for low power consumption devices. At the extremely small scale of devices, the major reason for wastage in charge-based devices turns out to be "leakage-induced" standby power. This is where the magnet-based devices provide a significant advantage. As was known from quite a long time from storage industry, magnets can keep "information" intact for several tens of years, thus requiring zero standby power.

Motivated by this fact the field of spintronics was introduced in Chapter 1, where the main goal is to control magnets electrically so that computational devices can be constructed out of magnets. Several mechanisms for electrical control of magnets were introduced which can broadly be classified into two categories: (a) devices which electrically control the critical temperature at which a material remains magnetic, example being charge carrier controlled magnetism in doped magnetic semiconductors and interface charge controlled Curie temperature in metallic thin ferromagnets. (b) Exchanging angular momentum with magnets and hence applying so called spin-torque on the magnets. Focusing on the mechanism (b) in this thesis, we then introduced more "traditional" and popular way of exchanging angular momentum with the help of another magnet (known as polarizer). This method has already resulted in commercial products in the form of spin transfer torque magnetic random access memory. However, the

major issue remaining for this method to be a viable electrical scheme for low power consumption devices is to reduce the dynamic power consumption, which currently is at least two orders of magnitude larger than CMOS based devices. The reason for such large dynamic power is the limitation on the amount of spin-current being generated for a given charge current by polarizers as characterized by the so-called polarization factor $P < 1$.

A new method of exchanging angular momentum, utilizing orbital degrees of freedom, was then introduced which is free from the limitation of $P < 1$. Spin-orbit interaction provides the necessary tool that translates between orbital (controlled electrically) and spin (causing magnetism) degrees of freedom, whose origin lies in relativistic effects pronounced in heavy elements. This new way of exchanging angular momentum results in electrical torques on magnets referred to as the spin-orbit torques (SOT), opening a new field on electrical manipulation of magnets known as *spin-orbitronics*. Based purely on a symmetry-based phenomenology, all possible effect of spin-orbit interaction was then discussed in material systems with engineered asymmetries and high spin-orbit interaction.

Prior to this thesis a reduction in currents by an order of magnitude for switching of magnets, when compared to spin transfer from polarizers, was already demonstrated showing the promise of spin-orbitronics for low power consumption devices. In Chapter 2 we further reduced this power consumption by discovery of novel spin-orbit torques in systems with lateral asymmetry and topological-insulator-based magnets. First focusing on switching of perpendicular magnets (which are desirable for higher density) we proposed and experimentally demonstrated a strategy for removing unwanted external magnetic fields required to switch the magnets by SOT. Next, taking advantage of the fact that the efficiency of SOT is not limited by $P < 1$, and high spin-orbit coupling in topological insulators we demonstrated 1000 times more

efficient SOT in magnetically doped topological insulators. Future challenge in this topic is to observe such large SOT at room temperature which can possibly be achieved by marrying topological insulators with magnetic insulators.

In Chapter 3, we showed that SOT can, apart from providing a means to switch magnets, also create and manipulate magnetic particles known as solitons. These magnetic solitons carry useful information which can be read electrically and has been proposed to construct memory and logic devices. The efficiency of SOT thus provides a low energy route to electrically control them. To this end, we demonstrate experimentally for the first time creation and motion of a magnetic particle known as skyrmion bubble at room temperature, which has been proposed to have the advantage of being able to depin from impurities at very low current densities. Such structures are encouraged by combination of two spin-orbitronic effects: SOT from inhomogeneous current and Dzyaloshinskii-Moriya interaction (DMI) favoring monochiral structures. The inhomogeneous SOT helps in expansion of stripe domain which breaks into bubbles much like how bubbles can be blown out of thin soap films, while, DMI stabilizes a single chirality providing a topological barrier to overcome and thus resulting in the interesting properties observed for skyrmions. Next, we went beyond current control by combining it with the more energy efficient voltage-induced SOT to show functionalities beyond simple motion of skyrmions, demonstrating theoretically skyrmion-based transistor and multiplexers. The role of voltage-induced SOT was to guide the skyrmion along desired trajectories by designing electrical energy landscape for the bubbles. Future directions in this field would involve a thorough study of scaling and method to increase the strength of DMI to make smaller bubbles for higher density and lower pinning.

Finally we devised a theoretical scheme to completely remove the need for current, and hence the associated wastage of energy via Joule heating, by showing a scheme for motion of domain wall soliton purely by voltage-induced SOT. This was achieved by change in the internal structure of domain wall caused by voltage-induced SOT which resulted in a non-zero force and hence motion of a domain wall soliton. Along the same line of removing the use of charge currents in transportation of spin-information, via the so-called “pure” spin currents carried by spin-waves (or its elementary excitation called magnons), the advantage of SOT was highlighted in Chapter 4 for inducing magnetization dynamics even in magnetic insulators. We devised an optical scheme providing a direct quantitative measurement of SOT in YIG/Pt bilayer structures. It was found that the SOT in insulators is as efficient as in metallic system. Moreover, as a proof of principle for all magnonic devices, we demonstrated that this pure spin current carried by magnons can result in non-zero torque pushing magnetic soliton in the absence of charge currents.

References

[1] "The Noble prize in Physics 1956," http://www.nobelprize.org/nobel_prizes/physics/laureates/1956/

[2] "The Integrated Circuit." http://www.nobelprize.org/educational/physics/integrated_circuit/

[3] R. H. Dennard, F. H. Gaensslen, V. L. Rideout, E. Bassous, and A. R. LeBlanc, "Design of ion-implanted MOSFET's with very small physical dimensions," *IEEE Journal of Solid-State Circuits,* vol. 9, pp. 256-268, 1974.

[4] G. E. Moore, "Cramming More Components Onto Integrated Circuits," *Proceedings of the IEEE,* vol. 86, pp. 82-85, 1998.

[5] J. Alzate, "Voltage-Controlled Magnetic Dynamics in Nanosclae Magnetic Tunnel Junctions," PhD Thesis, University of California Los Angeles, 2014.

[6] I. Žutić, J. Fabian, and S. Das Sarma, "Spintronics: Fundamentals and applications," *Reviews of Modern Physics,* vol. 76, pp. 323-410, 2004.

[7] K. J. Kuhn, "Considerations for Ultimate CMOS Scaling," *IEEE Transactions on Electron Devices,* vol. 59, pp. 1813-1828, 2012.

[8] H. Zhao, A. Lyle, Y. Zhang, P. K. Amiri, G. Rowlands, Z. Zeng, *et al.*, "Low writing energy and sub nanosecond spin torque transfer switching of in-plane magnetic tunnel junction for spin torque transfer random access memory," *Journal of Applied Physics,* vol. 109, p. 07C720, 2011.

[9] P. Khalili Amiri, Z. M. Zeng, J. Langer, H. Zhao, G. Rowlands, Y. J. Chen, *et al.*, "Switching current reduction using perpendicular anisotropy in CoFeB–MgO magnetic tunnel junctions," *Applied Physics Letters,* vol. 98, p. 112507, 2011.

[10] T. Dietl, "A ten-year perspective on dilute magnetic semiconductors and oxides," *Nat Mater,* vol. 9, pp. 965-74, Dec 2010.

[11] H. Ohno, D. Chiba, F. Matsukura, T. Omiya, E. Abe, T. Dietl, *et al.*, "Electric-field control of ferromagnetism," *Nature,* vol. 408, pp. 944-6, Dec 21-28 2000.

[12] T. Dietl, "Zener Model Description of Ferromagnetism in Zinc-Blende Magnetic Semiconductors," *Science,* vol. 287, pp. 1019-1022, 2000.

[13] T. Jungwirth, J. Sinova, J. Mašek, J. Kučera, and A. H. MacDonald, "Theory of ferromagnetic (III,Mn)V semiconductors," *Reviews of Modern Physics,* vol. 78, pp. 809-864, 2006.

[14] T. Dietl and H. Ohno, "Dilute ferromagnetic semiconductors: Physics and spintronic structures," *Reviews of Modern Physics,* vol. 86, pp. 187-251, 2014.

[15] I. V. Ovchinnikov and K. L. Wang, "Theory of electric-field-controlled surface ferromagnetic transition in metals," *Physical Review B,* vol. 79, 2009.

[16] D. Chiba, S. Fukami, K. Shimamura, N. Ishiwata, K. Kobayashi, and T. Ono, "Electrical control of the ferromagnetic phase transition in cobalt at room temperature," *Nat Mater,* vol. 10, pp. 853-6, Nov 2011.

[17] L. Berger, "Emission of spin waves by a magnetic multilayer traversed by a current," *Physical Review B,* vol. 54, pp. 9353-9358, 1996.

[18] J. C. Slonczewski, "Current-driven excitation of magnetic multilayers," *Journal of Magnetism and Magnetic Materials,* vol. 159, pp. L1-L7, 1996.

[19] E. B. Myers, "Current-Induced Switching of Domains in Magnetic Multilayer Devices," *Science,* vol. 285, pp. 867-870, 1999.

[20] M. Tsoi, A. G. M. Jansen, J. Bass, W. C. Chiang, M. Seck, V. Tsoi, *et al.*, "Excitation of a Magnetic Multilayer by an Electric Current," *Physical Review Letters,* vol. 80, pp. 4281-4284, 1998.

[21] J. A. Katine, F. J. Albert, R. A. Buhrman, E. B. Myers, and D. C. Ralph, "Current-Driven Magnetization Reversal and Spin-Wave Excitations in Co/Cu/Co Pillars," *Physical Review Letters,* vol. 84, pp. 3149-3152, 2000.

[22] D. C. Ralph and M. D. Stiles, "Spin transfer torques," *Journal of Magnetism and Magnetic Materials,* vol. 320, pp. 1190-1216, 2008.

[23] J. Nogués and I. K. Schuller, "Exchange bias," *Journal of Magnetism and Magnetic Materials,* vol. 192, pp. 203-232, 1999.

[24] *Spintronics-based computing*: Springer International Publishing, 2015.

[25] R. Winkler. (2003). *Spin-orbit coupling effects in two-dimensional electron and hole systems*. Available: http://rave.ohiolink.edu/ebooks/ebc/10864040

[26] J. E. Hirsch, "Spin Hall Effect," *Physical Review Letters,* vol. 83, pp. 1834-1837, 1999.

[27] A. Hoffmann, "Spin Hall Effects in Metals," *IEEE Transactions on Magnetics,* vol. 49, pp. 5172-5193, 2013.

[28] Y. Fan, P. Upadhyaya, X. Kou, M. Lang, S. Takei, Z. Wang, *et al.*, "Magnetization switching through giant spin-orbit torque in a magnetically doped topological insulator heterostructure," *Nat Mater,* vol. 13, pp. 699-704, Jul 2014.

[29] A. Chernyshov, M. Overby, X. Liu, J. K. Furdyna, Y. Lyanda-Geller, and L. P. Rokhinson, "Evidence for reversible control of magnetization in a ferromagnetic material by means of spin–orbit magnetic field," *Nature Physics,* vol. 5, pp. 656-659, 2009.

[30] I. M. Miron, G. Gaudin, S. Auffret, B. Rodmacq, A. Schuhl, S. Pizzini, *et al.*, "Current-driven spin torque induced by the Rashba effect in a ferromagnetic metal layer," *Nat Mater,* vol. 9, pp. 230-4, Mar 2010.

[31] L. Liu, C. F. Pai, Y. Li, H. W. Tseng, D. C. Ralph, and R. A. Buhrman, "Spin-torque switching with the giant spin Hall effect of tantalum," *Science,* vol. 336, pp. 555-8, May 4 2012.

[32] A. R. Mellnik, J. S. Lee, A. Richardella, J. L. Grab, P. J. Mintun, M. H. Fischer, *et al.*, "Spin-transfer torque generated by a topological insulator," *Nature,* vol. 511, pp. 449-51, Jul 24 2014.

[33] P. P. Haazen, E. Mure, J. H. Franken, R. Lavrijsen, H. J. Swagten, and B. Koopmans, "Domain wall depinning governed by the spin Hall effect," *Nat Mater,* vol. 12, pp. 299-303, Apr 2013.

[34] K. S. Ryu, L. Thomas, S. H. Yang, and S. Parkin, "Chiral spin torque at magnetic domain walls," *Nat Nanotechnol,* vol. 8, pp. 527-33, Jul 2013.

[35] Y. Kajiwara, K. Harii, S. Takahashi, J. Ohe, K. Uchida, M. Mizuguchi, *et al.*, "Transmission of electrical signals by spin-wave interconversion in a magnetic insulator," *Nature,* vol. 464, pp. 262-6, Mar 11 2010.

[36] A. V. Chumak, V. I. Vasyuchka, A. A. Serga, and B. Hillebrands, "Magnon spintronics," *Nature Physics,* vol. 11, pp. 453-461, 2015.

[37] C. Z. Chang, J. Zhang, X. Feng, J. Shen, Z. Zhang, M. Guo, *et al.*, "Experimental observation of the quantum anomalous Hall effect in a magnetic topological insulator," *Science,* vol. 340, pp. 167-70, Apr 12 2013.

[38] M. Z. Hasan and C. L. Kane, "Colloquium: Topological insulators," *Reviews of Modern Physics,* vol. 82, pp. 3045-3067, 2010.

[39] "Skyrmionics in sight," *Nat Nanotechnol,* vol. 8, p. 883, Dec 2013.

[40] L. Landau, "On the theory of phase transitions," *Zh. Eksp. Teor. Fiz.,* vol. 7, pp. 19-32, 1937.

[41] L. D. P. L. P. L. E. M. Landau, *Statistical physics Part 2, Part 2*. Oxford; New York [etc.]: Pergamon Press, 1981.

[42] T. L. Gilbert, "Classics in Magnetics A Phenomenological Theory of Damping in Ferromagnetic Materials," *IEEE Transactions on Magnetics,* vol. 40, pp. 3443-3449, 2004.

[43] G. Yu, P. Upadhyaya, Y. Fan, J. G. Alzate, W. Jiang, K. L. Wong, *et al.*, "Switching of perpendicular magnetization by spin-orbit torques in the absence of external magnetic fields," *Nat Nanotechnol,* vol. 9, pp. 548-54, Jul 2014.

[44] S. Hoffman, P. Upadhyaya, and Y. Tserkovnyak, "Spin-torque ac impedance in magnetic tunnel junctions," *Physical Review B,* vol. 86, 2012.

[45] Y. A. Bychkov and E. I. Rashba, "Oscillatory effects and the magnetic susceptibility of carriers in inversion layers," *Journal of Physics C: Solid State Physics,* vol. 17, pp. 6039-6045, 1984.

[46] V. M. Edelstein, "Spin polarization of conduction electrons induced by electric current in two-dimensional asymmetric electron systems," *Solid State Communications,* vol. 73, pp. 233-235, 1990.

[47] T. Maruyama, Y. Shiota, T. Nozaki, K. Ohta, N. Toda, M. Mizuguchi, *et al.*, "Large voltage-induced magnetic anisotropy change in a few atomic layers of iron," *Nat Nanotechnol,* vol. 4, pp. 158-61, Mar 2009.

[48] U. Bauer, L. Yao, A. J. Tan, P. Agrawal, S. Emori, H. L. Tuller, *et al.*, "Magneto-ionic control of interfacial magnetism," *Nat Mater,* vol. 14, pp. 174-81, Feb 2015.

[49] W. Eerenstein, N. D. Mathur, and J. F. Scott, "Multiferroic and magnetoelectric materials," *Nature,* vol. 442, pp. 759-65, Aug 17 2006.

[50] I. Dzyaloshinsky, "A thermodynamic theory of "weak" ferromagnetism of antiferromagnetics," *Journal of Physics and Chemistry of Solids,* vol. 4, pp. 241-255, 1958.

[51] T. Moriya, "New Mechanism of Anisotropic Superexchange Interaction," *Physical Review Letters,* vol. 4, pp. 228-230, 1960.

[52] K. Garello, I. M. Miron, C. O. Avci, F. Freimuth, Y. Mokrousov, S. Blugel, *et al.*, "Symmetry and magnitude of spin-orbit torques in ferromagnetic heterostructures," *Nat Nanotechnol,* vol. 8, pp. 587-93, Aug 2013.

[53] I. M. Miron, K. Garello, G. Gaudin, P. J. Zermatten, M. V. Costache, S. Auffret, *et al.*, "Perpendicular switching of a single ferromagnetic layer induced by in-plane current injection," *Nature,* vol. 476, pp. 189-93, Aug 11 2011.

[54] L. Liu, O. J. Lee, T. J. Gudmundsen, D. C. Ralph, and R. A. Buhrman, "Current-Induced Switching of Perpendicularly Magnetized Magnetic Layers Using Spin Torque from the Spin Hall Effect," *Physical Review Letters,* vol. 109, 2012.

[55] K. M. D. Hals and A. Brataas, "Phenomenology of current-induced spin-orbit torques," *Physical Review B,* vol. 88, Aug 20 2013.

[56] *It should be noted that the new DL term can also promote switching of perpendicular magnets by acting as a "negative" damping, in a fashion similar to STT-driven switching in perpendicular magnetic tunnel junctions[23], however based on the shifts seen in the experimental EHE loops presented in this work, the switching is attributed predominantly to the FL term.*

[57] A. J. Schellekens, A. van den Brink, J. H. Franken, H. J. M. Swagten, and B. Koopmans, "Electric-field control of domain wall motion in perpendicularly magnetized materials," *Nature communications,* vol. 3, p. 847, May 2012.

[58] S. Ikeda, K. Miura, H. Yamamoto, K. Mizunuma, H. D. Gan, M. Endo, *et al.*, "A perpendicular-anisotropy CoFeB-MgO magnetic tunnel junction," *Nature Materials,* vol. 9, pp. 721-724, Sep 2010.

[59] A. Manchon, C. Ducruet, L. Lombard, S. Auffret, B. Rodmacq, B. Dieny, *et al.*, "Analysis of oxygen induced anisotropy crossover in Pt/Co/MOx trilayers," *Journal of Applied Physics,* vol. 104, p. 043914, Aug 15 2008.

[60] K. Kita, D. W. Abraham, M. J. Gajek, and D. C. Worledge, "Electric-field-control of magnetic anisotropy of Co0.6Fe0.2B0.2/oxide stacks using reduced voltage," *Journal of Applied Physics,* vol. 112, p. 033919, Aug 1 2012.

[61] H. X. Yang, M. Chshiev, B. Dieny, J. H. Lee, A. Manchon, and K. H. Shin, "First-principles investigation of the very large perpendicular magnetic anisotropy at Fe|MgO and Co|MgO interfaces," *Physical Review B,* vol. 84, p. 054401, 2011.

[62] O. J. Lee, L. Q. Liu, C. F. Pai, Y. Li, H. W. Tseng, P. G. Gowtham, *et al.*, "Central role of domain wall depinning for perpendicular magnetization switching driven by spin torque from the spin Hall effect," *Physical Review B,* vol. 89, p. 024418, 2014.

[63] U. H. Pi, K. Won Kim, J. Y. Bae, S. C. Lee, Y. J. Cho, K. S. Kim, *et al.*, "Tilting of the spin orientation induced by Rashba effect in ferromagnetic metal layer," *Applied Physics Letters,* vol. 97, p. 162507, 2010.

[64] Y. A. Bychkov and E. I. Rashba, "Properties of a 2d Electron-Gas with Lifted Spectral Degeneracy," *Jetp Letters,* vol. 39, pp. 78-81, 1984.

[65] D. Bhowmik, L. You, and S. Salahuddin, "Possible Route to Low Current, High Speed, Dynamic Switching in a Perpendicular Anisotropy CoFeB-MgO Junction Using Spin Hall Effect Of Ta," *2012 Ieee International Electron Devices Meeting (Iedm),* 2012.

[66] J. E. Moore, "The birth of topological insulators," *Nature,* vol. 464, pp. 194-8, Mar 11 2010.

[67] X.-L. Qi and S.-C. Zhang, "Topological insulators and superconductors," *Reviews of Modern Physics,* vol. 83, pp. 1057-1110, 2011.

[68] H. Zhang, C.-X. Liu, X.-L. Qi, X. Dai, Z. Fang, and S.-C. Zhang, "Topological insulators in Bi2Se3, Bi2Te3 and Sb2Te3 with a single Dirac cone on the surface," *Nature Physics,* vol. 5, pp. 438-442, 2009.

[69] F. Mahfouzi, N. Nagaosa, and B. K. Nikolić, "Spin-Orbit Coupling Induced Spin-Transfer Torque and Current Polarization in Topological-Insulator/Ferromagnet Vertical Heterostructures," *Physical Review Letters,* vol. 109, 2012.

[70] Y. Tserkovnyak and D. Loss, "Thin-Film Magnetization Dynamics on the Surface of a Topological Insulator," *Physical Review Letters,* vol. 108, 2012.

[71] X. Kou, L. He, M. Lang, Y. Fan, K. Wong, Y. Jiang, *et al.*, "Manipulating surface-related ferromagnetism in modulation-doped topological insulators," *Nano Lett,* vol. 13, pp. 4587-93, Oct 9 2013.

[72] J. G. Checkelsky, J. Ye, Y. Onose, Y. Iwasa, and Y. Tokura, "Dirac-fermion-mediated ferromagnetism in a topological insulator," *Nature Physics,* vol. 8, pp. 729-733, 2012.

[73] Y. L. Chen, J. H. Chu, J. G. Analytis, Z. K. Liu, K. Igarashi, H. H. Kuo, *et al.*, "Massive Dirac fermion on the surface of a magnetically doped topological insulator," *Science,* vol. 329, pp. 659-62, Aug 6 2010.

[74] L. A. Wray, S.-Y. Xu, Y. Xia, D. Hsieh, A. V. Fedorov, Y. S. Hor, *et al.*, "A topological insulator surface under strong Coulomb, magnetic and disorder perturbations," *Nature Physics,* vol. 7, pp. 32-37, 2010.

[75] X. F. Kou, W. J. Jiang, M. R. Lang, F. X. Xiu, L. He, Y. Wang, *et al.*, "Magnetically doped semiconducting topological insulators," *Journal of Applied Physics,* vol. 112, p. 063912, 2012.

[76] D. Hsieh, Y. Xia, D. Qian, L. Wray, J. H. Dil, F. Meier, *et al.*, "A tunable topological insulator in the spin helical Dirac transport regime," *Nature,* vol. 460, pp. 1101-5, Aug 27 2009.

[77] I. Garate and M. Franz, "Inverse Spin-Galvanic Effect in the Interface between a Topological Insulator and a Ferromagnet," *Physical Review Letters,* vol. 104, 2010.

[78] W. Jiang, P. Upadhyaya, W. Zhang, G. Yu, M. B. Jungfleisch, F. Y. Fradin, *et al.*, "Magnetism. Blowing magnetic skyrmion bubbles," *Science,* vol. 349, pp. 283-6, Jul 17 2015.

[79] P. Upadhyaya, G. Yu, P. K. Amiri, and K. L. Wang, "Electric-field guiding of magnetic skyrmions," *arxiv:1505.03972,* 2015.

[80] P. Upadhyaya, R. Dusad, S. Hoffman, Y. Tserkovnyak, J. G. Alzate, P. K. Amiri, *et al.*, "Electric field induced domain-wall dynamics: Depinning and chirality switching," *Physical Review B,* vol. 88, 2013.

[81] J. Scott Russell, "Report on waves," *Fourteenth meeting of the British Association for the Advancement of Science*.

[82] A. H. Bobeck, P. I. Bonyhard, and J. E. Geusic, "Magnetic bubbles—An emerging new memory technology," *Proceedings of the IEEE,* vol. 63, pp. 1176-1195, 1975.

[83] S. Parkin and S. H. Yang, "Memory on the racetrack," *Nat Nanotechnol,* vol. 10, pp. 195-8, Mar 2015.

[84] D. A. Allwood, G. Xiong, C. C. Faulkner, D. Atkinson, D. Petit, and R. P. Cowburn, "Magnetic domain-wall logic," *Science,* vol. 309, pp. 1688-92, Sep 9 2005.

[85] K. S. Ryu, L. Thomas, S. H. Yang, and S. Parkin, "Chiral spin torque at magnetic domain walls," *Nature Nanotechnology,* vol. 8, pp. 527-533, 2013.

[86] S. Emori, U. Bauer, S. M. Ahn, E. Martinez, and G. S. Beach, "Current-driven dynamics of chiral ferromagnetic domain walls," *Nature Materials,* vol. 12, pp. 611-6, 2013.

[87] S. Emori, E. Martinez, K.-J. Lee, H.-W. Lee, U. Bauer, S.-M. Ahn, *et al.*, "Spin Hall torque magnetometry of Dzyaloshinskii domain walls," *Physical Review B,* vol. 90, p. 184427, 2014.

[88] A. P. Malozemoff and J. C. Slonczewski, *Magnetic Domain Walls in Bubble Materials*: Academic Press, New York, 1979.

[89] J. Eggers, "Nonlinear dynamics and breakup of free-surface flows," *Reviews of Modern Physics,* vol. 69, pp. 865-930, 1997.

[90] A. Thiaville, S. Rohart, E. Jue, V. Cros, and A. Fert, "Dynamics of Dzyaloshinskii domain walls in ultrathin magnetic films," *Epl,* vol. 100, p. 57002, 2012.

[91] J. Sampaio, V. Cros, S. Rohart, A. Thiaville, and A. Fert, "Nucleation, stability and current-induced motion of isolated magnetic skyrmions in nanostructures," *Nature Nanotechnology,* vol. 8, pp. 839-844, 2013.

[92] S. Rohart and A. Thiaville, "Skyrmion confinement in ultrathin film nanostructures in the presence of Dzyaloshinskii-Moriya interaction," *Physical Review B,* vol. 88, p. 184422, 2013.

[93] A. Fert, V. Cros, and J. Sampaio, "Skyrmions on the track," *Nature Nanotechnology,* vol. 8, pp. 152-156, 2013.

[94] R. Tomasello, E. Martinez, R. Zivieri, L. Torres, M. Carpentieri, and G. Finocchio, "A strategy for the design of skyrmion racetrack memories," *Scientific Reports,* vol. 4, p. 6784, 2014.

[95] Y. Zhou and M. Ezawa, "A reversible conversion between a skyrmion and a domain-wall pair in a junction geometry," *Nature Communications,* vol. 5, p. 4652, 2014.

[96] G. Q. Yu, P. Upadhyaya, Y. B. Fan, J. G. Alzate, W. J. Jiang, K. L. Wong, *et al.*, "Switching of perpendicular magnetization by spin-orbit torques in the absence of external magnetic fields," *Nature Nanotechnology,* vol. 9, pp. 548-554, 2014.

[97] G. Q. Yu, P. Upadhyaya, K. L. Wong, W. J. Jiang, J. G. Alzate, J. S. Tang, *et al.*, "Magnetization switching through spin-Hall-effect-induced chiral domain wall propagation," *Physical Review B,* vol. 89, p. 104421, 2014.

[98] "Methods and materials are available as supplementary materials on Science online.."

[99] A. Hubert and R. Schafer, *Magnetic Domains: The Analysis of Magnetic Microstructures* Springer, 2008.

[100] J. Iwasaki, M. Mochizuki, and N. Nagaosa, "Current-induced skyrmion dynamics in constricted geometries," *Nature Nanotechnology,* vol. 8, pp. 742-747, 2013.

[101] U. K. Rossler, A. N. Bogdanov, and C. Pfleiderer, "Spontaneous skyrmion ground states in magnetic metals," *Nature,* vol. 442, pp. 797-801, 2006.

[102] N. Nagaosa and Y. Tokura, "Topological properties and dynamics of magnetic skyrmions," *Nature Nanotechnology,* vol. 8, pp. 899-911, 2013.

[103] J. Choi, J. Wu, C. Won, Y. Z. Wu, A. Scholl, A. Doran, *et al.*, "Magnetic bubble domain phase at the spin reorientation transition of ultrathin Fe/Ni/Cu(001) film," *Physical Review Letters,* vol. 98, p. 207205, 2007.

[104] J. H. Franken, M. Herps, H. J. M. Swagten, and B. Koopmans, "Tunable chiral spin texture in magnetic domain-walls," *Scientific Reports,* vol. 4, p. 5248, 2014.

[105] L. Q. Liu, C. F. Pai, Y. Li, H. W. Tseng, D. C. Ralph, and R. A. Buhrman, "Spin-Torque Switching with the Giant Spin Hall Effect of Tantalum," *Science,* vol. 336, pp. 555-558, 2012.

[106] N. Romming, C. Hanneken, M. Menzel, J. E. Bickel, B. Wolter, K. von Bergmann, *et al.*, "Writing and Deleting Single Magnetic Skyrmions," *Science,* vol. 341, pp. 636-639, 2013.

[107] L. Sun, R. X. Cao, B. F. Miao, Z. Feng, B. You, D. Wu, *et al.*, "Creating an Artificial Two-Dimensional Skyrmion Crystal by Nanopatterning," *Physical Review Letters,* vol. 110, p. 167201, 2013.

[108] J. Li, A. Tan, K. W. Moon, A. Doran, M. A. Marcus, A. T. Young, *et al.*, "Tailoring the topology of an artificial magnetic skyrmion," *Nature Communications,* vol. 5, p. 4704, 2014.

[109] B. F. Miao, L. Sun, Y. W. Wu, X. D. Tao, X. Xiong, Y. Wen, *et al.*, "Experimental realization of two-dimensional artificial skyrmion crystals at room temperature," *Physical Review B,* vol. 90, p. 174411, 2014.

[110] A. Hrabec, N. A. Porter, A. Wells, M. J. Benitez, G. Burnell, S. McVitie, *et al.*, "Measuring and tailoring the Dzyaloshinskii-Moriya interaction in perpendicularly magnetized thin films," *Physical Review B,* vol. 90, p. 0204402(R), 2014.

[111] S. S. P. Parkin, M. Hayashi, and L. Thomas, "Magnetic domain-wall racetrack memory," *Science,* vol. 320, pp. 190-194, 2008.

[112] Y. S. Lin, "Bubble domains in magnetostatically coupled garnet films," *Applied Physics Letters,* vol. 23, p. 485, 1973.

[113] J.-H. Kim, K.-S. Ryu, J.-W. Jeong, and S.-C. Shin, "Large converse magnetoelectric coupling effect at room temperature in CoPd/PMN-PT (001) heterostructure," *Applied Physics Letters,* vol. 97, p. 252508, 2010.

[114] M. Hehn, K. Ounadjela, J. P. Bucher, F. Rousseaux, D. Decanini, B. Bartenlian, *et al.*, "Nanoscale Magnetic Domains in Mesoscopic Magnets," *Science,* vol. 272, pp. 1782-1785, 1996.

[115] C. Moutafis, S. Komineas, C. A. F. Vaz, J. A. C. Bland, T. Shima, T. Seki, *et al.*, "Magnetic bubbles in FePt nanodots with perpendicular anisotropy," *Physical Review B,* vol. 76, 2007.

[116] "llgmicro@mindspring.com."

[117] O. A. Tretiakov, D. Clarke, G.-W. Chern, Y. B. Bazaliy, and O. Tchernyshyov, "Dynamics of Domain Walls in Magnetic Nanostrips," *Physical Review Letters,* vol. 100, 2008.

[118] I. Makhfudz, B. Krüger, and O. Tchernyshyov, "Inertia and Chiral Edge Modes of a Skyrmion Magnetic Bubble," *Physical Review Letters,* vol. 109, 2012.

[119] G. E. Volovik, "Linear momentum in ferromagnets," *Journal of Physics C: Solid State Physics,* vol. 20, pp. L83-L87, 1987.

[120] A. A. Thiele, "Steady-State Motion of Magnetic Domains," *Physical Review Letters,* vol. 30, pp. 230-233, 1973.

[121] Y.-H. Liu, Y.-Q. Li, and J. H. Han, "Skyrmion dynamics in multiferroic insulators," *Physical Review B,* vol. 87, 2013.

[122] J. Sampaio, V. Cros, S. Rohart, A. Thiaville, and A. Fert, "Nucleation, stability and current-induced motion of isolated magnetic skyrmions in nanostructures," *Nat Nanotechnol,* vol. 8, pp. 839-44, Nov 2013.

[123] M. Lee, W. Kang, Y. Onose, Y. Tokura, and N. P. Ong, "Unusual Hall Effect Anomaly in MnSi under Pressure," *Physical Review Letters,* vol. 102, 2009.

[124] M. Julliere, "Tunneling between ferromagnetic films," *Physics Letters A,* vol. 54, pp. 225-226, 1975.

[125] M. N. Baibich, J. M. Broto, A. Fert, F. N. Van Dau, F. Petroff, P. Etienne, *et al.*, "Giant Magnetoresistance of (001)Fe/(001)Cr Magnetic Superlattices," *Physical Review Letters,* vol. 61, pp. 2472-2475, 1988.

[126] G. Binasch, P. Grünberg, F. Saurenbach, and W. Zinn, "Enhanced magnetoresistance in layered magnetic structures with antiferromagnetic interlayer exchange," *Physical Review B,* vol. 39, pp. 4828-4830, 1989.

[127] C.-G. Duan, J. P. Velev, R. F. Sabirianov, Z. Zhu, J. Chu, S. S. Jaswal, *et al.*, "Surface Magnetoelectric Effect in Ferromagnetic Metal Films," *Physical Review Letters,* vol. 101, 2008.

[128] S. Ikeda, K. Miura, H. Yamamoto, K. Mizunuma, H. D. Gan, M. Endo, *et al.*, "A perpendicular-anisotropy CoFeB-MgO magnetic tunnel junction," *Nat Mater,* vol. 9, pp. 721-4, Sep 2010.

[129] N. L. Schryer, "The motion of 180 °domain walls in uniform dc magnetic fields," *Journal of Applied Physics,* vol. 45, p. 5406, 1974.

[130] M. Endo, S. Kanai, S. Ikeda, F. Matsukura, and H. Ohno, "Electric-field effects on thickness dependent magnetic anisotropy of sputtered MgO/Co[sub 40]Fe[sub 40]B[sub 20]/Ta structures," *Applied Physics Letters,* vol. 96, p. 212503, 2010.

[131] M. K. Niranjan, C.-G. Duan, S. S. Jaswal, and E. Y. Tsymbal, "Electric field effect on magnetization at the Fe/MgO(001) interface," *Applied Physics Letters,* vol. 96, p. 222504, 2010.

[132] H. W. Schumacher, C. Chappert, R. C. Sousa, P. P. Freitas, and J. Miltat, "Quasiballistic Magnetization Reversal," *Physical Review Letters,* vol. 90, 2003.

[133] L. Thomas, M. Hayashi, X. Jiang, R. Moriya, C. Rettner, and S. S. Parkin, "Oscillatory dependence of current-driven magnetic domain wall motion on current pulse length," *Nature,* vol. 443, pp. 197-200, Sep 14 2006.

[134] A. Vanhaverbeke, A. Bischof, and R. Allenspach, "Control of Domain Wall Polarity by Current Pulses," *Physical Review Letters,* vol. 101, 2008.

[135] E. R. Moog and S. D. Bader, "Smoke signals from ferromagnetic monolayers: p(1×1) Fe/Au(100)," *Superlattices and Microstructures,* vol. 1, pp. 543-552, 1985.

[136] A. Kirilyuk, A. V. Kimel, and T. Rasing, "Ultrafast optical manipulation of magnetic order," *Reviews of Modern Physics,* vol. 82, pp. 2731-2784, 2010.

[137] M. Straub, R. Vollmer, and J. Kirschner, "Surface Magnetism of Ultrathinγ-Fe Films Investigated by Nonlinear Magneto-optical Kerr Effect," *Physical Review Letters,* vol. 77, pp. 743-746, 1996.

[138] W. Jiang, P. Upadhyaya, Y. Fan, J. Zhao, M. Wang, L.-T. Chang, *et al.*, "Direct Imaging of Thermally Driven Domain Wall Motion in Magnetic Insulators," *Physical Review Letters,* vol. 110, 2013.

[139] A. Yamaguchi, T. Ono, S. Nasu, K. Miyake, K. Mibu, and T. Shinjo, "Real-Space Observation of Current-Driven Domain Wall Motion in Submicron Magnetic Wires," *Physical Review Letters,* vol. 92, p. 077205, 2004.

[140] C. H. Marrows, "Spin-polarised currents and magnetic domain walls," *Advances in Physics,* vol. 54, pp. 585-713, Dec 2005.

[141] K. Uchida, J. Xiao, H. Adachi, J. Ohe, S. Takahashi, J. Ieda, *et al.*, "Spin Seebeck insulator," *Nature Materials,* vol. 9, pp. 894-897, Nov 2010.

[142] A. A. Kovalev and Y. Tserkovnyak, "Thermomagnonic spin transfer and Peltier effects in insulating magnets," *Europhys. Lett. ,* vol. 97, p. 67002, Mar 2012.

[143] P. Yan, X. S. Wang, and X. R. Wang, "All-Magnonic Spin-Transfer Torque and Domain Wall Propagation," *Physical Review Letters,* vol. 107, p. 177207, 2011.

[144] D. Hinzke and U. Nowak, "Domain Wall Motion by the Magnonic Spin Seebeck Effect," *Physical Review Letters,* vol. 107, p. 027205, 2011.

[145] P. Yan and G. E. W. Bauer, "Magnonic Domain Wall Heat Conductance in Ferromagnetic Wires," *Physical Review Letters,* vol. 109, p. 087202, 2012.

[146] X. S. Wang, P. Yan, Y. H. Shen, G. E. W. Bauer, and X. R. Wang, "Domain Wall Propagation through Spin Wave Emission," *Physical Review Letters,* vol. 109, p. 167209, 2012.

[147] E. Padrón-Hernández, A. Azevedo, and S. M. Rezende, "Amplification of Spin Waves by Thermal Spin-Transfer Torque," *Physical Review Letters,* vol. 107, p. 197203, Nov 4 2011.

[148] J. Xiao, G. E. W. Bauer, K.-c. Uchida, E. Saitoh, and S. Maekawa, "Theory of magnon-driven spin Seebeck effect," *Physical Review B,* vol. 81, p. 214418, 2010.

[149] Y. Tserkovnyak, A. Brataas, and G. E. W. Bauer, "Theory of current-driven magnetization dynamics in inhomogeneous ferromagnets," *Journal of Magnetism and Magnetic Materials,* vol. 320, pp. 1282-1292, 2008.

[150] A. A. Kovalev and Y. Tserkovnyak, "Thermoelectric spin transfer in textured magnets," *Physical Review B,* vol. 80, p. 100408, 2009.

[151] J. Torrejon, G. Malinowski, M. Pelloux, R. Weil, A. Thiaville, J. Curiale, *et al.*, "Unidirectional Thermal Effects in Current-Induced Domain Wall Motion," *Physical Review Letters,* vol. 109, p. 106601, 2012.

[152] Z. H. Zhang, Y. S. Gui, L. Fu, X. L. Fan, J. W. Cao, D. S. Xue, *et al.*, "Seebeck Rectification Enabled by Intrinsic Thermoelectrical Coupling in Magnetic Tunneling Junctions," *Physical Review Letters,* vol. 109, p. 037206, 2012.

[153] H. Fangohr, D. S. Chernyshenko, M. Franchin, T. Fischbacher, and G. Meier, "Joule heating in nanowires," *Physical Review B,* vol. 84, p. 054437, Aug 11 2011.

[154] C. M. Jaworski, J. Yang, S. Mack, D. D. Awschalom, R. C. Myers, and J. P. Heremans, "Spin-Seebeck Effect: A Phonon Driven Spin Distribution," *Physical Review Letters,* vol. 106, p. 186601, May 2 2011.

[155] D. Rugar, J. C. Suits, and C. J. Lin, "Thermomagnetic Direct Overwrite in Tbfe Using Thermally Induced Domain-Wall Energy Gradient," *Applied Physics Letters,* vol. 52, pp. 1537-1539, May 2 1988.

[156] S. U. Jen and L. Berger, "Thermal Domain Drag Effect in Amorphous Ferromagnetic Materials .2. Experiments," *Journal of Applied Physics,* vol. 59, pp. 1285-1290, Feb 15 1986.

[157] S. U. Jen and L. Berger, "Thermal Domain Drag Effect in Amorphous Ferromagnetic Materials .1. Theory," *Journal of Applied Physics*, vol. 59, pp. 1278-1284, Feb 15 1986.

[158] A. A. Thiele, "THEORY OF CYLINDRICAL MAGNETIC DOMAINS," *Bell System Technical Journal*, vol. 48, pp. 3287-+, 1969.

[159] A. Hamadeh, O. d'Allivy Kelly, C. Hahn, H. Meley, R. Bernard, A. H. Molpeceres, *et al.*, "Full Control of the Spin-Wave Damping in a Magnetic Insulator Using Spin-Orbit Torque," *Physical Review Letters*, vol. 113, 2014.

[160] A. Yamaguchi, A. Hirohata, T. Ono, and H. Miyajima, "Temperature estimation in a ferromagnetic Fe-Ni nanowire involving a current-driven domain wall motion," *Journal of Physics-Condensed Matter*, vol. 24, p. 024201, Jan 18 2012.